2004

MESOSPHERIC TEMPERATURE CLIMATOLOGY ABOVE UTAH STATE UNIVERSITY

Joshua P. Herron

MESOSPHERIC TEMPERATURE CLIMATOLOGY ABOVE

UTAH STATE UNIVERSITY

by

Joshua P. Herron

A thesis submitted in partial fulfillment
of the requirements for the degree

of

MASTER OF SCIENCE

in

Physics

Approved:

_____	_____
Dr. Vincent B. Wickwar Major Professor	Dr. D. Mark Riffe Committee Member
_____	_____
Dr. Robert W. Schunk Committee Member	Dr. Thomas Kent Dean of Graduate Studies

UTAH STATE UNIVERSITY
Logan, Utah

2004

ABSTRACT

Mesospheric Temperature Climatology Above

Utah State University

by

Joshua P. Herron, Master of Science

Utah State University, 2004

Major Professor: Dr. Vincent B. Wickwar
Department: Physics

A Rayleigh-scatter lidar has been in operation at Utah State University (41.7º N, 111.8 ° W) starting in September 1993 until the present (October 2003). The return profiles from the atmosphere have been analyzed to provide temperature measurements of the middle atmosphere from 45 to 90 km. Various methods of averaging were used to construct a temperature climatology of the region based on these observations. The data analysis algorithm has been critically analyzed to find possible sources of error, and has been compared to an independently derived technique. The resulting temperatures have been compared to other mid-latitude lidars with good agreement. Comparisons were made with temperatures from other ground-based instruments at Bear Lake Observatory. Additional comparisons were carried out with two satellite-based instruments, WINDII and SABER. The comparison of individual nights with the SABER instrument produced surprisingly good agreement considering the difference in the two methds. With the basic analysis of the temperature climatology completed in this work, an outline is given

for future research and upgrades to the facility.

(155 pages)

ACKNOWLEDGMENTS

I first must thank Dr. Vincent B. Wickwar for his help and guidance in understanding the necessary physics and operations of a lidar system. Thanks must also be given to John Meriwether and Tom Wilkerson for the seemingly perpetual loan of much of the equipment used for the lidar. I would like to thank Marc Hammond for showing me how to operate and maintain much of the equipment.

I would also like to thank all of those who have worked with the USU lidar over the years of its operation. They have spent many sleepless nights in a dark lab making observations with the lidar. Their names are Brian Anderson, Angela Bodrero, Kayla Brown, Nathan Bunderson, Courtney Butler, Stephen Collins, Joel Drake, Scot R. Elkington, Will Fredin, Spencer Fuller, Nicole Grotepas, John James, Paul Johnson, Teresa Jones, Doug Kenny, Jeffrey Leek, Eric Lundell, John Maloney, Bethany Martineau, Ian Monson, Gerald (Dusti) McEwen, Stephen Melzer, Patrick Neary, Karen Nelson, Spencer Nelson, Keith Oliver, Michael Purcell, Robert Ream, Ryan Smith, Joseph Andy Spencer, Kristina Thomas, Marie Westbrook, Rachel Whatcott, and Troy Wynn.

I would also like to thank Stephen Argall and Robert Sica for their temperature climatology and for providing raw data from their instrument for analysis. I would also like to thank Patrick Espy for the temperature results from the BOMEM, Michael Taylor, and his post doc Alok Taori for the results from the OH temperature mapper. I would like to express thanks to James Russell and Marianna Shepard for providing the SABER and WINDII results. Many thanks to Ray Roble and Ben Foster for the model

runs from the TIME–GCM.

I would also like to express my thanks to my family for the support and encouragement they have provided over the years. I would especially like to express my thanks to my wife, Ann. She has always been by my side, and has been a motivating force in my life. I would like to give thanks to the USU Physics Department and the Rocky Mountain NASA Space Grant Consortium for their financial support.

The lidar received partial support through National Science Foundation grants ATM-01234145, ATM-9714789, ATM-9525829, ATM-9302118, and ATM-9203034. Two NSF grants ATM-9813903 and ATM-9413909 and an AFOSR DURIP grant F49620-01-1-0275 upgraded ALO and the equipment within it.

Joshua P. Herron

CONTENTS

LIST OF TABLES

LIST OF FIGURES

Figure Page

CHAPTER 1

INTRODUCTION

1. Statement of Problem

The atmosphere above the Earth has a varied thermal, chemical, and dynamical structure. Various regions or layers can be defined in the atmosphere by means of their chemical, dynamical, or thermal structure. Naming the regions of the atmosphere by the neutral temperature structure gives the troposphere, stratosphere, mesosphere, and the thermosphere.

The natural behavior of the atmosphere is that of a coupled system. All of the layers of the atmosphere have a strong interdependence upon each other chemically, dynamically and energetically. The temperature structure of the atmosphere is dependent upon all three of these parameters. By creating a good general understanding of the temperature structure of the atmosphere we can gain insight into the physics of the region.

Measurements of the middle atmosphere have a gap between 30 and 60 km that can be covered by Rayleigh-scatter lidars. The Atmospheric Lidar Observatory (ALO) Rayleigh-scatter lidar located on the Utah State University (USU) campus is unique as it is one of only a very few that have been operating for an extended period of time. Problems covered in this thesis are (1) obtaining reliable temperatures from the ALO data set, (2) deriving a temperature climatology based on 1993 –2003 data, and (3) to show these temperature have the potential for providing new and useful understanding of the physics of the mesosphere and its relationship to the regions above and below it.

2. Background

The troposphere at mid-latitudes is characterized by the presence of a nearly constant rate of decrease in temperature from the ground to about 10 km. This constant rate of temperature decrease is known as the lapse rate, which has a mean value of 6.5 K/km for the troposphere. The stratosphere is characterized by an increase in temperature with altitude, or a negative lapse rate. The negative lapse rate of the stratosphere is due to ozone heating in the region. The stratosphere temperatures reach a maximum near 50 km at the stratopause where the rate of cooling is matched by the rate of heating from CO_2. The mesosphere is characterized by a positive lapse rate or a decrease in temperature with altitude. This change in the temperature gradient is due primarily to the greater rate of cooling from CO_2. In this region both radiative and turbulent processes are important. The decreasing temperatures reach a minimum at ~ 90 km in the summer and reach ~ 105 km in the winter at the mesopause. Above the mesopause is the thermosphere where the temperature can reach 500K to 2000K depending on solar activity. The transitional regions are known as the tropopause, stratopause, and mesopause. They separate the different layers and usually denote some change in the characteristics of the atmosphere (Figure 1).

The definitions of lower, middle, and upper atmospheres are another way to label regions of the atmosphere. The term lower atmosphere refers primarily to the troposphere. As we have had the most contact with the troposphere, it is easy to see why it is the region for which we have the most knowledge. Atmospheric data is collected twice daily by balloon-based radiosondes around the world to a maximum of ~ 30 km.

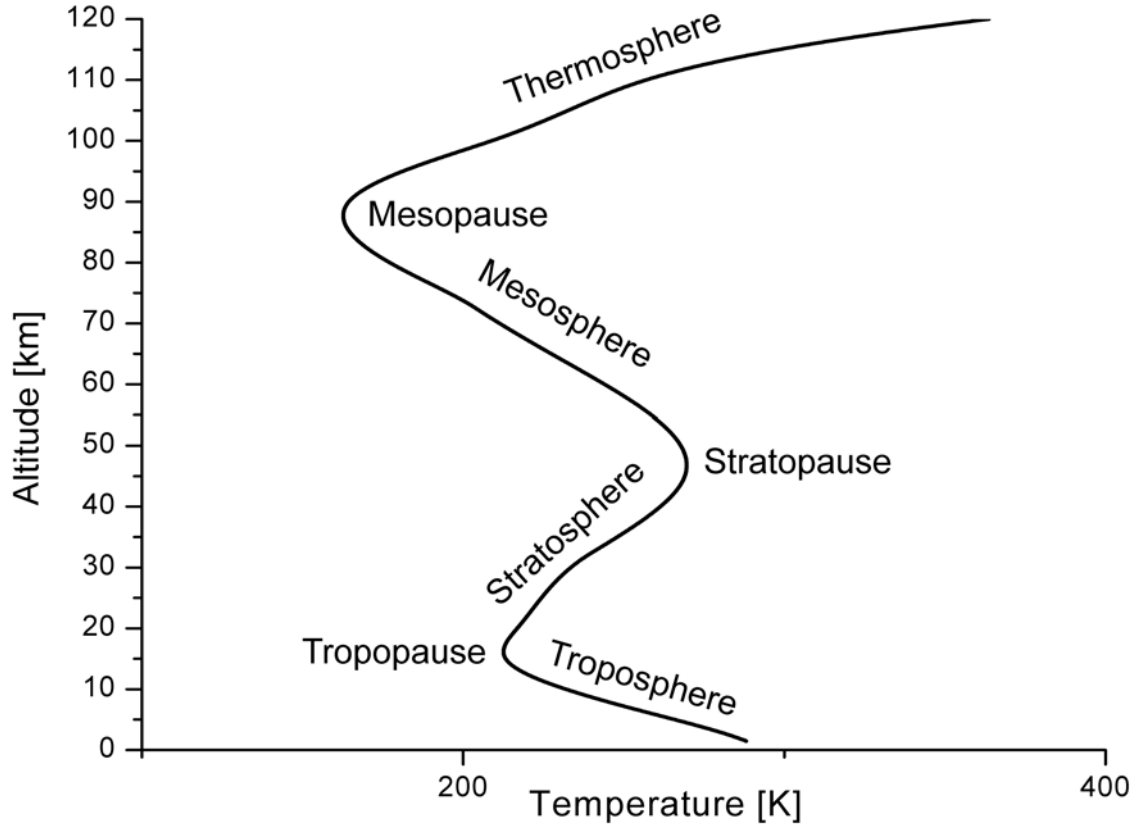

Figure 1. The temperature structure of the neutral atmosphere [based upon MSISe90] covering the troposphere and part of the stratosphere.

The upper atmosphere, which extends from about 100 km, primarily refers to the thermosphere and is second in our understanding, and in experimental knowledge. Phenomena such as the aurora and airglow and the effects of the ionosphere on radio communication are key in pushing forward the understanding of the upper atmosphere. Study of the upper atmosphere has increased since the advent of satellites.

The middle atmosphere, which extends from 10 to 110 km, covers the stratosphere and the mesosphere, and the transitions to the troposphere below and the thermosphere above. It has been the recent intense study of global change that has produced the greatest interest in studying the middle atmosphere. Ozone is one of the primary

molecules in the atmosphere that absorbs solar UV radiation. The development of observing techniques and concern over the loss of O^3 spurred the study of this region.

Measuring the middle atmosphere has proven to be difficult. Much of the middle atmosphere lies beyond the range of aircraft, and balloons, and below the range of in situ satellites. This explains the difficulty in making continuous in situ measurements of the middle atmosphere. Due to the difficulty in making measurements and the lack of a good understanding of the dynamics of the atmosphere in this region, the middle atmosphere has been termed the ignorosphere by many. The necessity for a complete understanding of the structure of the atmosphere has pushed for measurements to be made of the middle atmosphere.

The advent of rocket technology over the past 50 years has given atmospheric scientists the ability to make the first in situ measurements of this region. Rockets can carry a variety of instruments and materials into this region of the atmosphere and as a result provide many methods for determining the physical characteristics of this region. Spheres released from rockets for example have been tracked by radar providing information of the atmospheric density through the drag on the spheres. Many instruments carried by rockets make direct measurements of the region also. These rocket methods can only produce a limited amount of information as they are limited in the amount of time they spend in the region and the cost of launching them. However, rockets provide a useful means to calibrate many of the remote sensing techniques used to make measurements of this region.

Radar has proven effective in providing measurements of the middle atmosphere.

Stratosphere-troposphere or ST radar provides coverage from 1 to 30 km, and MF radar provides coverage from 60 to 100 km for daytime and 80 to 110 km for nighttime. This leaves a hole in the coverage of the middle atmosphere from 30 to 60 km.

Satellites also provide measurements of the middle atmosphere. Satellites do so through various measurements of emission and absorption spectra from various sources and wavelengths equivalent to those done from the ground with spectrometers, interferometers, all-sky cameras, and microwave instruments. Such measurements provide the mean temperature and density. Limb measurements provide a slight improvement in the vertical resolution of the measurements, however there is a considerable loss in the horizontal resolution as the measurement is made from the side. In older satellites the vertical resolution was ~ 12 km with newer systems making measurements every 2 km. Satellites play a key role in measuring the overall dynamics of the atmosphere as they give both longitudinal and latitudinal coverage. Satellites such as UARS (Upper Atmospheric Research Satellite) and TIMED (Thermosphere Ionosphere Mesosphere Energetics and Dynamics) have been dedicated to measurements of the middle atmosphere.

Rayleigh-scatter lidar systems are designed to detect the Rayleigh backscatter from molecules in the atmosphere. Vertical sounding of relative density are available from an altitude range of 25 to 110 km. As most lidar facilities are permanent locations, they provide high time resolution but provide limited geographic coverage. Temperatures from the lidar are typically provided in hourly or nightly profiles. The results from the lidar are derived from the physics of the atmosphere, are not dependent upon an instrument calibration, and provide a good standard for comparisons. Comparisons

between the Rayleigh-scatter lidar technique and other have provided good agreement. Such high temporal and vertical resolution is important for the study of the dynamics of the middle atmosphere, as they enable the study of gravity waves, tidal variations, stratospheric warmings, planetary waves, mesospheric inversion layers, solar rotation 28-day variations, seasonal variation, noctilucent clouds, sunspot cycle, and climatology.

3. Overview

The objectives of this thesis are:

1) Determine good mesospheric temperatures from the ALO Rayleigh-scatter lidar. This includes the selection criteria for good data, a detailed discussion of the statistical uncertainties in the measurements, and possible systematic errors.
    a. Compare the temperature-reduction algorithms to those used by the Purple Crow Lidar (PCL) in western Ontario. Discuss the differences in the derived temperature and the steps needed to bring them into agreement.
    b. Simulate the lidar data, starting from a model atmosphere, and retrieve the model temperatures.
2) Derive a temperature climatology from the measurements taken by the ALO Rayleigh-scatter lidar between 1993 & 2003.
3) Compare ALO temperatures to other mid-latitude temperatures to investigate future research projects.
    a. Compare average temperatures from ALO to those from PCL.
    b. Compare average temperatures from the Rayleigh-scatter lidar to the

temperature results from the WINDII instrument on the UARS satellite.

c. Compare individual nightly temperatures from the Rayleigh-scatter lidar to the temperatures from the SABER instrument on the TIMED satellite.
d. Compare the results from the Rayleigh-scatter lidar to several instruments located at the Bear Lake Observatory (BLO) that measure temperature at ~87 km —A Fabry-Perot Interferometer, Michelson Interferometer, and an Imager.
e. Compare the results from the Rayleigh-scatter lidar at ALO with the French Rayleigh-scatter lidars at Haute Provence (OHP) and Biscarosse (BIS).
f. Compare the results of the temperature climatology with the TIME-GCM atmospheric model.

The thesis is organized with a detailed description in Chapter 2 of the Rayleigh-scatter lidar located at the Atmospheric Lidar Observatory (ALO) located on the Utah State University campus (USU). Chapter 3 details the reduction theory by which temperature measurements are derived from lidar sounding for the atmosphere. This includes a detailed analysis of the measurement uncertainty. Chapter 4 details the implementation of the data reduction, the systematic error that could be present in the results, and the steps taken to minimize it. Chapter 5 details the data selection. The resulting temperature profiles from the lidar are discussed in Chapter 6 and include various methods of averaging the data to emphasize certain physical aspects. Chapter 7 contains the details of the temperature comparisons. The thesis summary and the details

of future work are detailed in Chapter 8.

CHAPTER 2

RAYLEIGH-SCATTER LIDAR SYSTEM

The Atmospheric Lidar Observatory (ALO) is located on the Utah State University (USU) campus and has operated a Rayleigh-scatter lidar since 1993. This Rayleigh-scatter lidar system can produce relative density measurements that extend from the stratopause to the mesopause (~42km — 100 km). These relative measurements of density can be used to derive an absolute measurement of temperature (~ 42 km — 90 km). This is the power of a Rayleigh-scatter lidar.

A Rayleigh-scatter lidar consists of few components compared to other lidars. The current configuration of the USU lidar contains a transmitter, receiver, and the data acquisition system, which can be seen in Figure 2 and will be discussed below. Currently the system is in the midst of an upgrade, not only the data acquisition system, but also the receiver and transmitter systems. The upgrades to the receiver system will increase the collecting area of the overall system by 33 times. This increased capability will be used to reduce the integration times needed for temperature measurements and to increase the maximum altitude. Temperature measurements that currently take eight hours, for example, will only require 15 minutes with the new system.

1. Lidar Transmitter

While the transmitter of the lidar system consists of very few components, the principle component is the laser, which is complex. The term laser is actually an acronym for Light Amplification by the Stimulated Emission of Radiation. The

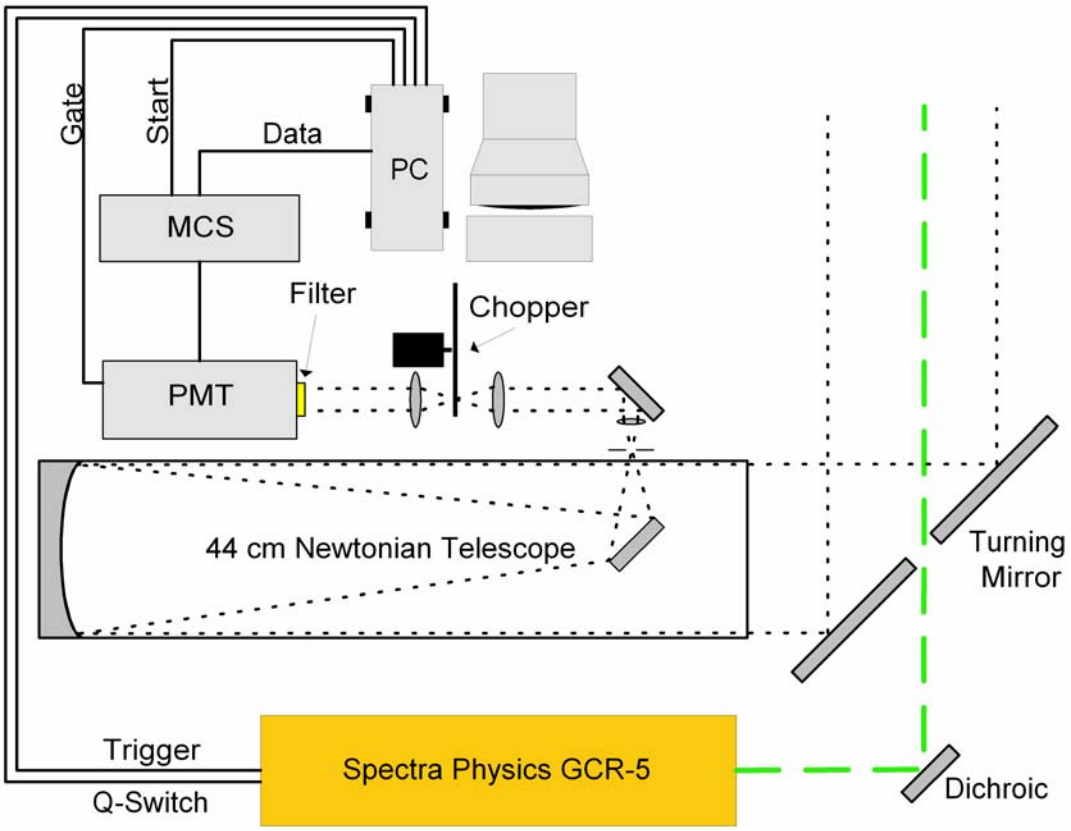

Figure 2. Simplified lidar diagram.

laser used in the transmitter system is a Spectra Physics GCR-5 laser. The GCR-5 uses neodymium:yttrium aluminum garnet (Nd:YAG) crystals with the cubic crystal characteristics of garnets for the lasing medium. This laser is commonly referred to as a YAG for the crystal that is the host for the trivalent neodymium ions, which are the lasing atoms. The GCR-5 has two oscillating rods and one amplification rod. Originally a GCR-6 was used that had two amplification rods, which provided slightly more power: and the early data show a slightly greater amount of backscattered light. The GCR-5 is a pulsed laser that is Q-switched, which enables the laser to create short pulses of intense light at a continuous repetition rate of 30 Hz. The Q-switched pulse from the laser is ~ 7 ns long. It is possible to run the laser in a long-pulse mode that is convenient for

alignment as the energy density is reduced.

The cross section for Rayleigh scattering varies as λ^{-4}, so naturally the shorter the wavelength used for the transmitter system, the greater the return. The principal wavelength for the Nd:YAG is 1064 nm, a doubling crystal is placed in the path of the beam, producing a 50 percent conversion of the laser energy to the first harmonic at 532 nm. The laser output could be tripled, to 355 nm, but such factors as atmospheric transmittance, optical transmission, energy per laser pulse, and conversion efficiency favor the second harmonic at 532 nm. The laser output as it passes from the doubling crystal is directed along the optical axis of the receiving telescope to produce a co-axial configuration for the transmitter and receiver. The energy density of the laser pulse prevents the use of aluminized mirrors so dielectric mirrors are used. Each of the dielectric mirrors is coated for dichroic properties: high reflectance at 532 nm and high transmittance at 1064 nm. The remaining 1064-nm radiation is sent into a beam dump.

2. Lidar Receiver

The receiver system is composed of the light collector, optics, chopper, filters and the detector. The basic configuration of the system is a co-axial one in which the transmitted signal is sent out along the optical path of the receiver system. Due to the small area of the detector, a telescope is used to increase the collecting area of the detector system. The other optics in the system are used to direct the output of the telescope into the detector system.

The USU lidar employs a Newtonian telescope to collect the backscattered light. The telescope has a 44-cm diameter and a 201-cm focal length. The telescope is

mounted horizontally and a large flat mirror is placed at a 45° angle to vertical to direct the return signal into the telescope. The transmitted signal, to be co-axial with the receiver, passes through a cutout in the center of the turning mirror. This modification has simplified the task of creating a co-axial lidar as a small mirror placed under the turning mirror is used to direct the laser beam along the same optical axis as the telescope. This small mirror is a dichroic mirror mounted in an open-loop motorized mount to facilitate the alignment of the laser and the telescope.

The backscattered light collected by the telescope passes through a field stop and a lens, which ensures the field of view of the telescope is triple that illuminated by the laser. This field of view of the telescope allows for alignment of the system and pointing fluctuations of the laser while minimizing the amount of background light that enters the system. After the field lens, a small lens is used to collimate the return signal. This collimated beam is then focused onto the vertical plane of a mechanical chopper, which blocks the return signal from the lower altitudes. After passing through the plane of the chopper the light is collimated to slightly smaller than the size of the cathode of the photomultiplier tube (PMT). Before the light enters the PMT, it passes through a narrow band-pass interference filter (1 nm FWHM). The filter is used to reduce the amount of white light that enters the receiver system from the background sky.

The photon detector for this system is a green sensitive bialkali photomultiplier tube (Electron Tubes 9954 B), which converts the incoming photons into electronic pulses. The conversion of photons to electrons is done by the photocathode through the photoelectric effect. These photoelectrons are then amplified through a dynode string

that amplifies the signal through the generation of secondary electrons. The gain of the photomultiplier tube is approximately 10^6 and creates a detectable voltage for each photoelectron. The quantum efficiency of the photomultiplier tube is ~ 13 percent at 532 nm. While other devices such as CCDs may have higher quantum efficiency, they lack the high temporal resolution needed for the ranging of the lidar returns.

The signals generated from the PMT include a certain amount of spurious noise that is referred to as the dark count of the tube. The dark count is found by measuring the output when there is no illumination on the tube. A certain amount of noise is generated inside of the photomultiplier tube from thermionic emission from both the dynode string and the photocathode. The dark count generated by the photocathode is indistinguishable from those counts produced by photons. This part of the dark count can be reduced by cooling the PMT. For this we use a thermoelectrically cooled PMT housing (Products for Research) that cools the PMT to 30 K below ambient. Originally, the housing was air-cooled, enabling the PMT to be operated at ~-10 C. The current housing is coupled to a recirculating chiller that drops the ambient temperature to 5 C and the PMT temperature to ~-25 C.

The density of the atmosphere is reduced by a factor of about 10^6 between 0 and 100 km [*Banks and Kockarts*, 1973]. The high backscatter number density at the lower altitudes along with aerosols and clouds create a large low-altitude signal such that a mechanical chopper must be employed along with electronic gating to prevent saturation of the PMT. Gating of the PMT is accomplished by setting the voltage on the photocathode to the voltage of the first dynode. This gating reduces the gain of the PMT

by a factor of 10^2 to 10^3 thereby provides some protection for the PMT.

The mechanical chopper is also the source of the timing for the lidar system. The chopper is equipped with a bow-tie blade and is set to rotate at a multiple of the laser repetition rate. Typically this is six or seven times the 30 Hz repetition rate of the laser. Currently the mechanical chopper is set to rotate at 210 Hz or 6300 rpm. A timing unit controlled by Labview performs a divide by six or seven and introduces a time delay to generate the 30 Hz signal to trigger the laser to fire when the chopper is blocking the receiver. The delay is adjusted for the chopper to open around 20 km. By this method the majority, but not all, of the low-altitude backscatter return is blocked from entering the PMT. As the laser fires, a trigger pulse is used to start the data acquisition and to gate the PMT on at 38.5 km. Figure 3 shows typical returns from the lidar depicting the opening of the chopper and the electronic gating of the PMT.

The logarithmic color scale in Figure 3 enables some of the smaller features we see with the lidar to stand out against the large Rayleigh-scatter return. For this particular night the lidar was started at dusk and you can see the decrease of the background light between 70 km and 150 km. Between profiles 50 and 90 you can see a thin cirrus cloud layer has formed during the night and there is a slight decrease in the signal as a result. The profile plotted on the right of the image plot shows the night-long average of the raw photocounts, along with the appropriate labels. Centered around 20 km a small haze layer is clearly seen.

3. Data Acquisition System

The data acquisition system for the lidar consists of a multichannel scalar or MCS.

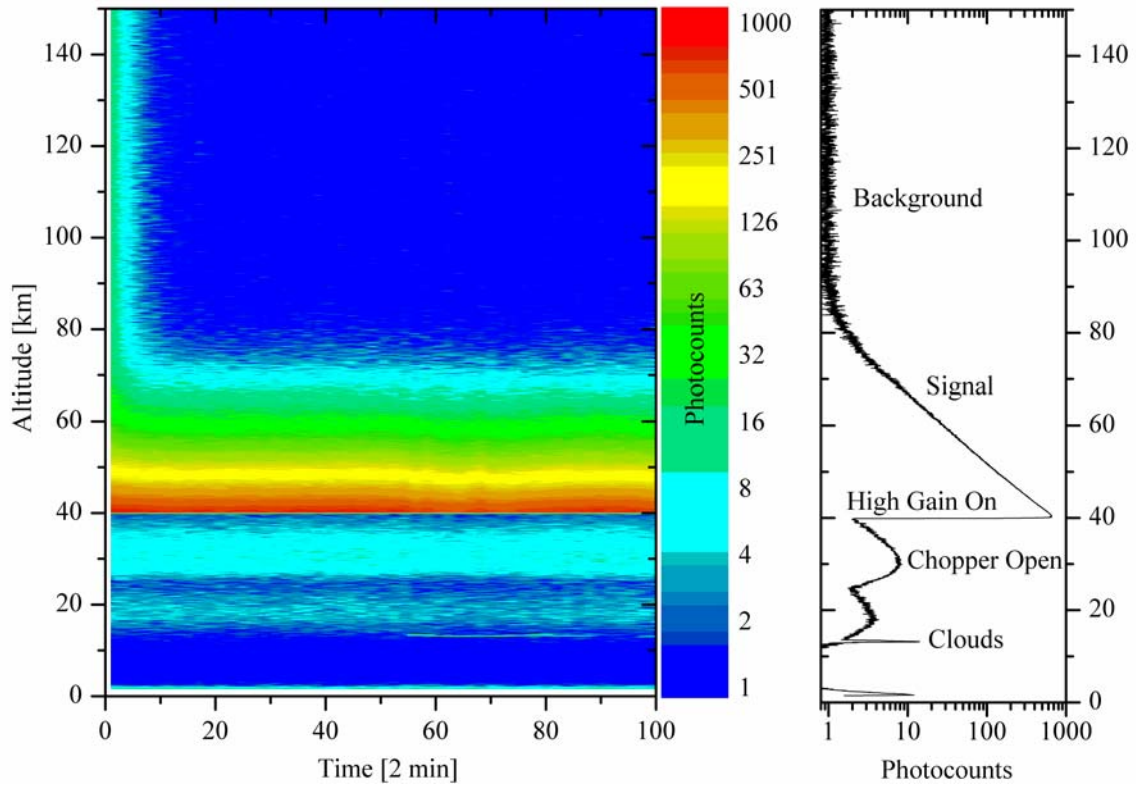

Figure 3. Rayleigh-scatter lidar return from the ALO lidar. The nightly average of the data has also been calculated to give a better understanding of when certain events take place, such as the opening of the chopper and the gating of the PMT.

Since the lidar is basically doing time of flight measurements between the outgoing laser pulses and their returns, a high-speed counter is necessary. Signals generated by the PMT first pass through a small fast 200x pre-amp, before they are passed on to the MCS by a standard BNC cable. This amplification is necessary due to the small amplitude of the signals. The amplifier is located as close to the detector as possible to minimize the amplification of line noise. The MCS has 16000 separate range bins, of which 14400 are used. The bin width is set at 250 ns, which gives an altitude resolution for the system of 37.5 m. The return signals from 3600 laser pulses are summed before the data is

recorded on a standard PC. With the repetition rate of the laser set to 30 Hz this corresponds to data samples spaced every two minutes. There is a four-second delay between the end of one record and the start of the next as the system records its data to disk.

With the MCS unit, a compromise was made between the resolution and the maximum range of the lidar. The shortest possibility would be to have the bin width set to 5 ns or 0.75 meter is range, but with 16,000 bins this would give a maximum range of 12 km. Fortunately the physics of the atmosphere provides a measure of the appropriate resolution we should use for a Rayleigh lidar system. The scale height (H) is dependent upon the temperature and the mean molecular mass (m) of a neutral gas, and provides a measure of the distance over which we expect to see significant changes in the atmosphere

$$H = \frac{kT}{\langle m \rangle g}. \qquad 2.3.1$$

Since the variation of the mean molecular mass m is small in the mesosphere and the small decrease in g partly compensates for the decrease in T, the scale height is almost a constant 7 km. Thus the spatial resolution of 37.5 m (250 ns gate width) for the lidar is very high. It was made this small for gravity wave studies and for thin cloud or aerosol layers. To obtain a good signal for the temperatures, the data are integrated over 3 km (80 bins).

The calculation of temperature makes the assumption of hydrostatic equilibrium. An integration time of 15 minutes averages out the shortest period waves and allows the re-establishment of hydrostatic equilibrium from longer period disturbances. As a result

when we average together data from the lidar to derive temperatures we should include 15 minutes of data at a minimum, but we typically use an hour of data as the minimum for temperature-reductions. When the returns are analyzed for spectral components the limiting factor is then the Brunt-Väisälä frequency. Again for the region of interest the corresponding period is only four minutes. By recording data at two-minute intervals we are able to measure frequencies down to the Brunt-Väisälä frequency.

4. Conclusion

As most components used in a Rayleigh-scatter lidar system are comparable in their efficiency, a measure of merit is usually used to compare two lidar systems to each other. The power-aperture product is the product of the average transmitter power and the area of the receiver. Two other Rayleigh-scatter lidar are compared to the ALO lidar. They are the Purple Crow Lidar (PCL) and the two French lidars at the Observatory of Haute-Provence (OHP) and at Biscarrosse (BIS). The ALO, PCL, OHP, and BIS lidars are compared in Table 1. For the ALO lidar the product is 2.7 and for the PCL the product is 63.7. The 2.6-m diameter telescope enables the return signal from the PCL lidar to reach a higher altitude than that of the ALO lidar for an equivalent integration time and for the uncertainty at overlapping altitudes to be much smaller. The two French lidars are separated by 550 km and the results are combined into a single climatology and will be referred to as OHP from this point on. The values for the second system are given in the parenthesis. The ALO lidar is undergoing an upgrade to the telescope with an equivalent diameter of 2.54 m such that when finished, the resulting power aperture product will be 91 W-m^2. Until that time comes we are

operating whenever possible to increase the number of measurements in an attempt to make up the difference. One advantage for ALO is the height of the lidar above sea level. By being 1.4 km above sea level, we gain by not losing signal due to atmospheric absorption.

Table 1. Comparison of Rayleigh-Scatter Lidar Systems [*Wickwar et al.*, 2000]

LIDAR	**Energy (mJ)**	**Rep. Rate (Hz)**	**Telescope Diameter (m)**	**Power Aperture Product (W-m^2)**
ALO	600	30	.44	2.7
PCL	600	20	2.6	63.7
OHP (BIS)	400 (200)	15 (50)	.8 (1.2)	3.0 (11.3)

CHAPTER 3

DATA REDUCTION – THEORY

The basis for Rayleigh lidar is molecular or what is frequently called Rayleigh scatter from which it derives its name. In Rayleigh scattering the incident radiation induces an electric dipole in the molecule. This induced electric dipole oscillates at the same frequency as the incident radiation and produces a photon at the incident frequency. Furthermore theory states the scattering is directly proportional to the product of the atmospheric density and the Rayleigh backscatter cross section. The Rayleigh scattering cross section is dependent upon the wavelength of light that is scattered. Because the light is produced with a laser and is spectrally narrow and the middle atmosphere is well mixed, the backscatter cross section can be assumed to be a constant. For the standard atmospheric constituents up to an altitude of 100 km the Rayleigh backscatter cross section is given by equation 3.1.1 [*Measures*, 1992]

$$\sigma_{\pi}^{R}(\lambda) = 5.45\left[\frac{550}{\lambda(nm)}\right]^{4} \times 10^{-28} cm^{2} sr^{-1}. \qquad 3.1.1$$

Consequently, when corrected for range the returns are profiles of relative density once above the aerosols that may reach to 30 km. Since the backscatter cross section varies as λ^{-4}, a significant gain in the return signal will result if the wavelength of the laser is shortened. Thus by using the first harmonic of the laser there is a gain of sixteen, but at only half the power, so the net gain is a factor of eight. The second advantage to doubling the frequency of the laser is it is now visible and easier to work with. The development of the theory follows that of *Beissner* [1997].

1. Relative Densities

The number of backscattered photons *N(h)* due to a laser pulse of N_0 photons will be proportional to the product of the energy output of the laser, the square of the atmospheric transmission of light between the lidar and the scattering altitude, the molecule cross section for Rayleigh backscatter, the efficiencies of the receiver system, and the range squared corrections as given in equation 3.1.2.

$$N(h) = \frac{N_0 A Q T^2(h)}{h^2}\left[n(h)\sigma_\pi^R\right]. \qquad 3.1.2$$

Here *h* is the height above the lidar, *n(h)* is the atmospheric number density, *A* is the telescope area, *Q* is the optical efficiency of the lidar system, and *T(h)* is the atmospheric transmittance. The lidar equation may be inverted to give the relative molecular density as a function of altitude in terms of the measured quantities above a reference altitude h_0.

It is difficult to make absolute measurements of density because of the changing atmospheric transmission from aerosols and clouds (Figure 3), from temporal changes in laser power (aging flashlamps, delay of Q-switch trigger after flashlamps, polarizer at entrance to doubling crystal housing, orientation of doubling crystal), changes in alignment of laser beam and telescope, and from changing O^3 absorption at 532 nm in the stratosphere. Hence it is preferable to work with relative densities

$$n(h) = n(h_0)\frac{N(h)}{N(h_0)}\frac{h^2}{h_0^2}\frac{T^2(h_0)}{T^2(h)}. \qquad 3.1.3$$

Unlike the basic lidar equation the measurements of the relative density measurements have no dependence upon the optical efficiency of the lidar system, or the backscatter cross section. By 45 km we are above the majority of the atmosphere, and the changes

in the transmittance are small enough so $T(h) \approx T(h_0)$. In order to develop an absolute measurement of the atmospheric density, we must normalize the relative density profile to either measurements or models. (However, that is not the goal of this work.)

2. Absolute Temperatures

Under the assumptions the atmosphere is comprised of an ideal gas in hydrostatic equilibrium it is possible to derive temperature from the relative density [*Hauchecorne and Chanin*, 1980; *Chanin*, 1984; *Chanin and Hauchecorne*, 1984; *Gardner et al.*, 1989]. By integrating the relative density over some altitude range an absolute measurement of temperature is obtained. Again given the long integration times used to derive accurate temperature measurements, the assumption of hydrostatic equilibrium is accurate.

The steady-state diffusion equation or hydrostatic equilibrium equation is the balance between the gravitational force and the pressure gradient

$$\frac{dP}{dh} + n(h)m(h)g(h) = 0 . \qquad 3.2.1$$

Here $m(h)$ is the mean molecular mass of the atmosphere, $n(h)$ is the number density, and $g(h)$ is gravitational acceleration. The equation for hydrostatic equilibrium may be combined with the ideal gas law,

$$P(h) = n(h)kT(h) , \qquad 3.2.2$$

to give the relationship

$$k\frac{d(n(h)T(h))}{dh} = -n(h)m(h)g(h) . \qquad 3.2.3$$

Here $P(h)$ is the pressure, $T(h)$ is the temperature, and k is Boltzman's constant. This equation is easily integrated over the altitude region from h, the altitude of interest, to

some particular reference altitude h_0,

$$k\left[n(h_0)T(h_0) - n(h)T(h)\right] = -\int_h^{h_0} n(h')m(h')g(h')dh' \quad 3.2.4$$

It is now possible to solve for the temperature *T(h)* at our altitude on interest.

$$T(h) = T(h_0)\frac{n(h_0)}{n(h)} + \frac{1}{kn(h)}\int_h^{h_0} n(h')m(h')g(h')dh' \quad 3.2.5$$

In this form any error in the measurement of the relative density will enter into the equation. The error in the measurement may even cause the temperature to diverge through the $\frac{n(h_0)}{n(h)}$ ratio. If however, we choose h_0 to be some initial maximum starting altitude h_{max} and the integration is done to some lower altitude

$$T(h) = T(h_{\max})\frac{n(h_{\max})}{n(h)} + \frac{1}{k}\frac{n(h_{\max})}{n(h)}\int_h^{h_{\max}} \frac{n(h')}{n(h_{\max})}m(h')g(h')dh' \quad 3.2.6$$

In this form any of the system-dependent parameters of density divide out of the temperature calculation. The measurements of density are relative. However as the temperature is derived from the ratio of two relative measurements, the temperature becomes an absolute measurement (except for the 1st term, which decreases with altitude).

The temperature algorithm is based upon an initial temperature at the chosen h_{max}. We choose h_{max} to be the altitude in which the signal is 16 standard deviations. The initial temperature for this altitude must be provided from some source outside of the Rayleigh lidar. This temperature may be from a model or other observations. Currently if the altitude is above 83 km, the starting temperatures are taken from the temperature climatology from the sodium lidar at Colorado State University (CSU) [*She et al.*, 2000]

and interpolated for the correct date and altitude. However, if the starting altitude is below 83 km the starting temperature is based both upon the MSISe90 [*Hedin et al.*, 1991] model and the sodium climatology. The offset between the climatology and the model at 83 km at midnight is used to offset the starting temperatures at lower altitudes from the model. The IDL code for the temperature reduction is outlined in Appendix B.

3. Measurement Error

The return profiles are a sum of 3600 separate soundings of the atmosphere made by the lidar system. These profiles can be considered to consist of up two different signals, the Rayleigh-scatter signal *S* and the background noise signal *N*. It is then possible to separate the Rayleigh-scatter signal from the total if the background is known.

$$S_j = \frac{1}{I}\sum_{i=1}^{I}(S+N)_{ij} - \frac{1}{K}\sum_{k=1}^{K}N_{kj} = (\overline{S+N})_j - \overline{N}_j . \qquad 3.3.1$$

Here *I* and *K* denotes space and *J* denotes time. The background is measured at a different altitude than the Rayleigh Scatter signal, and is assumed to be constant. This assumption places certain requirements on the data selection.

Variations in the return signal and the background can also be calculated. First is the background variance

$$dN_j = \sum_{k=1}^{K}\frac{\partial N_j}{\partial N_{kj}}dN_{kj} = \frac{1}{K}\sum_{k=1}^{K}dN_{kj} . \qquad 3.3.2$$

Square and add, assuming each N_{kj} is independent. Let

$$\sigma_x^2 = (dx)^2 . \qquad 3.3.3$$

Then

$$\sigma_{N_j}^2 = \frac{1}{K^2}\left(\sum_{k=1}^{K}\sigma_{N_{kj}}^2\right) \qquad 3.3.4$$

assuming the background is constant then

$$\frac{1}{K^2}\left(\sum_{k=1}^{K}\sigma_{N_{kj}}^2\right) = \frac{\sigma_N^2}{K} \qquad 3.3.5$$

gives the noise variance for an average over K altitudes. The variance in the combined signal can be calculated by

$$d(S+N)_j = \sum_{i=1}^{I}\frac{\partial(S+N)_j}{\partial(S+N)_{ij}}d(S+N)_{ij} = \frac{1}{I}\sum_{i=1}^{I}d(S+N)_{ij}\ . \qquad 3.3.6$$

Square and add, assuming each $(S+N)_{ij}$ is independent.

$$\sigma_{(S+N)_{ij}}^2 = \frac{1}{I^2}\sum_{i=1}^{I}\sigma_{(S+N)_{ij}}^2\ . \qquad 3.3.7$$

We now have calculations for the variance of the noise and the combined signal and noise. The variance for the signal alone (Eq 3.3.1) is given by

$$\sigma_{S_j}^2 = \sigma_{(S+N)_j}^2 + \sigma_{N_j}^2 = \frac{1}{I^2}\sum_{i=1}^{I}\sigma_{(S+N)_{ij}}^2 + \frac{1}{K^2}\sum_{k=1}^{K}\sigma_{N_{kj}}^2\ . \qquad 3.3.8$$

Due to the fact the return signal follows Poisson statistics $\sigma_x^{\,2} = x$, we can substitute the return signal in place of the variance

$$\sigma_{S_j}^2 = \frac{1}{I^2}\sum_{i=1}^{I}(S+N)_{ij} + \frac{1}{K^2}\sum_{k=1}^{K}N_{kj}\ . \qquad 3.3.9$$

Or, using the altitude averages, we get

$$\sigma_{S_j}^2 = \frac{1}{I}(\overline{S+N})_j + \frac{1}{K}(\overline{N})_j\ . \qquad 3.3.10$$

If there are other factors in adding to the variability in the measurements, then our uncertainties will be underestimates. Ignoring the assumption of hydrostatic equilibrium

for a moment, the temperature profiles derived from a single two-minute profile do not have enough precision to obtain useable temperatures at higher altitudes. A temporal average is required to do so. This temporal averaging of the return signals will enter into the averages as follows:

$$\left\langle \overline{S+N} \right\rangle = \frac{1}{J}\frac{1}{I}\sum_{j=1}^{J}\sum_{i=1}^{I}(S+N)_{ij} = \frac{1}{J}\sum_{j=1}^{J}(\overline{S+N})_j \,, \qquad 3.3.11$$

$$\left\langle \overline{N} \right\rangle = \frac{1}{J}\frac{1}{K}\sum_{j=1}^{J}\sum_{k=1}^{K}N_{kj} = \frac{1}{J}\sum_{j=1}^{J}(\overline{N})_j \,. \qquad 3.3.12$$

Their variances are given by

$$\sigma^2_{\left\langle \overline{S+N} \right\rangle} = \frac{1}{J}\frac{1}{I}\left\langle \overline{S+N} \right\rangle \qquad 3.3.13$$

and

$$\sigma^2_{\left\langle \overline{N} \right\rangle} = \frac{1}{J}\frac{1}{K}\left\langle \overline{N} \right\rangle. \qquad 3.3.14$$

Recalling the Rayleigh-scatter signal is the difference between these two averaged measurements, it is given by

$$\left\langle \overline{S} \right\rangle = \left\langle \overline{S+N} \right\rangle - \left\langle \overline{N} \right\rangle, \qquad 3.3.15$$

and its variance is given by

$$\sigma^2_{\left\langle \overline{S} \right\rangle} = \sigma^2_{\left\langle \overline{S+N} \right\rangle} + \sigma^2_{\left\langle \overline{N} \right\rangle} = \frac{1}{J}\frac{1}{I}\left\langle \overline{S+N} \right\rangle + \frac{1}{J}\frac{1}{K}\left\langle \overline{N} \right\rangle. \qquad 3.3.16$$

Thus the standard deviation of the signal is

$$\sigma_{\left\langle \overline{S} \right\rangle} = \sqrt{\frac{1}{J}\frac{1}{I}\left\langle \overline{S+N} \right\rangle + \frac{1}{J}\frac{1}{K}\left\langle \overline{N} \right\rangle}. \qquad 3.3.17$$

As stated earlier, we need to know when the signal is 16x the standard deviation. The

number of standard deviations is given by

$$\frac{\langle \overline{S} \rangle}{\sigma_{\langle \overline{S} \rangle}} = \frac{\langle \overline{S+N} \rangle - \langle \overline{N} \rangle}{\sqrt{\frac{1}{J}\frac{1}{I}\langle \overline{S+N} \rangle + \frac{1}{K}\frac{1}{J}\langle \overline{N} \rangle}}. \tag{3.3.18}$$

Having calculated the variance of the measurement, it is now possible to find the uncertainty for the temperature measurements. It is possible to find the variance of the temperature in much the same way we have for the backscatter signal. Using the temperature calculation Eq. 3.2.6, we can propagate the uncertainties in the return signal and derive an uncertainty for the temperature profile [*Gardner et al.*, 1989]

$$dT = \frac{\partial T}{\partial T_{\max}} dT_{\max} + \frac{\partial T}{\partial n_{\max}} dn_{\max} + \frac{\partial T}{\partial n} dn. \tag{3.3.19}$$

$$\begin{aligned} dT = {} & \frac{n_{\max}}{n(h)} dT_{\max} + \frac{T_{\max}}{n(h)} dn_{\max} - \left(\frac{T_{\max} n_{\max}}{n(h)} + \frac{mg}{kn(h)} \int_h^{h_{\max}} n(h')dh' \right) \frac{dn}{n(h)} \\ & + \frac{mg}{kn} \frac{\partial}{\partial n} \left(\int_h^{h_{\max}} n(h')dh' \right) dn. \end{aligned} \tag{3.3.20}$$

The last term on the right in Eq. 3.3.20 can be simplified. Letting

$$c = \frac{mg}{k} \text{ and } \frac{\partial}{\partial n} = \frac{d}{dn} \Rightarrow dn = \left(\frac{dn}{dh} \right) dh. \tag{3.3.21}$$

The number density n increases with decreasing altitude by the scale height H given by

$$n(h) = n_{\max} e^{-\frac{h_{\max} - h}{H}}. \tag{3.3.22}$$

As such

$$\frac{dn}{dh} = -\left(\frac{n}{H} \right). \tag{3.3.23}$$

And

$$\frac{c}{n}\frac{\partial}{\partial n}\left(\int_h^{h_{\max}} n(h')dh'\right)dn = \frac{c}{n}\left[n(h_{\max})\frac{dh_{\max}}{dn} - n(h)\frac{dh}{dn}\right] = \\ -\frac{c}{n}\left[n(h_{\max})\frac{H_{\max}}{n(h_{\max})} - n(h)\frac{H}{n(h)}\right] = -\frac{c}{n}\left[H_{\max} - H\right]. \quad 3.3.24$$

The final term is zero for a constant scale height. The temperature variance becomes

$$\sigma_T^2 = \left[\frac{n_{\max}}{n(h)}\right]^2 \sigma_{T_{\max}}^2 + \left[\frac{T_{\max}}{n(h)}\right]^2 \sigma_{n_{\max}}^2 + \left[\frac{T(h)}{n(h)}\right]^2 \sigma_n^2 . \quad 3.3.25$$

Substituting Eq 3.3.22 into Eq 3.3.25 we find the final calculation of the temperature variance

$$\sigma_T^2 = T^2\left(\frac{\sigma_n}{n}\right)^2 + \left[\sigma_{T_{\max}}^2 + T_{\max}^2\left(\frac{\sigma_{n_{\max}}}{n_{\max}}\right)^2\right] e^{\frac{-2(h_{\max}-h)}{H}} . \quad 3.3.26$$

T and n are the temperature and number density at h, T_{max} and n_{max} are the temperature and number density at the top altitude, h_{max}, and H is the atmospheric scale height, which is assumed to be constant at 7 km. The first term in the equation is derived from the ideal gas law. The second term is based upon the uncertainty from the initial temperature, and decreases with height. Typically in the calculated error, the uncertainty in the starting temperature is assumed to be zero, which is not the case. This uncertainty is difficult to determine, but it will be shown in Chapter 4 how this possible source of error decreases rapidly with altitude.

CHAPTER 4

DATA REDUCTION – IMPLEMENTATION & INTRODUCTION

The goal of the Rayleigh-scatter lidar is to produce accurate temperature measurements. Compared to many other types of lidar systems, for example resonance and DIAL, a Rayleigh-scatter lidar is straightforward. In practice the operation of any lidar requires a certain amount of skill and experience. The major obstacles to accurate temperatures are systematic errors. These arise from errors in the data analysis or problems with the instrumentation itself, both of which can be subtle effects.

1. Algorithm for Determining the Temperatures and their Uncertainties

The Purple Crow Lidar (PCL) operates both a Rayleigh-scatter lidar system and a sodium resonance lidar. The measurements from the PCL's Rayleigh lidar are very similar to those made by ALO's Rayleigh system [*Sica et al.*, 1995] as they are located at almost the same latitude and cover the same time period. The transmitter for the PCL lidar operates at 67 percent of the power of the ALO system, but the PCL telescope is larger. The PCL lidar employs a liquid mercury mirror for its primary. A parabolic shaped container holding the mercury is rotated at ~ 6 rpm to produce an inexpensive large-diameter parabolic mirror. The container has a parabolic shape not to guide the mercury to take this form, but just too minimize the amount of mercury used in the mirror as there is a weight limit to the air bearing used. The PMT is located at the prime focus of the telescope, which obscures a small portion of the primary mirror.

Both of the Rayleigh lidar systems are using the data reduction procedure outlined

in the previous chapter. For the purposes of comparing temperature-reduction routines used by both lidars, the PCL group provided us with raw lidar data along with their temperature results. The first comparison showed a small difference between the two reductions. It was soon discovered the simple gravity calculation used by the ALO lidar was too simplistic and a new routine was needed. The Taylor's series expansion used by the PCL lidar [*Jursa*, 1985] has been updated by the National Imagery and Mapping Agency, but this update included a more complete calculation now used by the ALO lidar [*NIMA*, 2000] in which the normal component of gravity is calculated. The errors due to gravity in Figure 4 were at most 2 degrees, but this is much larger than the measurement.

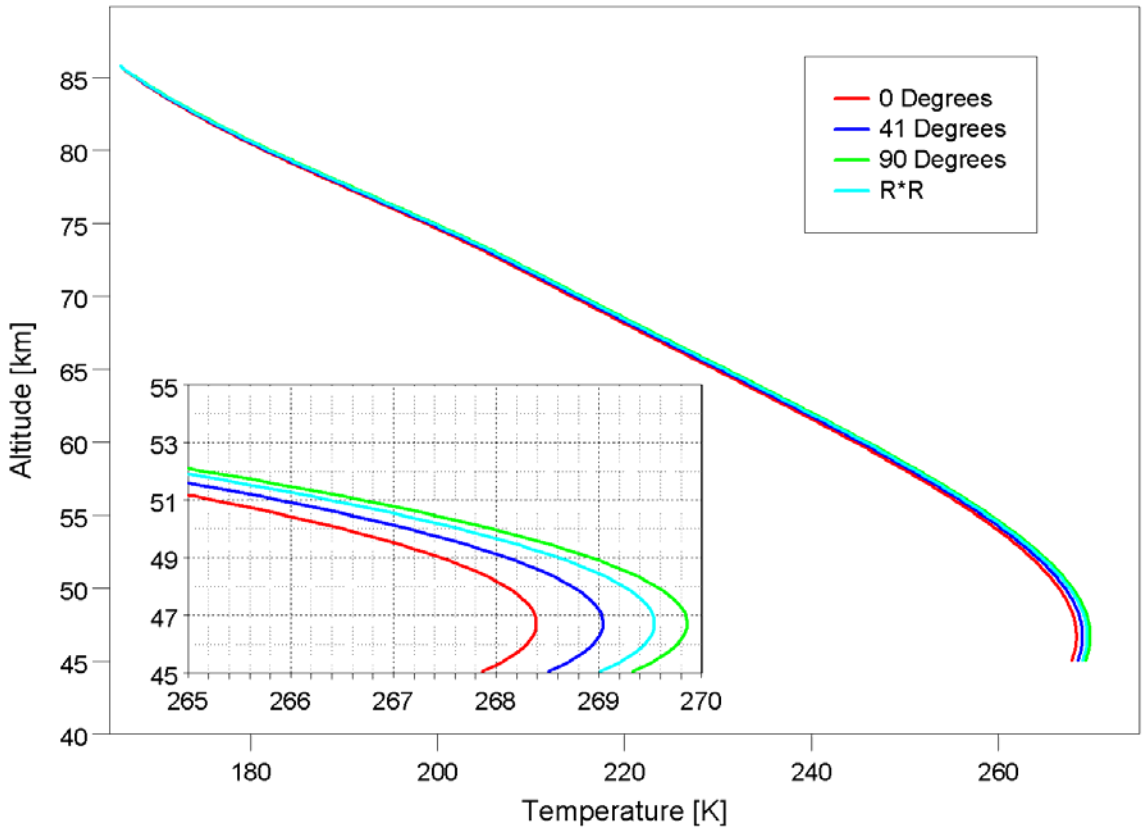

Figure 4. Variations in temperature due to gravity error.

This comparison was important as it eliminated a small systematic error in the climatology.

The new gravity calculation requires not only latitude, but also longitude and is outlined in Appendix A. While the changes in the longitude produce little change in the temperature, changing the latitude did. Figure 4 gives the variations in the deduced temperature due to the variation in latitude and a simple $1/R^2$ fall off with altitude. The variations in the deduced temperature profiles due to the calculation of gravity are small, but they were another source of systematic errors.

After changing the calculation of gravity used by the ALO lidar it was possible to compare the results of the two different temperature-reduction procedures. While the two temperature profiles are certainly from the same data set, there are some obvious differences between the two procedures (Figure 5). The starting altitudes, and therefore temperatures, are different for the two data reduction algorithms. Other differences between the calculated temperature profiles arise from the amount and manner of averaging done to the raw data. After the first few kilometers, the temperatures are in very close agreement all the way down to 45 km. If there were systematic errors in either data reduction procedure, the temperature curves would separate near the bottom. This gives a good independent confirmation of our data reduction procedure. It also means in the future, we can compare temperatures between the two locations and be reasonably sure differences are geophysical.

To further test the temperature-reduction programs that were used in the climatology, a simulation of the lidar returns was developed. The MSISe90 atmospheric

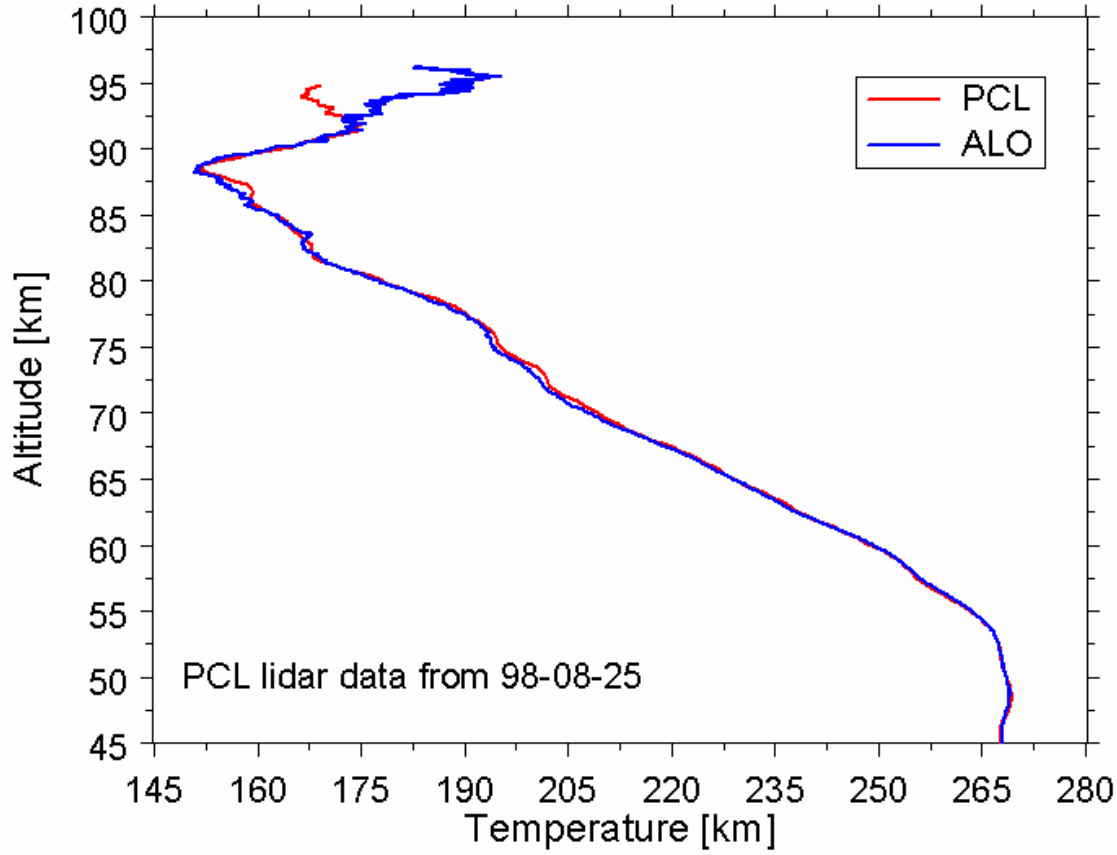

Figure 5. Comparison of temperature-reduction algorithms. The data were taken with the Purple Crow Lidar (PCL) and reduced by both groups. The red profile is from the PCL reduction and the blue is from the ALO reduction. (Different initial altitudes and temperatures were used.) [Courtesy of R.J. Sica and P.S. Argall.]

model was the basis for the lidar simulation because it provides profiles of both temperature and density, and they are related through hydrostatic equilibrium and the ideal gas law [*Hedin*, 1991; *Leblanc et al.*, 1998]. A midnight summer density profile was normalized and multiplied by one over the range squared so it would have essentially the same characteristics as the returns from the lidar system. The normalization is to the standard count rate seen with the lidar, which is only 300 counts in two minutes at 45 km. Using the standard temperature-reduction algorithm for the lidar data reduction, it is

possible to take the modeled lidar return and calculate the resulting temperature. Using a starting temperature from the MSISe90 model, the derived temperatures are highly accurate. As seen in Figure 6, the temperatures from the MSISe90 temperature profile closely match the temperatures that were calculated from the MSISe90 density profile using the ALO temperature-reduction algorithm. The differences between the two temperature profiles are quite small; they can simply be attributed to differences in values used in the model, for instance, for the variation of gravity with altitude.

The propagation of Poisson statistics through the Rayleigh lidar temperature

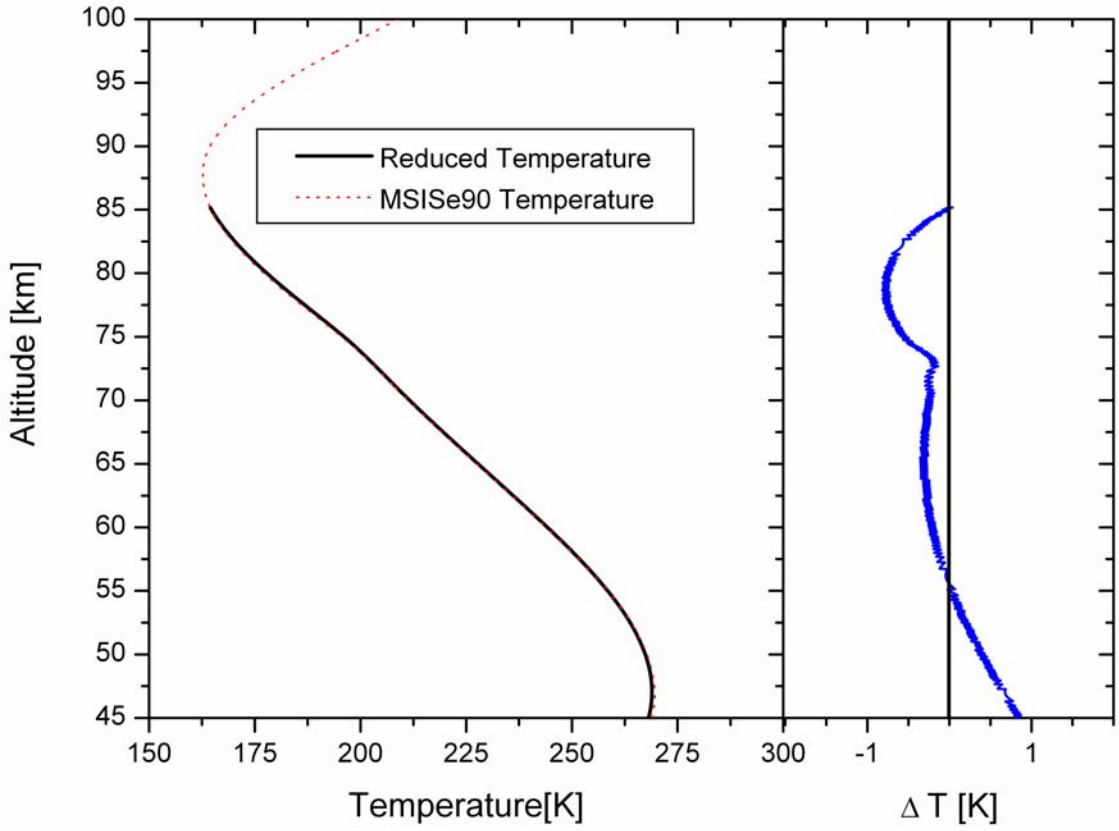

Figure 6. Temperature results derived from MSIS densities using the ALO temperature-reduction algorithm compared with the MSIS temperatures. The right-hand plot is the temperature difference

equation was necessary to produce an equation to give the measurement uncertainty [*Gardner et al.*, 1989] as reviewed in Chapter 3. It is difficult to verify this error propagation using the return from the lidar system as it is subject to a large amount of geophysical variation along with the measurement noise. Using the lidar model, it was possible to generate thousands of profiles that contain only the variation due to Poisson statistics. In this manner it was possible to calculate the uncertainty in the temperatures from the formula, and also to calculate the actual RMS variation of the signal. A model run was completed simulating the returns from a single one-hour temperature profile (Figure 7).

For large numbers of profiles, these two calculations give the same uncertainties. Figure 8 shows the results that verify the error propagation method as being a proper manner to calculate the error bars for the temperature measurements. The reason the error propagation curve goes to a higher altitude is it used a different averaging method. The RMS value was calculated using the mean temperature profile from 50 one-hour temperature profiles. The error propagation curve was calculated using the average density profile for all 50 one-hour profiles. This increased the signal-to-standard deviation ratio of the profile, enabling temperature derivations to a higher altitude than found using the one-hour integrations. (It is also important to note because of the large number of one-hour integrations used to calculate the temperature uncertainty, the resultant error bars are smaller than those normally seen with the Rayleigh-scatter lidar system.) The differences between the two methods for calculating the error in the temperature measurements are very small. Overall the results show the two methods are

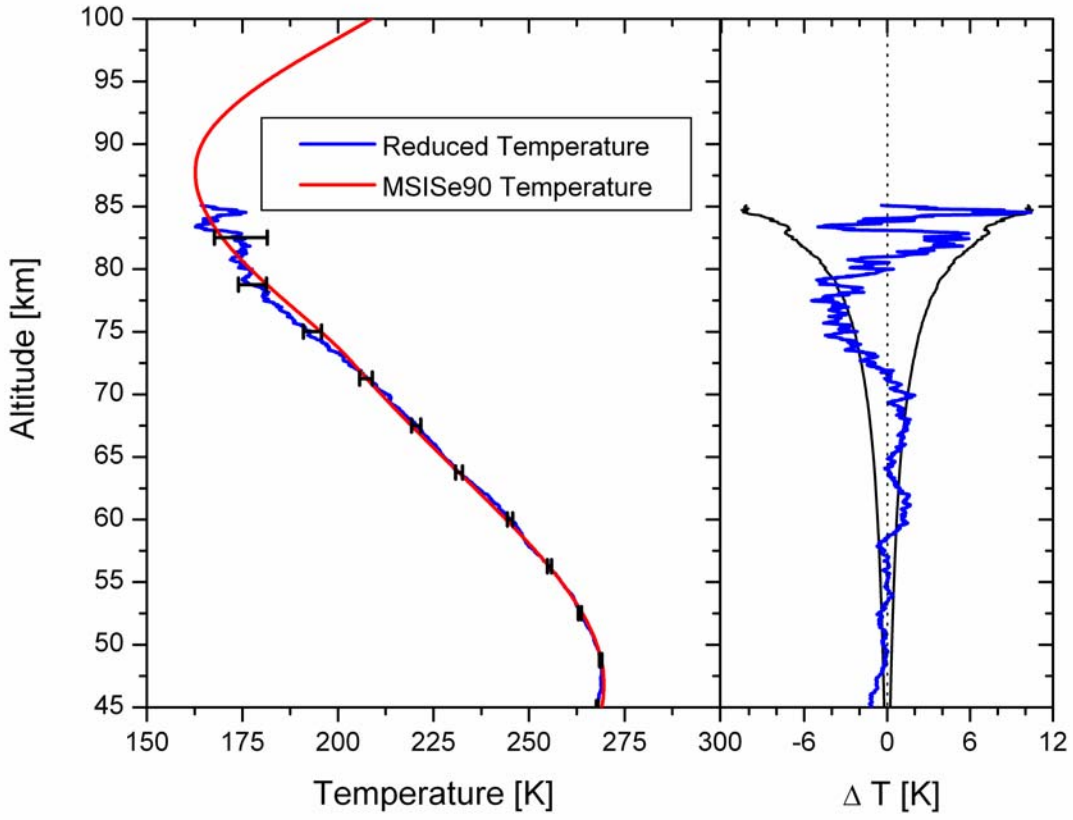

Figure 7. Model results corresponding to an hour integration and its associated error bars. The right-hand plot also gives the error bars (black) along with the difference from the MSIS model (blue).

equivalent, and the error propagation can be used with confidence.

2. Possible Systematic Errors

The next task is to determine the effects of any measurement uncertainties or possible systematic errors. As was detailed in Chapter 3, the method by which the temperatures are found from the relative density requires an initial starting temperature for the data reduction. As a Rayleigh lidar cannot produce its own starting temperature, it must rely on an external temperature value. Typically the starting temperatures for

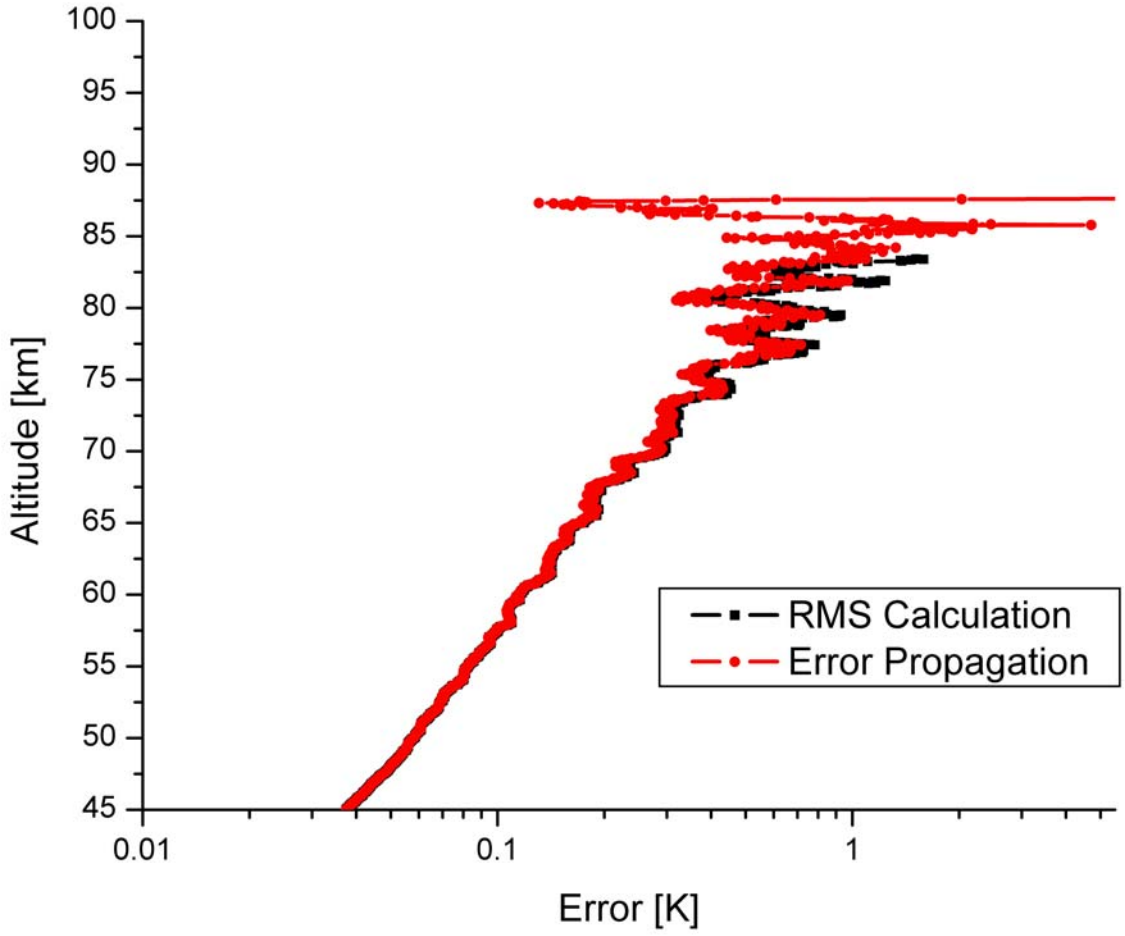

Figure 8. Simulation results of error propagation. Using 50 one-hour profiles with Poisson uncertainty, the black curve shows the RMS temperature uncertainty. The red curve shows the temperature uncertainty using Eq. 3.3.23.

Rayleigh-scatter lidars are taken from an empirical model such as MSISe90 or, in our case a combination of MSISe90 and the temperature climatology from the Fort Collins sodium lidar at Colorado State University [*She et al.*, 2000]. These starting temperatures are taken from long-term climatology measurements and do not show the day-to-day geophysical variations. The uncertainty in these initial values for a given hour or night is unknown. However, because we are primarily focusing on the development of our own climatology

from our data, using a climatology from a facility relatively close to ours greatly reduces the likelihood of introducing large errors in the starting temperatures.

The short-term nightly geophysical variability in the middle atmosphere between the altitudes of 84 and 104 km is ± 14 K [*She et al.*, 2000]. These short-term variations in the temperature introduce uncertainty, particularly into the nightly temperature average. Any errors in the starting temperature are removed from the temperatures as the profile is integrated downward. This is due to the first term to the right of the equal sign in equation 3.2.6. The influence of the temperature profile decreases as the density of the atmosphere increases. This decreasing effect is seen in Figure 9 where an error in the starting temperature was added in 5 K increments from +20 K to -20 K. The +20 K case is a good example of how the introduced error is minimized by integrating downward. The difference between the two profiles after 10 km has been reduced to ~ 3 K, and is ~ 1 K after 20 km. The short-term variability of the middle atmosphere does not enter into the climatology due to the temporal averaging used. This does not mean by using the temperature measurements from the Fort Collins lidar we have eliminated any error in the starting temperature, but we feel for the climatology, the values should be close. The published climatology from Fort Collins covers a period from 1990 until 1999. The earliest measurements made by the USU lidar started in 1993. Dr. She reports an atmospheric cooling of 1 K/yr in his temperature measurements in addition to the effects seen from Mt. Pinatubo [*She et al.*, 1998]. These effects may produce a constant bias in the starting temperature that can produce an error of a few K in the first few kilometers of

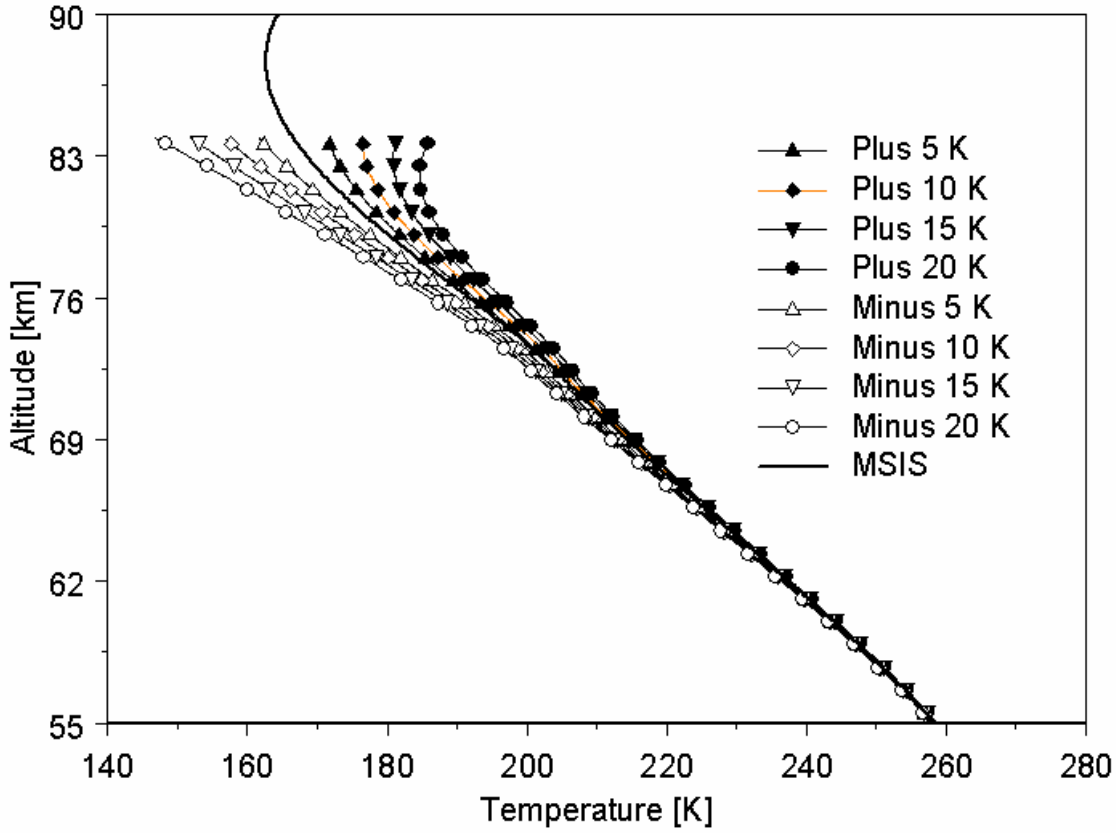

Figure 9. Systematic effects of an error in the initial temperature on the reduced temperatures.

our reduced temperatures.

The presence of signal-induced noise in the lidar returns is another concern. The response of the PMT to light can vary during the 3.5 ms data acquisition window. If the effect is small, it is hard to detect in a single two-minute profile. Usually these smaller effects only appear after the data reduction has taken place. With the lidar model, it is possible to test different kinds of variations to the background level and see their effects on deriving the correct temperature profile. In making the temperature measurements, it has always been assumed the variations in the background level are constant over the full altitude range or if they are not constant, then will vary over long time scales so it is

essentially constant for any given profile. Utilizing the lidar model it is possible to add variations to the background level. The actual variations are usually far less than one percent. However, to show what can occasionally happen, we made changes on the order of one to five percent of the total background level of five counts in the modeled returns. The effects of these unusually large variations were significant on the reduced temperatures.

The starting point for these temperature-reductions was fixed at 16 standard deviations. As a result, small changes in the background level will change the starting altitudes (Figure 10). A five percent decrease to the background level causes the lidar signal to be higher than normal. This overestimation of the signal causes the sixteen

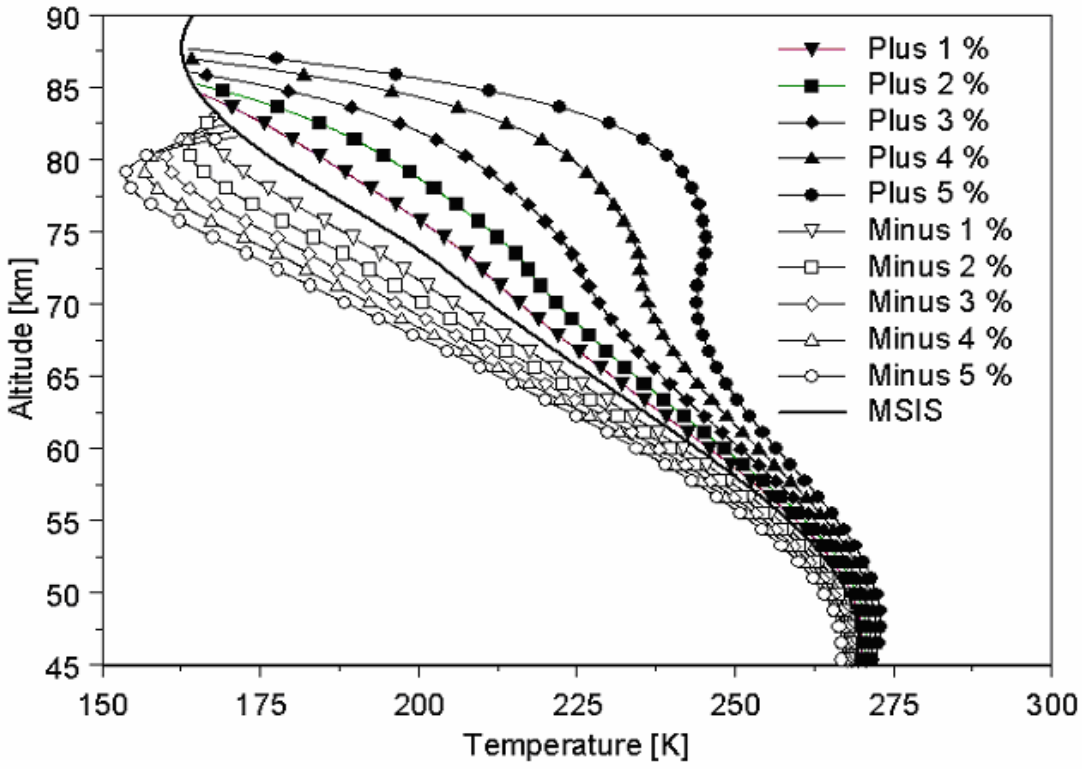

Figure 10. Errors in temperature due to small error in the background subtraction.

standard deviation points to increase in altitude by 5 km. These small changes in the background level produced significant changes in the resulting temperatures. While errors in the starting temperature diminish greatly with height, the errors from the background level produced effects that were still significant after 40 km of integration. In fact, for the five percent case, the error in the derived temperature was still 3 K after integrating downward for 40 km. While the temperature profile for the five percent case at a glance is obviously incorrect, a smaller error may produce errors in the temperature that are not detected as the nightly variation in temperature would mask any slight temperature effect.

The error in the Rayleigh-scatter signal due to errors in the background subtraction is a small fraction of the total signal at lower altitudes. By lowering the starting altitude, the effects of any errors in the background level can be minimized. Likewise, measurements that do not produce good results in the upper mesosphere can still produce accurate measurements of the lower mesosphere by starting the temperature-reduction at a much lower altitude.

To minimize the amount of error in the measurement of the background, a large number of gates, typically 1000, are used to find an average background value. The measurement uncertainty in the background is much smaller than any of the errors used in this lidar simulation when the lidar is working properly. Using Eq. 3.3.14 the uncertainty in the background signal is given in Table 2 for one-hour integrations from the ALO lidar. The percent error in the background measurement is a fraction of a percent. The uncertainty in the background value for good data is far smaller than the

values used in Figure 6. Table 2 lists the uncertainties in the background level typically the background level is less than 10 counts/bin. There were some nights with bad backgrounds that did produce temperature similar to those in Figure 6. These nights were eliminated from the climatology. By varying the range of gates over which the background level is calculated, it is possible to vary the background by more than the uncertainty in the background.

As mentioned in Chapter 3, the background level in the region where we have Rayleigh scatter is unknown and must be approximated from higher altitudes. This requires the performance of the PMT be consistent or ideally linear. In making the temperature analysis, there were certain temperature profiles that appeared to be non-physical. These non-physical temperatures compared well with those results from the lidar simulation of the systematic errors.

The starting altitude for the temperature data reduction is fixed to the point where the signal is 16 times the standard deviation. This 16 standard-deviation level was initially produced by guesswork: it seemed to produce good results. Using the lidar simulation, it was possible to examine this assumption. The number of standard

Table 2. Background Uncertainties Based upon Poisson Statistics. The noise or background level is listed in the left-hand column with the variance and standard deviation given. The right-hand column gives the percentage error in the background for a one-hour profile.

$\langle \overline{N} \rangle$	$\sigma^2_{\langle \overline{N} \rangle}$	$\sigma_{\langle \overline{N} \rangle}$	$\frac{\sigma_{\langle \overline{N} \rangle}}{\langle \overline{N} \rangle} 100$
1	3.33×10^{-5}	0.0057	0.578 %
10	3.33×10^{-4}	0.0183	0.182 %
100	3.33×10^{-3}	0.0578	0.058 %

deviations was varied from 10 to 20. By lowering the number of standard deviations, the starting altitude was increased, but so was their density uncertainties, and hence the temperature uncertainties, at the highest altitude. Likewise by increasing the number of standard deviations, the starting altitude dropped as did the density and temperature uncertainty at the highest altitude.

If we did not care about the location of the starting point, it would make sense to start at a lower altitude where there is less noise in the data. Since we are using an initial guess as the starting temperature, we need to increase the starting altitude so when we integrate downward, there will be a larger region where the starting temperature has little effect on the results.

The difference in initial altitude between the 10 and 20 standard-deviation cases is only a few kilometers. The results from the lower standard-deviation cases produced greater uncertainty at the lower altitudes where their temperatures overlapped with the 16 standard-deviation case. The higher standard-deviation cases decreased the starting altitude too much. After looking at the results, it was decided the initial point should be near the middle of the region we tested. As a result we have continued to use the 16 standard-deviation level for the starting point for the temperature-reductions. This decision still needs to be more carefully evaluated, but can be left for future work.

3. Instrumentation Considerations

So far, we have shown the data reduction routine employed produces the correct temperature profile from the relative density profile. The main possible source of systematic error remaining is from making the observations. There are several potential

problems in making accurate measurements with the lidar system. The foremost of these is for the detector system to respond linearly to the incident light.

The linearity of the pulse-counting electronics and the dead time between successive range bins is vital for making accurate measurements. The pulse-counting electronics should be able to switch from one range bin to the next with no time gap between them. If a gap is present, the ranging of the lidar system will be incorrect producing errors in temperature and altitude, and the counts will be fewer than they should be. These effects may be corrected, but it is necessary to make accurate measurements of the gap between bins to do so.

If the pulse-counting electronics are not able to respond fast enough to the incoming pulses, they will produce incorrect measurements. Even when the average count rate is low, this can happen because the photons do not arrive uniformly in time. The overall signal level will be lower than normal. This in turn will cause the starting altitude to be lower than it should be in the data reduction and the uncertainty to be greater. A fast-function generator was used to test the Multi-Channel Scalar (MCS) to ensure its linearity and to verify no dead time between range bins. The pulse length was set to 40 ns to simulate the electron pulses from the 9954 PMT and pre-amp. The linearity test is shown in Figure 11.

Looking back to Figure 3, we see for a typical two-minute profile the maximum count rate is about 1000 counts. But this is over 3600 soundings of the atmosphere by the lidar system. The maximum count would be about one photon for every four laser pulses. Because each bin is 250 ns wide, we would have one photon every μs, which is a

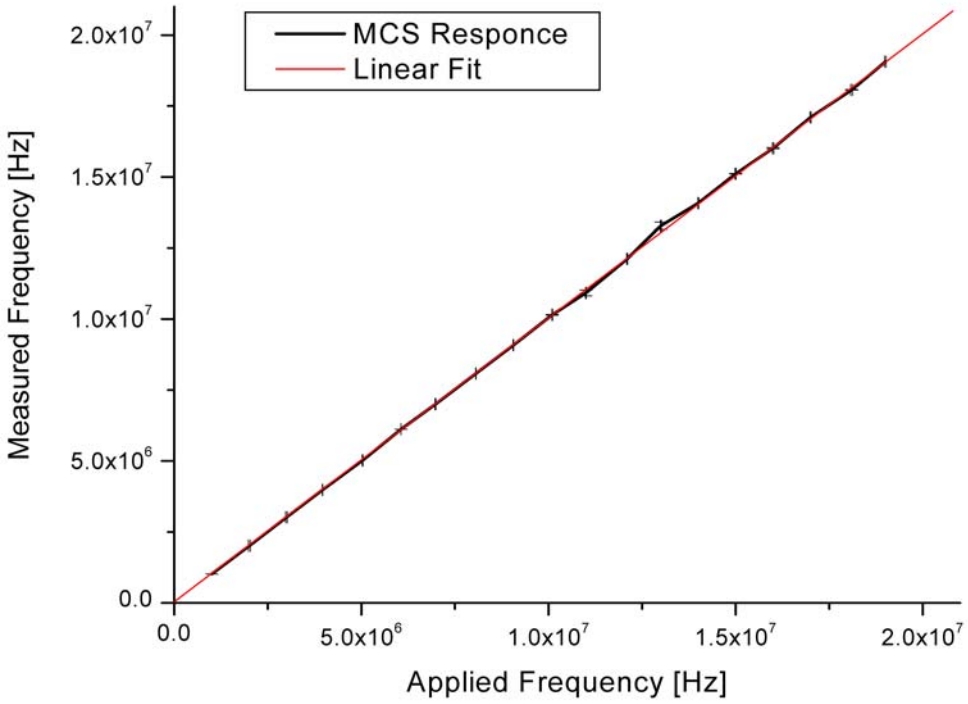

Figure 11. MCS frequency response.

frequency of 1 Mhz. Examining Figure 11, we see the MCS was tested in the lab out to almost 20 Mhz. These faster rates are necessary because the backscattered photons arrive at random intervals and a single laser pulse might produce five photons in a single range bin (20 Mhz). The function generator was gated to produce a finite number of pulses, and we were able to test for undercounting from gaps between the range bins. There were no measurable gaps between range bins. With its high linear response to high count rates and no gaps between range bins, the MCS is ideal for counting the lidar return signal.

In addition to the MCS, the pulse counting electronics are dependent on the response of a small pre-amplifier. The amplifier must respond to the same or greater

frequency range than the MCS. Utilizing the same function generator as used in testing the MCS, but with the amplitude of the pulses lowered to about 40 mV representing the level of the pulse out of the PMT, a fast oscilloscope could examine the output. This arrangement showed the output pulse rate from the pre-amp multiplied the input pulse rate up to the maximum frequency of the function generator. Thus, the response of the pre-amp matched that of the MCS. In general, the counting electronics and amplifiers for our lidar perform ideally for a Rayleigh-scatter lidar system.

The receiving system for the lidar is a standard photon-counting system. A problem exists with this type of detector (PMT) in that as the signal level increases, the response becomes nonlinear [*Donovan et al.*, 1993]. This problem is commonly referred to as signal-induced noise (SIN) or detector saturation. Typically the small fluctuations in the gain of the detector are only seen in the background region. But if the fluctuations are in the region of the Rayleigh returns, it becomes impossible to correct for them.

As was discussed in Chapter 2, the PMTs must be protected from bright light. If exposed, the tube may not have a linear response for a few hours, have added noise, or may be permanently damaged. The optical chopper discussed in Chapter 2 prevents the illumination of the PMT from low-altitude light during operation. The electronic gating prevents large photoelectron fluxes from bright light from damaging the final dynodes. We have found both the chopper and electronic gating are needed to avoid creating SIN. Otherwise, the signal in the noise region may increase, decrease, or oscillate. In addition, one must also be careful in the handling of the tube when maintaining the system. The PMT should only be installed or removed from its housing in low light conditions as exposure to strong light will effect its behavior for several days.

The second item to consider is the electronics that control the PMT. The high-voltage power supply must be able to provide adequate current at the higher count rates. If not, the signal out of the PMT will not increase as much as the incident light. This has been tested and found to be linear.

The background signal has been affected not only by the strong signals, but also by electrical interference, loose grounding, moisture in the PMT housing and socket, and occasionally some unidentified sources. We have also found an intermittent problem with a stuck bit in the MCS, which will cause abnormally high count rates for a single two-minute profile. The vast majority of these problems create characteristic returns and can be identified when the data reduction routines are run. Some problems are subtle and a line is fitted to the background and the slope found. Data with a slope much greater than 10^{-4} counts/250 ns are considered bad.

4. Conclusions

The variation of *g* with altitude has been updated. In the future, when going to higher altitudes, the constancy of the mean molecular mass and the Rayleigh cross section may have to be re-examined. We have justified the use of the 16 σ starting point for the temperature-reduction. The simulation of the lidar signal has been important for the development of the reduction procedure and investigating potential systematic errors, such as wrong initial value and incorrect background value. Some groups use one PMT to cover the whole altitude range from 25 to 95 km. The count rate will be 20 times higher at the bottom than ours. Most systems are non-linear at this point. Some groups try to correct for this, but it is hard and uncertain. We are avoiding the nonlinear

problem by only going to 45 km. We are being very conservative. In the upgrade we will add additional low-altitude channels that will receive a fraction of the total return. The SIN we have seen is a common problem, and some groups have been able to use either a chopper or an electronic gate to avoid it. We believe you have to use both. Some groups have tried to fit the background with an exponential or a sloping line and extended the fit to lower altitudes. We are being more conservative as we require a straight line with almost no slope.

CHAPTER 5

DATA SELECTION

The database for the temperature measurements spans a period of 10 years starting in 1993 and continuing until the present. As a result, we have been conservative in the selection of data for the climatology.

1. Data Signal

Before the temperatures were compiled into a climatology, it was necessary to separate the good data from the bad. The lidar is able to operate with a mild cloud cover, but a solid cloud bank dramatically reduces the received signal. Because of this, a simple method is to check each two-minute profile for a minimum of 60 counts at 45 km. If the signal is lower than 60 counts, the data is not used in the temperature-reduction.

Nightly observations are typically averaged into one-hour profiles centered on the half hour. The choice of the one-hour integration time instead of an all-night integration is to allow for the short-term variations in the temperature profiles to be measured. Short-term fluctuations are typically from gravity waves. But tides and planetary waves lead to systematic changes in the hourly temperature data. Because the lidar system records data at two-minute intervals, the hourly profiles are typically an average of 30 profiles. If several of the two-minute profiles are removed due to clouds, then a minimum of 20 profiles are required to be included into the hourly temperature averages.

2. Background Signal

The selection of the background level is important for the data reduction. The

signal-to-standard deviation ratio determines the height at which the temperature-reduction starts. If the lidar is operated too close to dawn or dusk, the returns are lost in the background signal. There is also an intermittent problem with a sticky bit in the MCS that causes the data reduction to halt due to extremely large count rates. As such the background level of each two-minute profile is checked and must fall below 20 counts per range bin. The region of the lidar signal that is chosen to be the background region must be clear of spikes and bumps. To make sure the background is flat with no bumps present, a line is fitted to the background. The slope of the fit must be below 2.6E-2 counts/km for the night to be included.

3. The Data

Certain nights produce unusable temperature results due to the presence of noctilucent clouds, non-linear backgrounds, or other instrument problems. A complete list of lidar observations on approximately 900 nights, are given in Appendix C. The removal of the bad data results in a total of 593 nights of observations given in Table 3.

The limiting factor in making observations with the lidar has been the academic school year. It can be seen during the months of December, April, and May there is a sharp decline in the number of observations. This has been due primarily to final exams and the end of the semester. Also we are typically training new students to operate the lidar during the start of term. Some of the gaps in the data were also caused by switching lasers, lack of funding for the lidar, and equipment problems. There has been a sharp increase in the number of days the lidar was in operation in 2003 due to an increase in the number of observers. The climatology was prepared with all of the

available data up through the first week of August 2003.

Table 3. Number of Good Nights Used in the ALO Lidar Temperature Reduction

	1993	1994	1995	1996	1997	1998	1999	2000	2001	2002	2003	Total
Jan		8	9	1	5		4	1	5		10	43
Feb		5	8	6	7		5		6	2	6	45
Mar		14	14		8			1	3	3	8	51
Apr			6		3				5	2	10	26
May		3				4				3	12	22
Jun		6	10	1		6	5	18		3	14	63
Jul			7	9		7		15	17	6	16	77
Aug	1	11	15	7		3		14	16		3	70
Sep	4	19	9	8		5		15	7	1		68
Oct		9	7	10		11	21	10	2			70
Nov	5			8		8	10	5				36
Dec	4	2		4		9	3					22
	14	77	85	54	23	53	48	79	61	20	79	593

CHAPTER 6

TEMPERATURE MEASUREMENTS

1. Hourly Temperatures

The lidar system operates during the night when the solar zenith angle is more than 6 degrees below the horizon. As such, the start and stop times are set by the individuals operating the system. The nightly data is binned into hourly intervals to accommodate the different starting times. In binning the hourly data, a few profiles at the beginning and end of a run may not be included as they do not constitute an hour's (40 minutes – minimum) worth of data. The same can be said for profiles that have had a large amount of data removed due to cloud cover. A single-hour temperature profile typically starts at ~ 85 km. Figure 12 shows several of the hourly temperature profiles from a single night in June with MSISe90 included as a reference. The measurement uncertainties for an hourly profile are typically 5 K at the upper altitudes and decrease rapidly toward 1 K at 60 km. The small fluctuations in the temperatures in the lower altitudes are real and are typical for the summer months when there is little geophysical activity.

Above 75 km, there is a sharp increase in the variability of the temperature profiles. This is a combination of the variability of the atmosphere, the low signal at the upper altitudes of the lidar, and what appears to be a region of high variability at the beginning of the integrations to calculate the temperatures.

2. Nightly Temperatures

In addition to the hourly temperature profiles, the nightly average is also calculated.

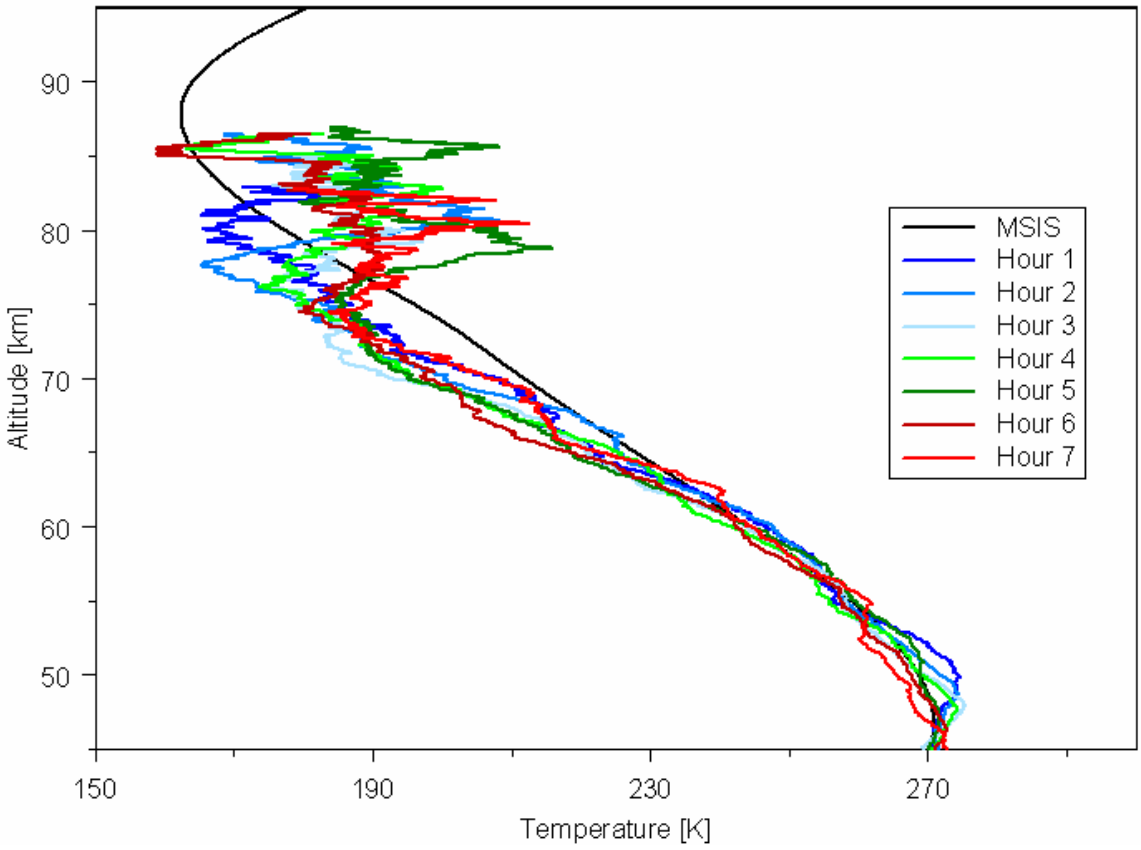

Figure 12. Hourly temperature profiles from June 12, 2003.

The nightly average can be calculated in two different manners. The first is to take the average of the hourly temperature profiles. The second method is to average the individual soundings of the atmosphere for the whole night together into a single relative-density profile. The second method will produce temperature measurements to higher altitudes due to the higher signal-to-standard deviation ratio from averaging many more raw signals. A comparison of the two methods typically shows a slight difference in the temperature structure at the upper altitudes. One reason for the difference is the two methods contain different amounts of data. In averaging the hourly temperature

profiles, the intervals that contain less than 40 minutes are not included in the average. By averaging together all of the good two-minute profiles, the second method typically will contain slightly more data and cover a slightly larger period of time. The greater signal-to-standard deviation ratio for the all-night data average causes the starting altitude to increase a few kilometers and the starting temperature to be different. By increasing the starting altitude, it is increasingly important to have a linear background to produce accurate temperatures.

Small adjustments to the background level can have a dramatic effect on the reduced temperatures. The curves in Figure 13 show the effects of changing the background level. The blue and red curves are the original temperature produced by the two averaging techniques. By changing the background level, it is possible to decrease the temperature difference between the two techniques. As mentioned in Chapter 5, the error in the background measurement is quite small, but changing the region from where the background is calculated can produce changes larger than the error. This is a result froma small slope or non-linearity in the background. The difference between the three profiles decreases with decreasing altitude, becoming small after 10 km. Without a secondary measurement of temperature we cannot say which is correct.

3. Monthly Averages

The short-term oscillations in temperature in the middle atmosphere can be eliminated from the results by averaging the data for longer periods of times. The two averaging techniques used for the monthly temperature follow those used to calculate the nightly temperature averages. The first is to average together all of the all night

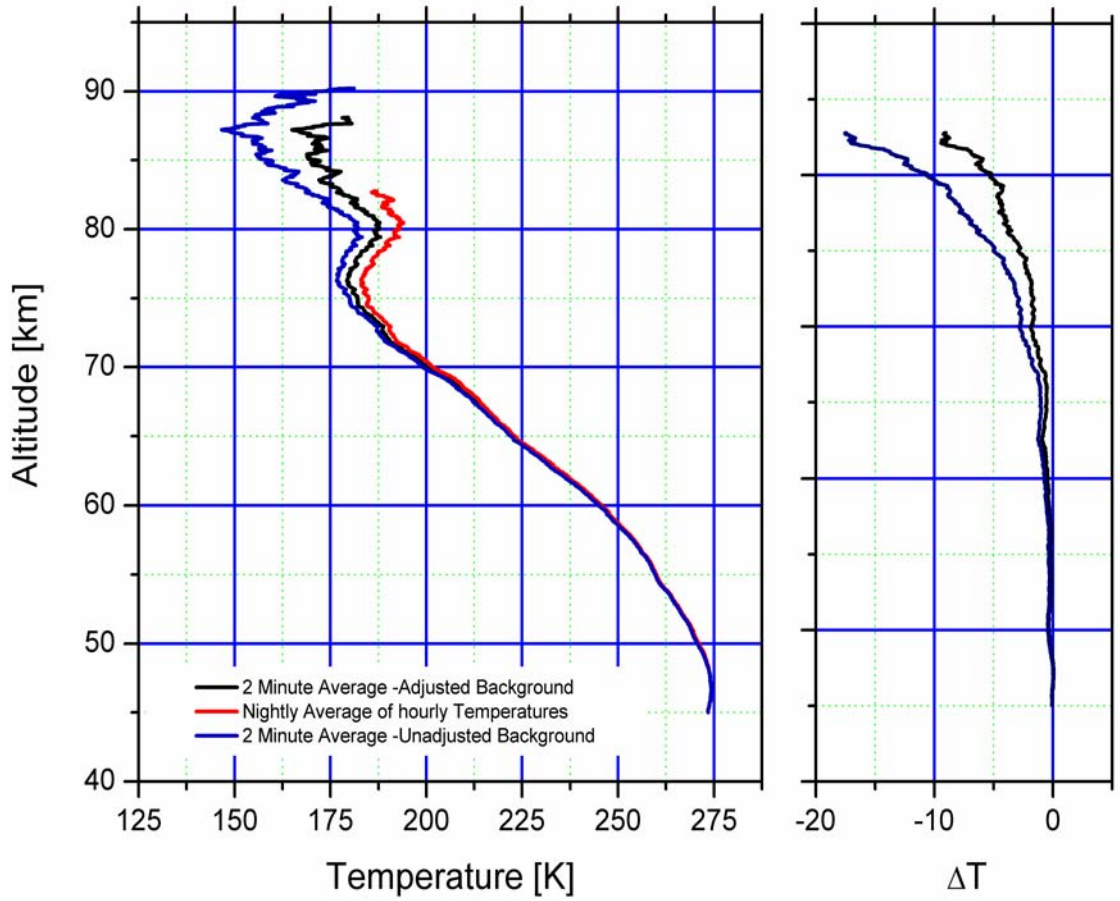

Figure 13. Comparison between the two nightly averages. The average of the hourly temperature profiles is in red. The black and blue curves represent the adjusted and unadjusted nightly averages of the raw two-minute data.

temperature profiles and the second is to average the two-minute profiles to generate a single profile from which to derive the temperature.

Typically the average of the nightly temperatures is completed first. For any given night, the number of two-minute profiles collected is mainly dependent upon the season of the year and the operator of the lidar. Certain nights will have temperature measurements that reach 90 km and others will barely reach 80 km. To take account of this when making the monthly temperature averages, the average was stopped at the

altitude where half of the profiles started below and half above. By this means there are still several profiles at the upper altitudes and the resulting temperatures are not dependent upon only one or two nights.

The second method for monthly averages is to average together all of the photocounts. This averaging scheme increases the signal-to-standard deviation ratio and, as a result, increases the maximum altitude to which temperatures may be calculated. With a change in the maximum altitude, the initial temperature will also change. The monthly averages are given for every month the lidar was in operation in Figures 14, 15, 16, and 17. The plots on the left-hand side are temperature profiles resulting from the average of the raw photocounts and the right-hand plots are the results from the average of the nightly temperature profiles.

A few of the temperature profiles need adjustments to the background level to bring them into agreement with the nightly averages, but overall the two techniques show very good agreement. This solves the problem that *Beissner* [1997] had found and emphasized the background level is extremely important. There are some differences at the highest altitudes due to the initial temperatures and the averaging techniques used.

In general the winter months show large amounts of inter-annual variability. The remaining months show some inter-annual variability, but this is relatively small compared to the winter months. There are several months where one or two years are significantly different from the rest. For instance, looking at the results from January two years, 1994 and 2001, show a very unusual temperature structure that is much hotter than the others. The results from July of 1998 also show a very different temperature structure

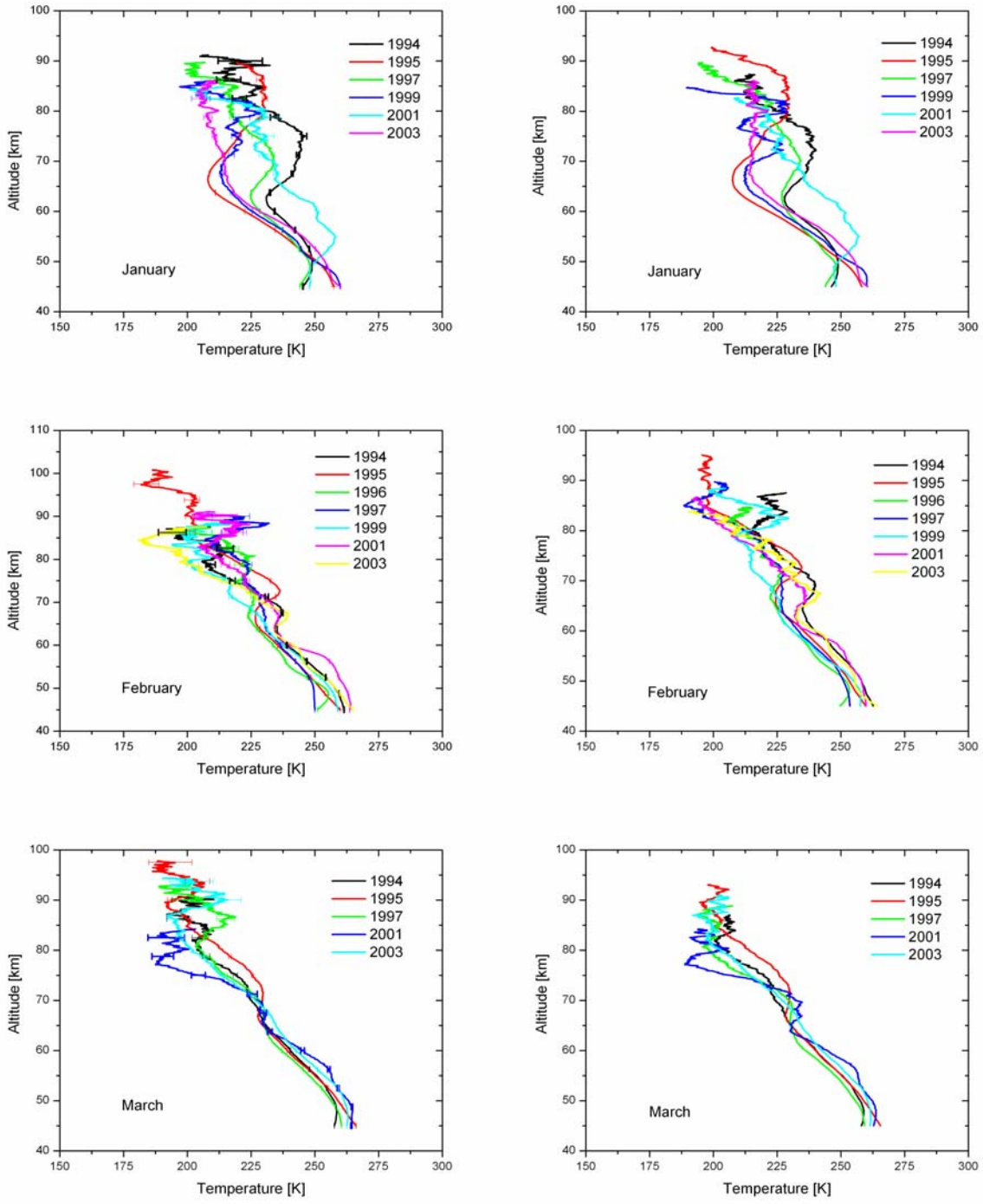

Figure 14. Monthly temperature averages for January, February, and March calculated by two different methods. The figures on the left are calculated from the average of the raw signal and the figures on the right are the results of averaging the nightly temperature profiles. The error bars on the left-hand side are the measurement uncertainties.

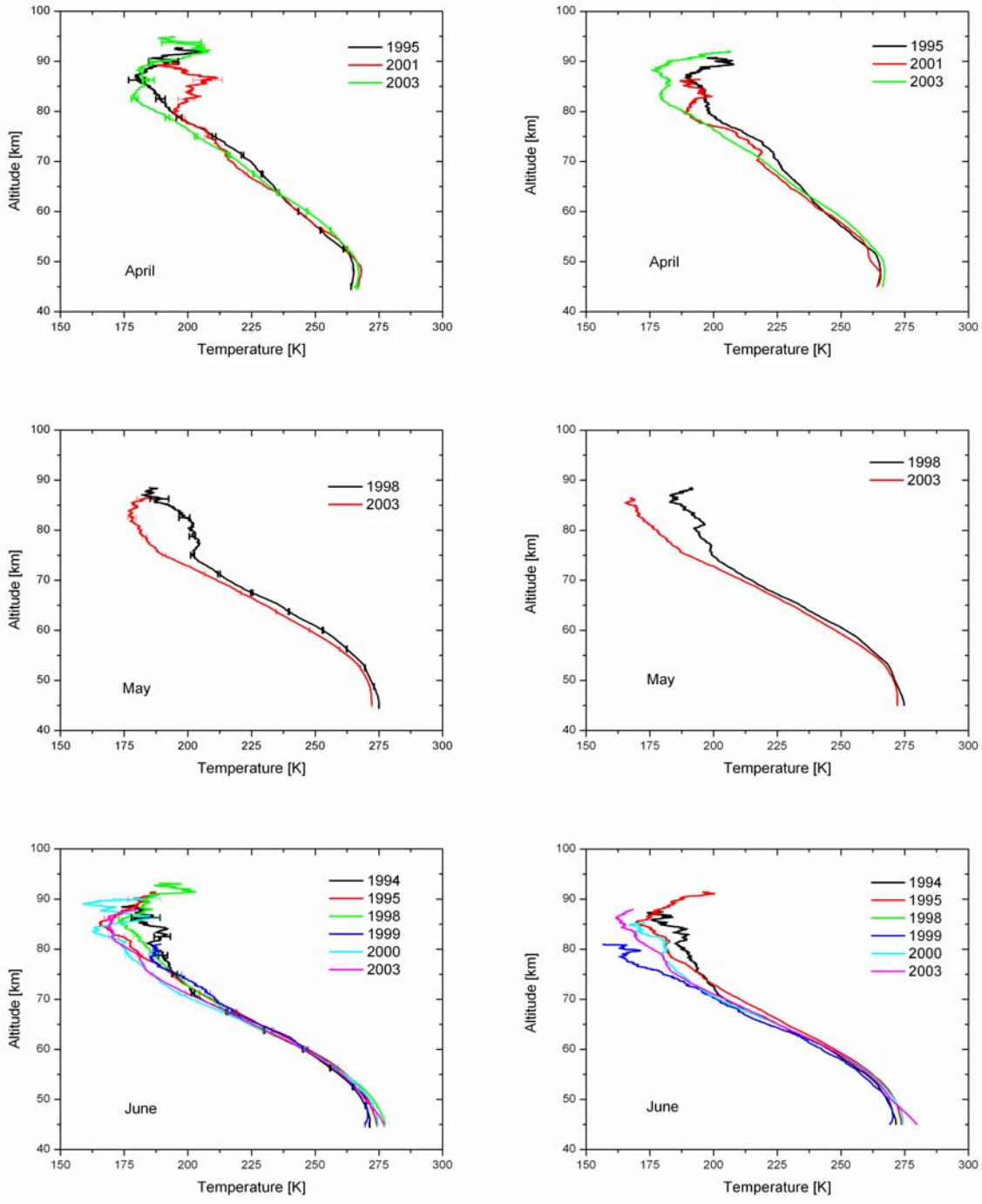

Figure 15. Monthly temperature averages for April, May, and June calculated by two different methods. The figures on the left are calculated from the average of the raw signal and the figures on the right are the results of averaging the nightly temperature profiles. The error bars on the left-hand side are the measurement uncertainties.

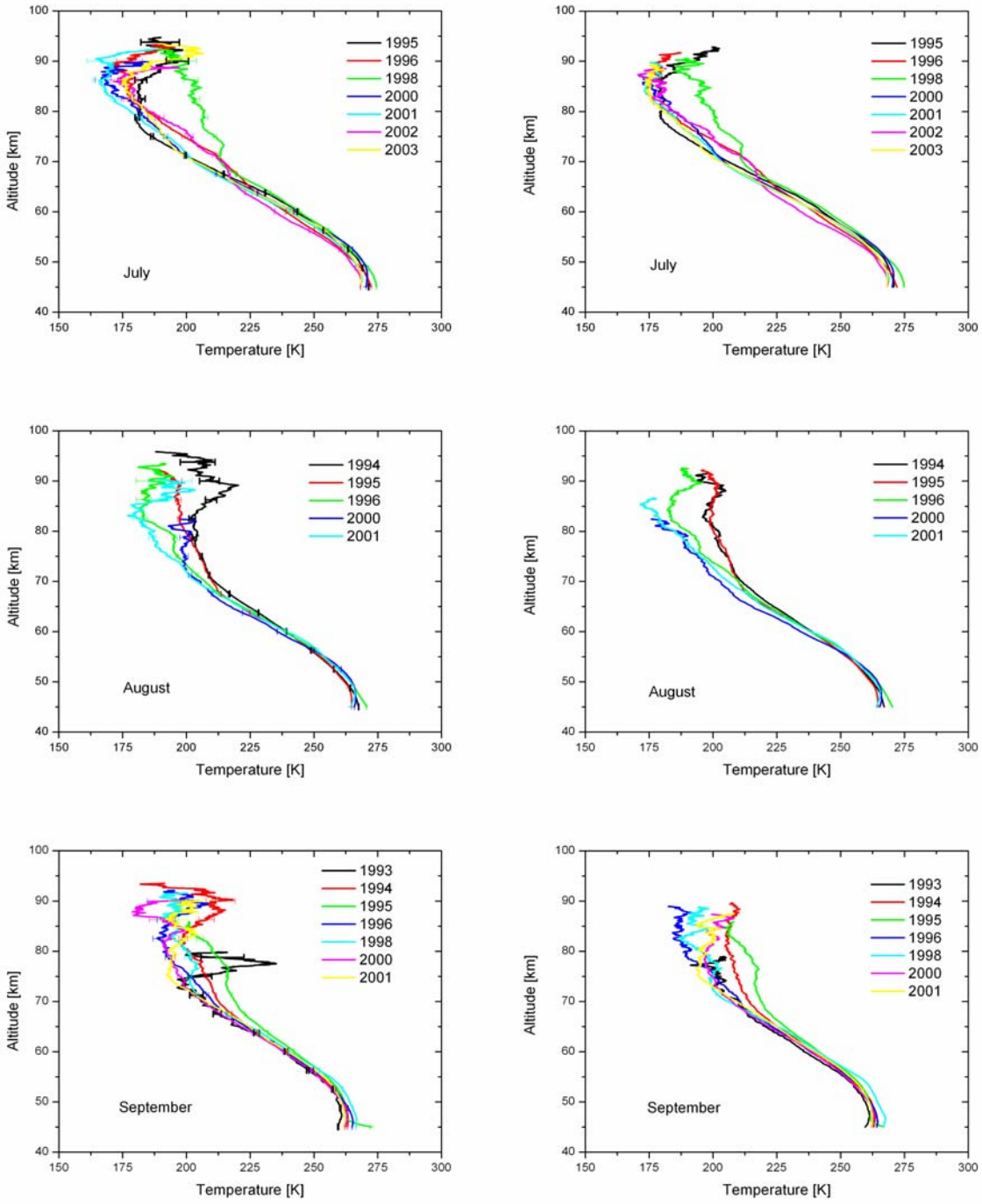

Figure 16. Monthly temperature averages for July, August, and September calculated by two different methods. The figures on the left are calculated from the average of the raw signal and the figures on the right are the results of averaging the nightly temperature profiles. The error bars on the left-hand side are the measurement uncertainties.

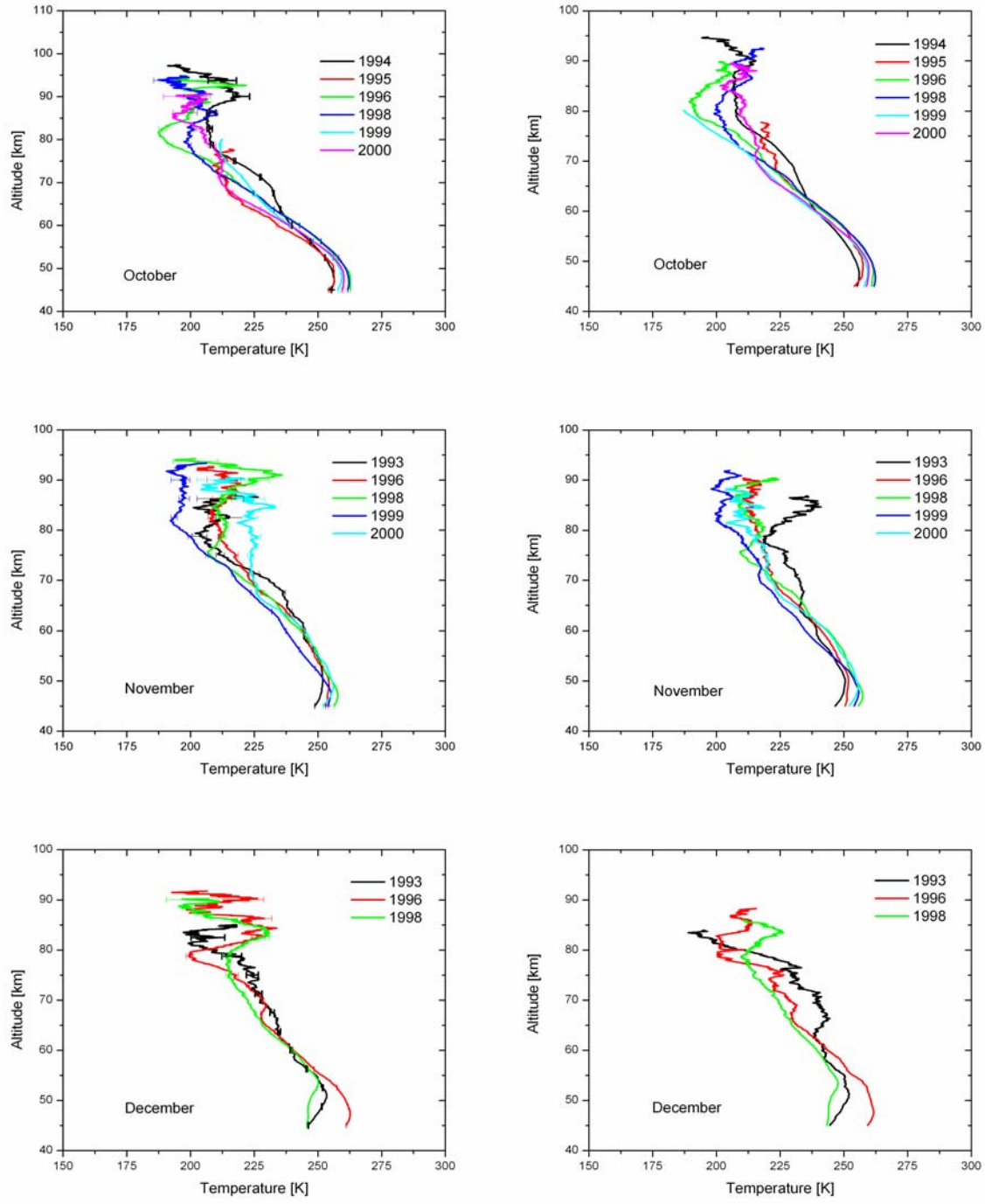

Figure 17. Monthly temperature averages for October, November, and December calculated by two different methods. The figures on the left are calculated from the average of the raw signal and the figures on the right are the results of averaging the nightly temperature profiles. The error bars on the left-hand side are the measurement uncertainties.

from the other years. A possible reaction to these different temperature profiles is to question their validity. The nightly temperature profiles were carefully checked for the types of problems that cause bad temperature. None were found. These unusual years will warrant a more in-depth analysis to try to determine physical reasons for the significant variations.

4. Multi-Year Monthly Temperatures

The next step is to average together all of the data from a given month spanning multiple years. Figure 18 shows the multi-year monthly average of the nightly temperature profiles. The starting altitudes of all of the months vary slightly from each other. The main reason is the maximum height is dependent upon the signal-to-standard deviation ratio of the nightly temperature profiles.

The temperature structure of the middle atmosphere undergoes a temperature inflection around 65 km. The temperature of the middle atmosphere also seems to have its smallest variability at this altitude. Near the mesopause region, the highest temperatures are from the winter months and the lowest temperatures are from the summer months. This is contrary to the more familiar temperature structure at lower altitudes where the winter months are colder and the summer months are warmer. The temperature structure of the upper mesosphere is not due directly to illumination from the sun, but the dynamics of the atmosphere. During the summer months we are able to see the temperature minimum that is the mesopause. The mesopause moves upward during the winter months making it difficult to determine the minimum temperature. Table 4 gives the results from the multi-year nightly temperature average.

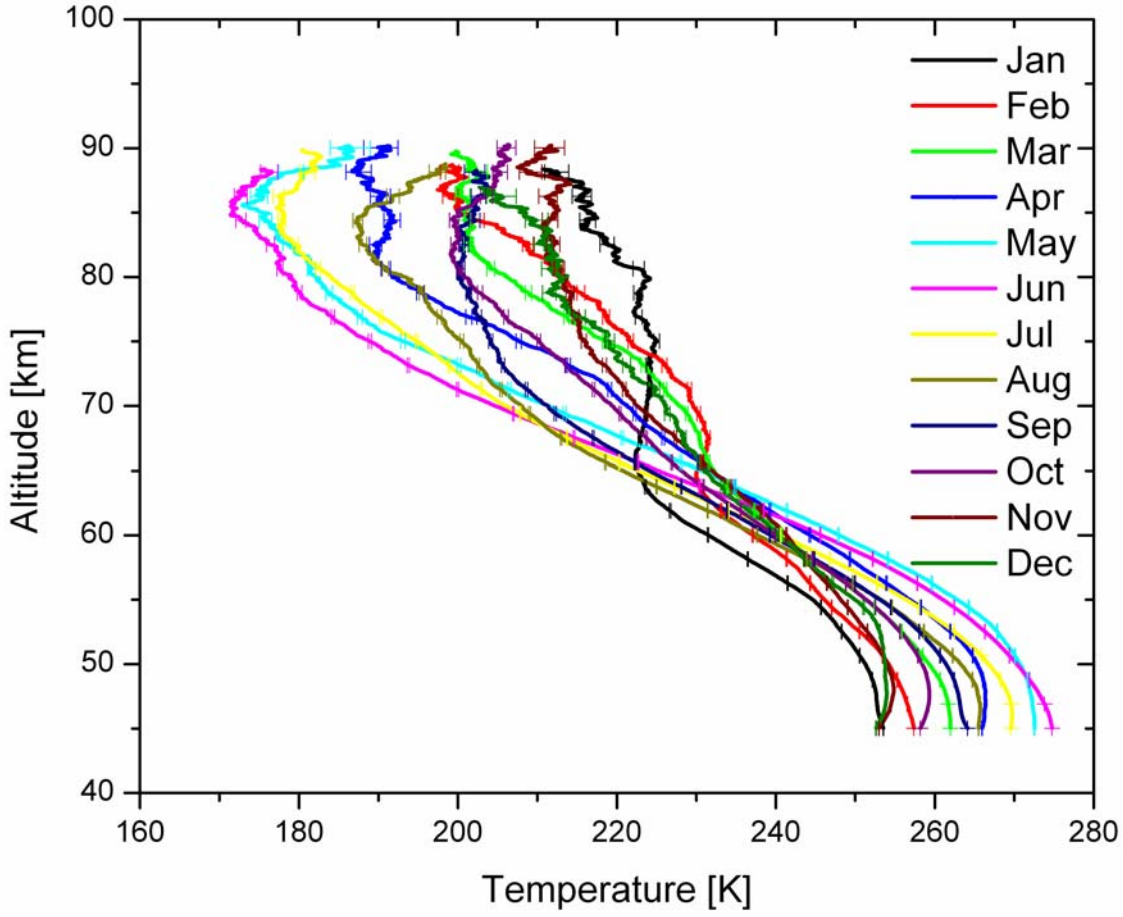

Figure 18. Monthly mean temperatures derived from the mean of nightly temperature profiles.

The number of nightly measurements that have been made during the 10 years of data are spread fairly evenly through the year. A month-long average can be calculated at an increased interval. A 28-day interval was used to calculate a month-long mean of the nightly temperature profiles starting on the first of the year, with the first half of the data coming from December and the second half coming from January. This 28-day interval was then shifted, moving the mid-point of the 28-day period by one week, and the mean calculated again. By this method smaller-scale features are visible in the contour plots due to the higher data density and not due to some artifact of a fitting routine in the

Table 4. Multi-Year Monthly Average of Nightly Temperatures

Alt	Jan	Feb	Mar	Apr	May	Jun	July	Aug	Sep	Oct	Nov	Dec
45	254	257	262	266	273	275	270	265	264	258	253	253
48	253	256	261	266	272	273	269	265	263	259	255	254
51	250	253	258	264	270	269	265	262	260	257	253	253
54	246	248	253	259	265	263	259	255	255	253	250	252
57	240	243	247	252	258	256	250	247	248	247	245	246
60	231	237	241	244	248	246	241	238	239	240	241	240
63	224	231	235	237	238	234	230	228	231	233	236	234
66	222	231	231	229	227	221	219	217	221	226	230	230
69	224	231	229	223	215	208	209	210	213	221	224	227
72	224	227	225	218	204	198	201	204	207	216	220	223
75	225	222	218	208	193	189	195	201	204	210	216	219
78	223	218	211	198	185	181	188	196	202	204	214	214
81	220	211	204	190	181	177	182	190	200	200	212	212
84	215	205	202	191	177	174	178	188	201	200	211	210
87	215	198	200	189	175	173	180	194	203	205	213	203

contour plot. This method produced 53 temperature profiles which produces a smoother contour profile with more information than using just the 12 monthly temperature profiles. Figure 19 shows a contour plot of the resulting temperatures calculated from the nightly averages. The maximum stratopause and minimum mesopause temperatures are very obvious when plotted in this manner.

The maximum and minimum temperatures appear during the same time of the year, between May and June. The stratopause region however has a slower temporal response than the mesopause that appears to have dramatic temperature changes over a short period of time. Taking for example the month of August, the stratopause area around 45 km changes only 5 K during the period but the mesopause region at 85 km changes 15 K.

The thermal behavior of the atmosphere during the winter months is strongly influenced by the atmospheric dynamics. This can easily be seen in the large inversion

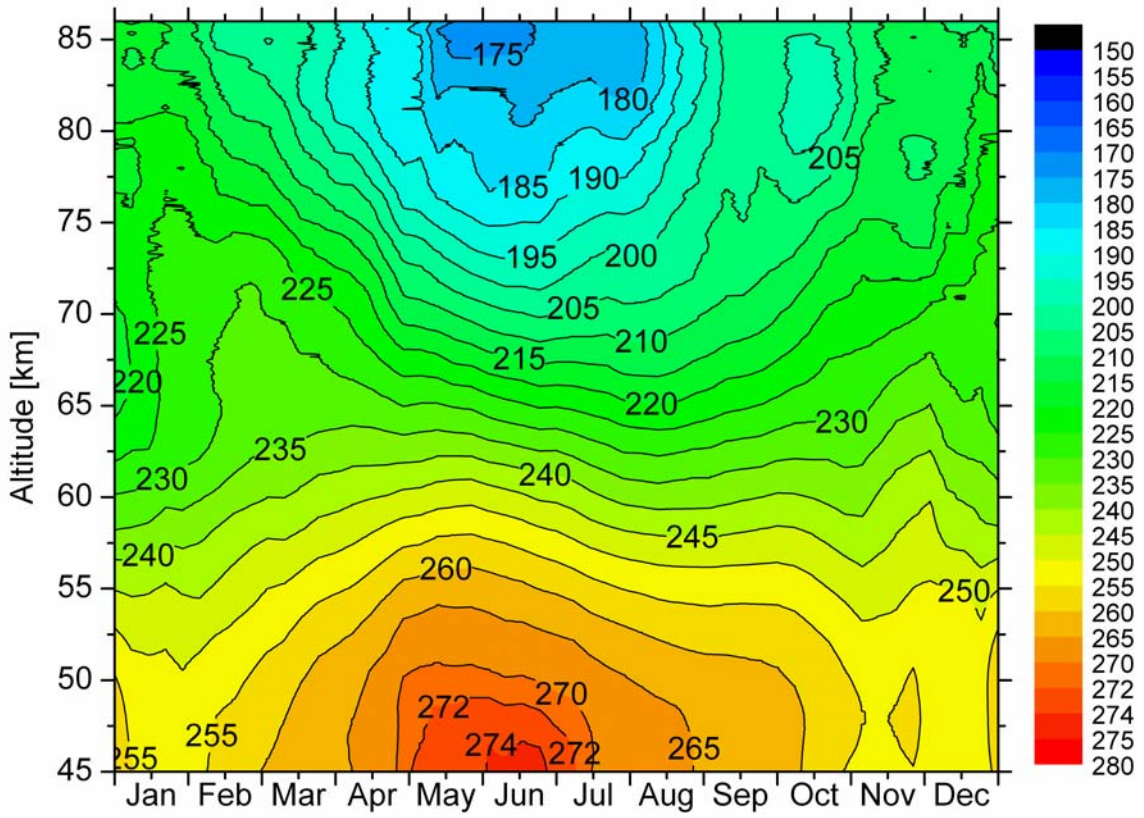

Figure 19. Multi-year temperature climatology produced from 53 28-day averages of nightly temperature profiles offset by seven days from each other. The contour levels are given at 5 degree intervals from 170 K to 280 K, and a 2 K interval near the summer stratopause.

layer present during the months of February and March. It is believed that such inversion layers are created by interactions of gravity waves with the background atmosphere,

including the diurnal tides and planetary waves [*Hauchecorne and Maillard*, 1992; *Meriwether et al.*, 1997; *Meriwether et al.*, 1998].

The monthly averages can also be made by averaging together all of the two-minute temperature profiles gathered during a particular month for all the years the lidar was in operation. The monthly average of the all-night temperature profiles contain the

same amount of data as making a monthly average of all of the good two-minute profiles. However, the starting altitude for the data reduction increases dramatically when all of the raw data is summed.

The temperatures shown in Figure 20 are plotted from the point where the temperature-reduction starts. Since the initial temperatures are taken from a climatology, there is a certain amount of uncertainty involved with them. Typically the first 5-10 km of the data reduction is discounted as they are heavily dependent upon the starting temperature. (However, when these climatological values are used for individual nights, the uncertainty is greater and a greater altitude range has to be discounted.) When compared to Figure 18 the resulting temperatures are similar to those from the nightly averages, but at the higher altitudes there are several differences. This is due to the starting height, initial temperature, the amount of data used, and the background level. The higher starting heights allow the influence from the starting temperature to diminish by the altitudes where the average of the monthly means start. This effect will be discussed in Chapter 5. The temperature values for Figure 20 are given in Table 5.

The difference between the temperatures produced by the two averaging techniques is highly dependent upon the background value. The differences between these two techniques are given in Table 6. As was shown previously the differences can be minimized by varying the background level. This was done by making incremental changes to the background to minimize the overall temperature difference. The difference between the two techniques is greater at higher altitude and decreases as the temperature-reduction continues. As the starting temperatures are unknown it is

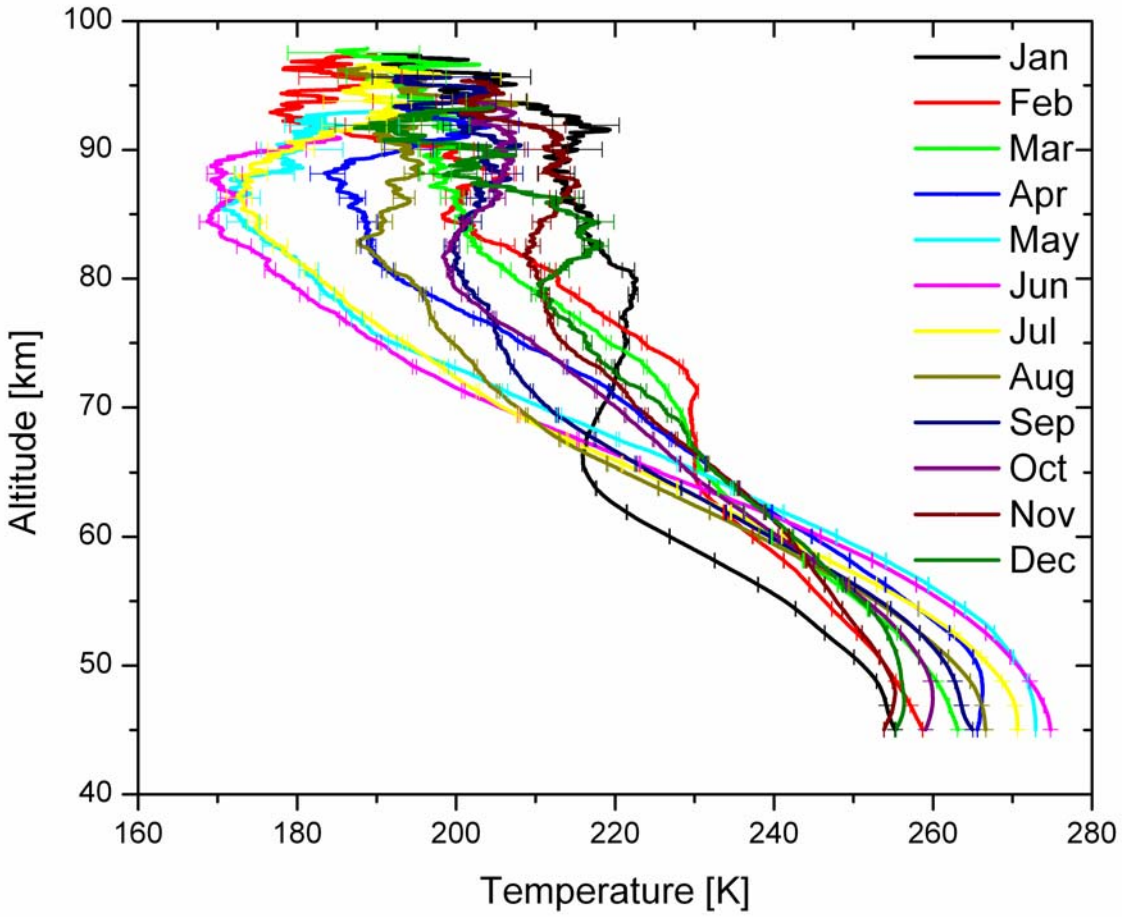

Figure 20. Multi-year monthly average calculated from two-minute profiles.

impossible to determine which profile is the correct one as each had points in its favor. These differences indicate the derived temperatures are good except at the highest altitudes, to within 1 K. On average the two techniques agree well, but show increased differences in both the lower and upper altitudes (Figure 21). As can be seen in Figure 21 the yearly mean from averaging all of the raw data produces a temperature that is ~ 2 K warmer than the average of the nightly temperature profiles. Below 70 km the sign of the difference changes and the temperature of the raw average is ~1 K cooler than the average of the nightly temperatures. The difference at the upper altitudes can be

Table 5. Multi-Year Monthly Average Temperatures Derived from Average of Raw Photocounts

Alt	Jan	Feb	Mar	Apr	May	Jun	Jul	Aug	Sep	Oct	Nov	Dec
45	255	259	263	266	273	275	271	267	265	259	254	255
48	254	256	261	266	272	273	260	265	263	260	255	256
51	249	253	258	265	270	269	266	261	261	258	253	255
54	243	248	253	259	265	264	259	255	255	254	249	253
57	236	243	246	252	257	256	251	247	248	248	245	247
60	227	237	240	245	248	246	241	238	239	241	242	242
63	219	232	234	237	237	234	231	228	231	234	237	236
66	216	230	230	231	226	221	220	218	222	227	231	231
69	218	230	229	224	215	209	209	210	214	222	225	228
72	220	230	226	218	204	199	201	204	208	216	220	221
75	221	224	219	208	192	190	194	200	205	210	214	217
78	222	217	213	199	185	183	186	196	204	203	211	212
81	220	210	206	190	181	176	181	191	200	199	209	214
84	216	202	201	189	174	170	175	191	201	201	211	216
87	214	201	199	186	172	171	174	193	203	205	214	207
90	215	200	198	194	181	178	179	193	206	206	211	203

Table 6. Temperature Difference Between Averaging Methods

Alt	Jan	Feb	Mar	Apr	May	Jun	Jul	Aug	Sep	Oct	Nov	Dec
45	-2	-1	0	0	0	-1	-2	-1	-1	-1	-2	0
48	0	0	0	0	0	0	0	0	-1	0	-2	0
51	0	0	-1	0	0	-1	1	-1	-1	0	-2	0
54	0	0	0	0	-1	0	0	0	-1	1	-1	0
57	0	1	0	1	0	-1	0	0	-1	0	-1	0
60	0	-	-1	0	0	0	0	0	-1	-1	-2	0
63	-1	1	0	1	0	-1	0	0	-1	-1	-2	0
66	1	1	-2	1	0	-1	-1	-1	-1	-1	-1	0
69	1	0	-1	0	-1	0	0	-1	-1	-1	-1	0
72	-3	-1	0	0	-1	0	0	-1	0	0	2	0
75	-2	-1	0	1	-1	1	1	-1	0	2	2	0
78	1	-2	-1	0	-2	2	0	-2	1	3	2	0
81	-1	-2	0	0	1	1	-1	0	1	3	-2	0
84	3	1	2	3	4	3	-3	0	-1	0	-6	0
87	-3	1	3	3	2	6	1	0	0	-1	-4	0

attributed to differences in the starting altitudes and temperatures. The difference at lower altitudes can be due to differences in the selected backgrounds of the two averages. To assure the quality of the data used in the temperature climatology the data set from the lidar was divided equally into two separate data sets. In essence they were divided so every other day went into the same divided data set. Given these two data sets, spanning the 10-year period, the mean monthly temperature was found using the two techniques discussed earlier and the results are given in Figures 22, 23, 24, and 25.

The results from the two data sets show very good agreement over the majority of the months. The winter months show the least agreement as can be expected due to the

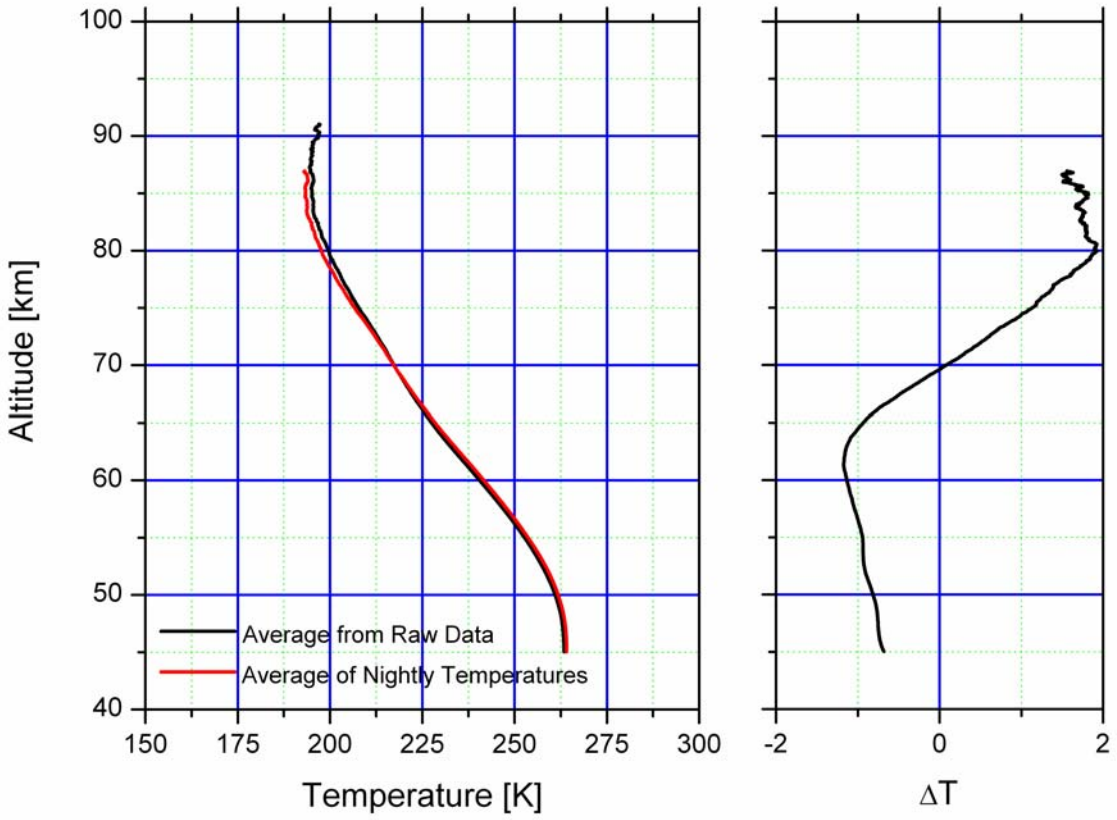

Figure 21. Yearly averages from the two averaging techniques with the temperature difference included.

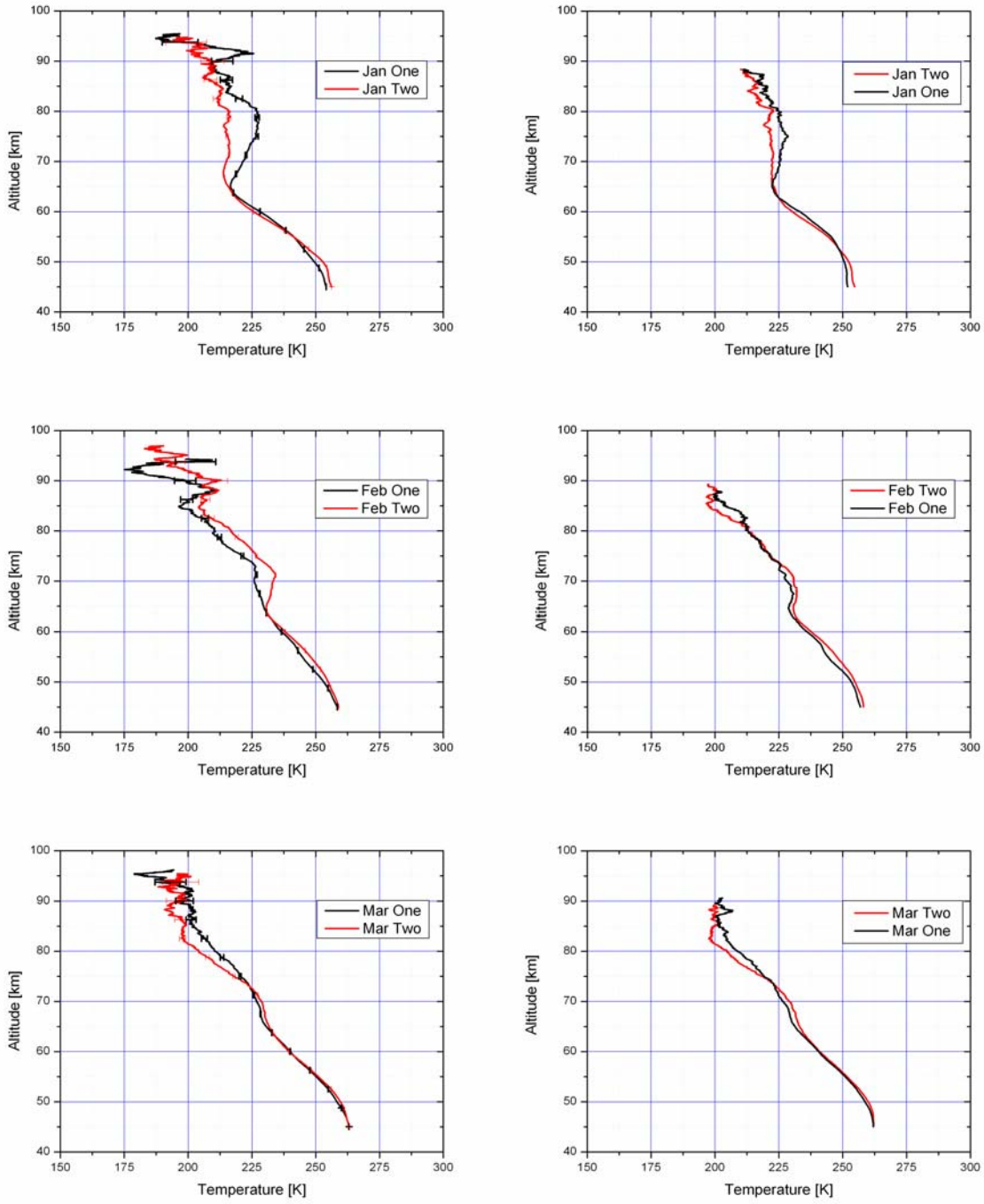

Figure 22. Results from two averaging methods on two equal halfs of the ALO data set for January, February, and March. The left-hand set is the two-minute data average with the associated temperature uncertainty and the right set is the average of the nightly temperature profiles.

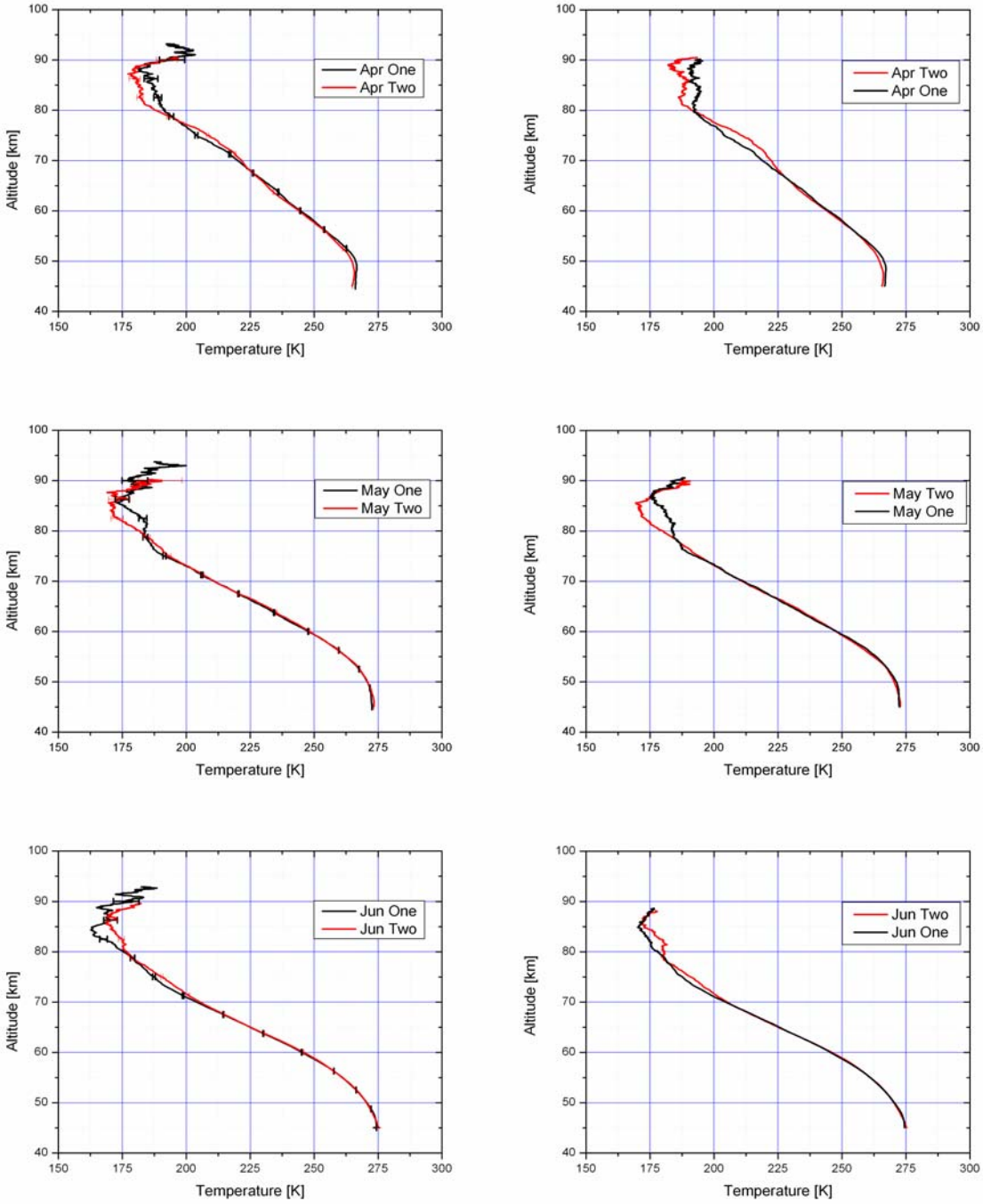

Figure 23. Results from two averaging methods on two equal halfs of the ALO data set for April, May, and June. The left-hand set is the two-minute data average with the associated temperature uncertainty and the right set is the average of the nightly temperature profiles.

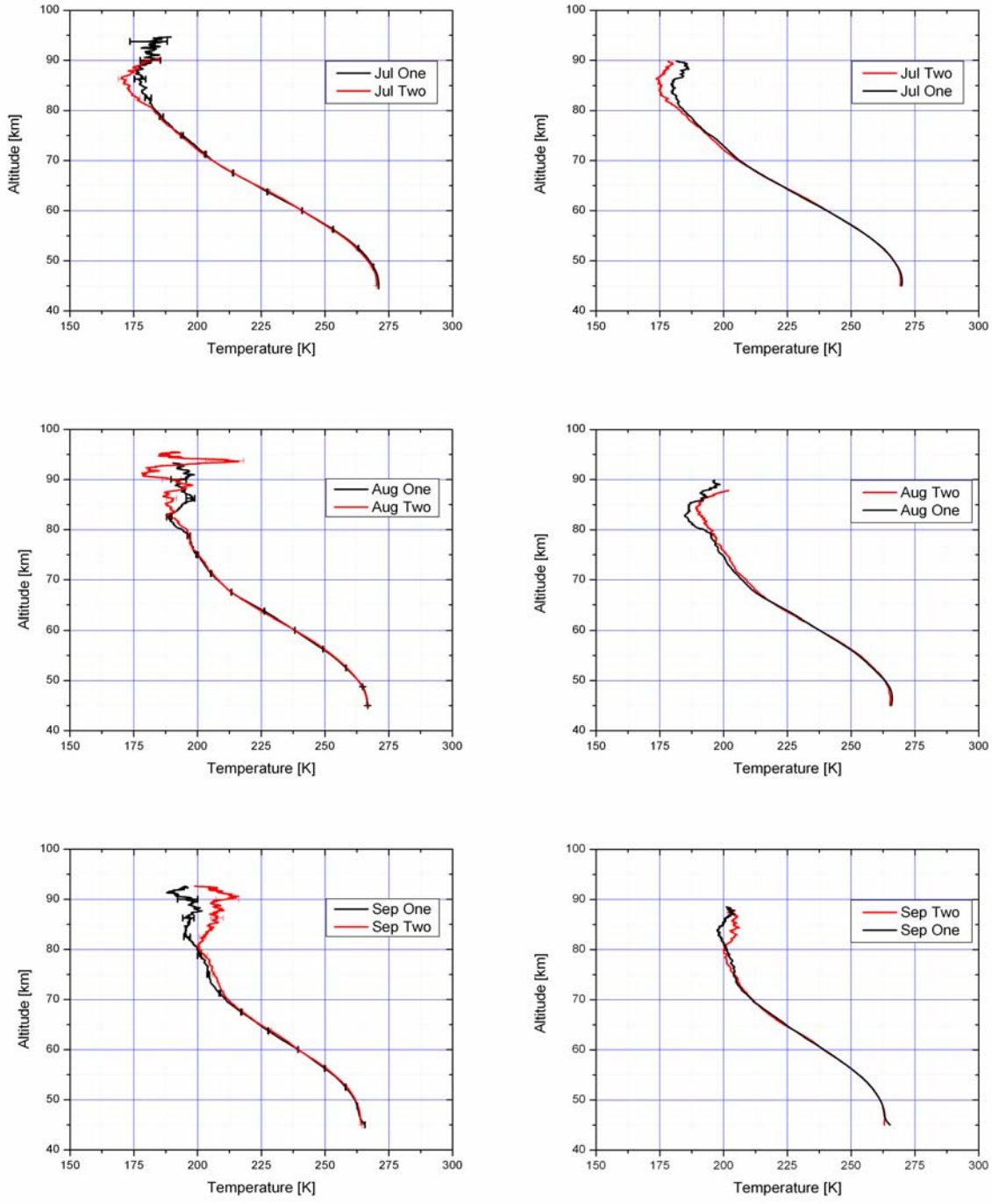

Figure 24. Results from two averaging methods on two equal halfs of the ALO data set for July, August, and September. The left-hand set is the two-minute data average with the associated temperature uncertainty and the right set is the average of the nightly temperature profiles.

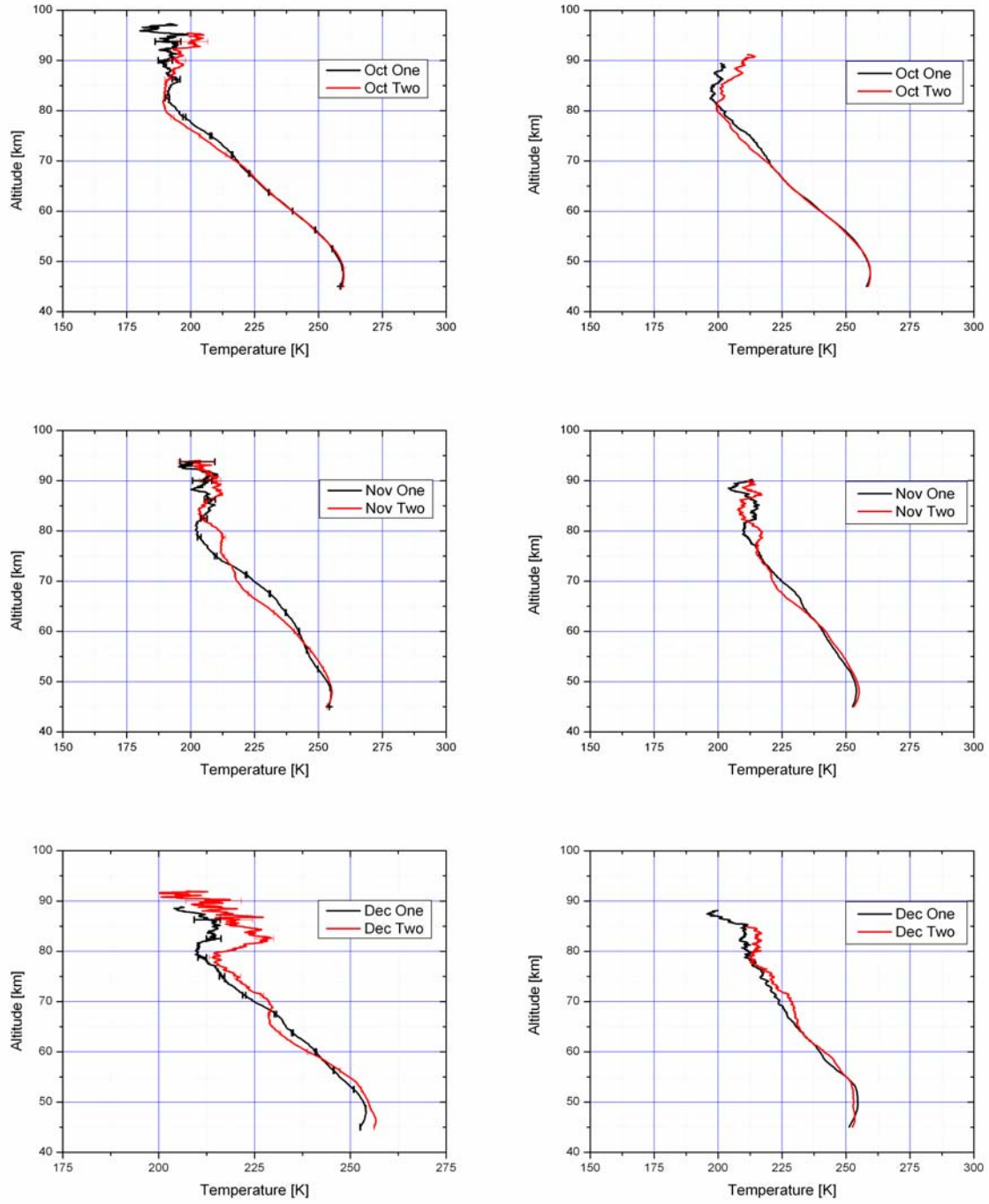

Figure 25. Results from two averaging methods on two equal halfs of the ALO data set for October, November, and December. The left-hand set is the two-minute data average with the associated temperature uncertainty and the right set is the average of the nightly temperature profiles.

increased geophysical variability during this season. The average of the nightly profiles, however, shows better agreement than the temperature profiles derived from the average of the raw photocounts. The difference between the two methods does not produce large changes in the deduced temperatures. The average of the raw photocounts gives a higher signal-to-noise level due to the amount of averaging. For example, a single night may contain only 300 profiles, while the multi-year profiles can contain more than 12,000 profiles, dramatically reducing the signal-to-noise ratio. An average with a systematic error in the background may produce incorrect temperature measurements, which are emphasized in averaging the photocounts. In some cases a small change to the background level was introduced. It brought the results from the average of the raw photocounts into agreement with those from the average of the nightly temperatures. These changes were bigger than the measurement uncertainty in the background as the variability in the background is greater than expected from Poisson statistics alone. However, shifting the background region to a higher or lower altitude will produce a larger change to the background than what was applied.

5. Geophysical Variation

The results from the lidar provide measurements of the temperature structure of the middle atmosphere. Beyond the basic temperature structure, it also provides information on the dynamics of the middle atmosphere. The geophysical variations of the middle atmosphere produce oscillations in the temperature structure seen with the lidar. The magnitude of these oscillations is found by calculating the RMS variation of the nightly calculated temperature profiles. A 28-day average of the nightly

temperature was calculated every seven days to give the RMS variation (Figure 26). The RMS variation was also calculated from the multi-year nightly temperatures for every month and is given in Table 7.

The RMS value is the measured uncertainty on any one nightly temperature profile because of geophysical variability (provided the measurement uncertainty is less). A better description of the geophysical variation calculated by this means would be the inter-annual geophysical variability. The use of the nightly temperature profiles averages out the shortest oscillations. The winter months show the highest level of geophysical variation over all altitude ranges, but at higher altitudes all of the temperature profiles

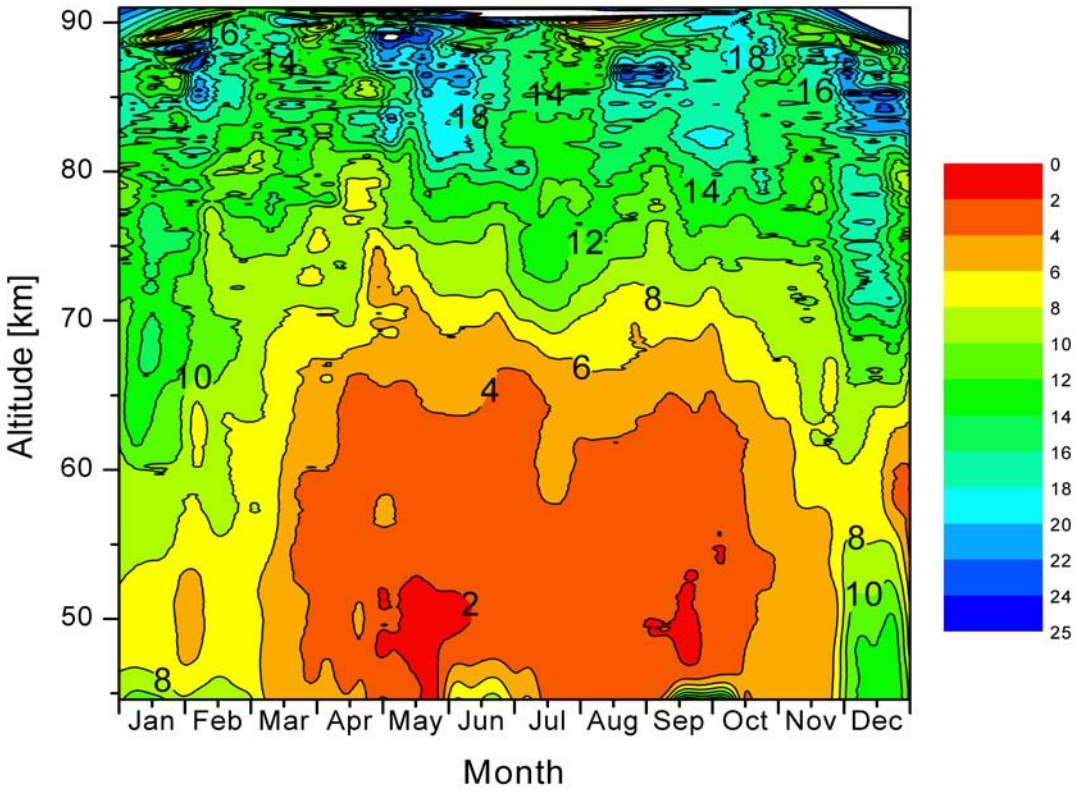

Figure 26. Geophysical temperature variations calculated from 28-day RMS values calculated every seven days from the nightly temperature profiles.

show large geophysical variation, which is to be expected when waves grow with altitude. The mesopause region is where the lapse rate of the middle atmosphere changes signs and this may cause an increase in wave breaking. As waves break in the mesopause region, there is transfer of energy, which can cause greater variability in the temperatures [*Hauchecorne et al.*, 1987].

6. Conclusion

The temperatures from the Rayleigh-scatter lidar were calculated on hourly, nightly, monthly, and multi-year monthly profiles. The monthly averages were derived in two different methods. The fist being an average of the nightly temperature profiles, and the second is an average of all the two-minute photocounts. The two methods have been shown to give good agreement and each has its advantages and disadvantages. To further show the accuracy of the temperature averages, the database was divided in two

Table 7. RMS Variability Calculated from the Nightly Temperature Profiles

Alt	Jan	Feb	Mar	Apr	May	Jun	Jul	Aug	Sep	Oct	Nov	Dec
45	9.8	9.1	5.3	4.6	2.2	7.7	3.3	3.0	9.9	4.4	5.3	12.9
48	7.6	7.7	5.2	3.3	2.0	4.4	2.9	2.4	2.5	4.1	5.3	12.6
51	6.9	6.7	5.3	3.6	1.8	2.1	2.7	2.4	2.0	3.8	4.4	10.4
54	8.3	7.4	4.8	2.6	2.3	2.2	3.0	2.2	2.2	3.6	5.0	9.0
57	8.8	8.3	5.3	3.0	3.0	2.5	3.7	2.7	2.4	4.1	5.7	6.8
60	10.2	7.6	5.7	3.4	2.8	2.7	4.4	3.0	3.1	4.5	7.4	6.4
63	12.0	7.3	6.7	3.3	2.4	3.0	4.1	4.3	3.5	5.0	7.9	7.4
66	13.6	9.5	7.4	3.9	3.9	4.0	4.5	5.5	4.4	7.2	8.6	10.0
69	14.6	10.7	7.8	7.1	5.0	4.6	6.8	5.7	5.9	9.0	9.0	12.4
72	13.8	10.4	7.6	9.1	5.0	6.5	10.2	7.7	8.5	10.9	9.4	16.6
75	15.4	9.4	10.3	9.0	7.6	8.7	11.4	11.0	10.6	12.5	12.4	16.5
78	13.6	11.4	14.1	7.7	10.4	11.8	10.6	13.9	12.0	16.4	12.3	16.6
81	14.2	13.1	13.0	10.4	12.2	15.4	12.0	14.7	14.5	18.9	11.9	15.2
84	15.7	15.3	14.1	16.9	16.8	14.9	13.4	17.2	16.6	17.2	14.4	22.7
87	14.5	12.8	12.3	13.7	18.9	17.6	14.3	24.7	15.0	17.8	16.5	13.0

and the multi-year monthly temperature calculated for each. Again, the two techniques

showed good agreement. The geophysical variability was also calculated from the nightly temperature profiles.

The temperatures deduced from the average of the two-minute photocounts reaches to higher altitudes than the average of the nightly temperature profiles. For use in making comparisons, it is useful to have the additional range. I will use the climatology generated by the average of all the two-minute profiles for most of the following comparisons. It is the major product of this work. The results are given in Figure 20 and Table 5.

CHAPTER 7

TEMPERATURE COMPARISONS

The major benefit of a Rayleigh-scatter lidar is the ability to make measurements of the middle atmosphere frequently and over a considerable altitude range. Most Rayleigh-scatter lidars have been built at a single location. The ALO lidar for example has been operating from the same location for 10 years. A few other Rayleigh-scatter lidars have been in operation for the same, if not longer, periods. The results from these systems when compared to those from the ALO lidar may show latitudinal and longitudinal differences. To gain a better understanding of the structure and physics of the middle atmosphere, it is helpful to compare the results with other instruments, both ground based and satellite based, in addition to examining the ALO data.

Typically instruments are separated by time, space, and differences in the types of measurements they make. In comparing the results from various instruments to those from the ALO Rayleigh-scatter lidar, we are looking for both similarities and differences. Data sets that are separated from each other in time may give some indication of trends, while those separated by distance may show longitudinal or latitudinal differences.

1. Comparisons with PCL

In Chapter 4 we showed the data reduction techniques used by the PCL and the ALO lidar produced identical results. Accordingly, meaningful comparisons can be made between the temperatures obtained at both sites. Figure 27 shows the temperature climatology derived from their measurements of the middle atmosphere from western

Ontario. PCL has been in operation since August of 1992.

The two lidar systems are located at approximately the same latitude, 41.7º N vs. 42.5º N. The climatology was created by moving a 33-day window through the nightly temperature averages in one-day increments [*Argall*, 2003], thus the smoothing is similar to that for ALO.

In a general view the stratopause region measured by the two lidars shows considerable agreement. This is not surprising as this region of the atmosphere is driven by radiative processes and the two lidar systems are located at approximately the same latitude. However there are some differences.

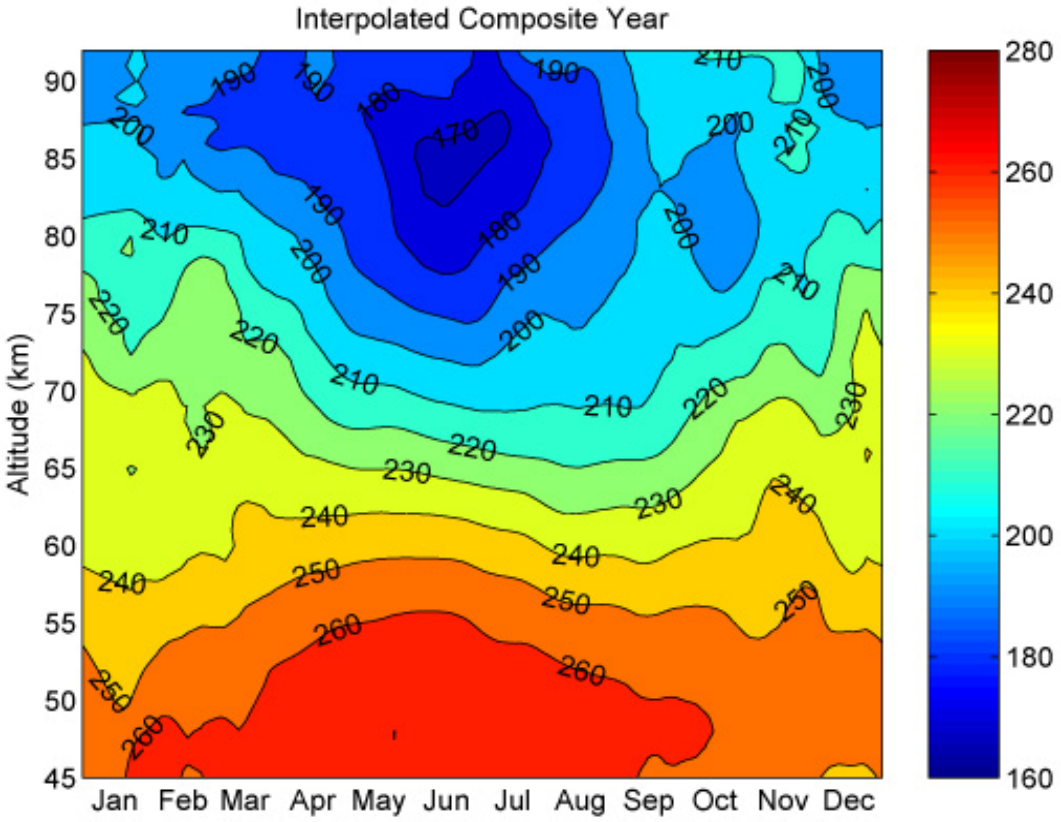

Figure 27. Temperature contour plot from Purple Crow Lidar [Courtesy of R.J. Sica and P.S. Argall].

To examine the stratopause, start first with the large contour level for the PCL at 260 K. Comparing this region to the 260 K contour for ALO from Figure 19 shows the PCL contour starting 1.5 months before ALO with both contours ending in October. May shows a small sliver of the 270 K contour, but the same contour level from the ALO lidar spans May and June and extends from 45 to 50 km. From this it is clear the stratopause above the PCL becomes warmer sooner, while the measurements from the ALO lidar show a higher maximum temperature by ~ 5 K.

The mesopause is slightly cooler at the PCL in the first half of the year than the second. There is a clear minimum to the mesopause temperature between June and July. The minimum temperature for the year is located at 85 km with a minimum temperature of 170 K. The ALO lidar in comparison has the minimum temperature also at 85 km but with a minimum temperature of 175 K. The striking difference between the two systems is the difference in where the minimums are found and not the 5 K difference in their temperatures. In the case of the PCL lidar the minimum temperature is found from the first week in June to mid July while in the case of the ALO lidar the minimum occurs earlier from mid May to mid June.

The PCL lidar with its larger collecting area has the advantage of starting their temperature-reduction at a much higher altitude so by 85 km, their uncertainty from the initial temperature is greatly diminished. Because the mesopause temperatures come from close to the initial altitude for the ALO lidar, there is no guarantee that an influence from the starting points is not present. A better comparison would be to redo the ALO reduction using the two-minute photocount profiles for the average which would increase the initial altitude.

One interesting aspect of what the two lidar systems observe is the inversion layer that can be seen during the month of February. The magnitude of the feature is at a higher temperature in the ALO contours. As both lidars are located at approximately the same latitude, this may be a result of the longitudinal difference. The PCL lidar is located in western Ontario in the Great Lakes region while the ALO lidar is located in the midst of the Rocky Mountains. These inversion layers are thought to be influenced by gravity waves, and the proximity of the ALO lidar to an orthographic source such as the Rockies may be the cause.

Overall the results from the two lidars show good agreement and significant differences. The intent is to continue the comparison. The purpose will be to look for longitudinal differences between the two locations by exploring these comparisons of stratopause and mesopause temperatures, and RMS values, simultaneous and non-simultaneous data.

2. Comparison with WINDII

WINDII is the WIND Imaging Interferometer onboard the UARS spacecraft. The instrument provides measurements of wind, temperature, and emission rate from the visible region airglow. Mesospheric temperature measurements are derived from Rayleigh-scattered sunlight observed in a wavelength band centered at 553 nm. Integrated line-of-sight limb radiance observations are inverted to tangent height volume-scattering profiles, which are proportional to atmospheric density [*Shepherd et al.*, 2001]. Temperatures are derived in the same way that ALO derives temperature.

The data from the WINDII instrument comes from three daytime measurements per orbit in the 10º latitude window with multiple orbits per day used for the ALO WINDII comparison. In contrast to these daytime observations, the lidar observations are nighttime only. Hence, a temperature comparison may include local time effects such as tides. In addition, there are differences in the observing periods. The WINDII data covers a period from March 1992 until January 1994 (Table 8). It was able to make 116 good daytime temperature profiles in this period between 35º and 45º N latitude. The lidar, Table 3, produced 427 good nighttime temperature profiles over a much longer and later period, from 1993 till 2003.

The monthly means from ALO and WINDII are given in Figures 28 and 29. They include the temperature along with the standard deviation of the mean. The two winter months, December and January, show considerable differences between WINDII and ALO. January shows the temperature results from the WINDII instrument to be much cooler than those from the lidar system. Noting the interannual variability seen at ALO, this difference may arise from the limited WINDII sampling. It might also arise because

Table 8. WINDII Data Used in Temperature Comparison

Period	Latitude Bin	Number of Days	Time of Coverage, LT
Jan 1993/1994	35º - 45º N	17	0700-1700
March 1992/1993	35º - 45º N	22	0600-1800
April 1992/1993	35º - 45º N	9	1000-1200, 1700-1900
July 1992/1993	35º - 45º N	18	0500-0900, 1500-1800
Aug. 1992	35º - 45º N	12	0500-0700
Sept. 1992	35º - 45º N	8	0700-1100
Oct. 1992	35º - 45º N	12	0600-1100
Dec. 1992/1993	35º - 45º N	18	0800-1600
Total Days of Observation		116	

of longitudinal differences. The two equinox periods, March/April and September/October, show good agreement with the results from March showing the best overall agreement. The summer months, July and August, when we expect a minimum in the geophysical variability, show interesting results. The results from July show the ALO temperatures to be systematically cooler than those from the WINDII instrument. The results from August show a minimum in the WINDII temperatures at 87 km and warmer temperatures between 70 and 75 km. The WINDII results for August were taken from 12 days from 0500 to 0700 for a single year. This may account for the differences between WINDII and ALO temperatures. Averaging together the eight monthly profiles from the WINDII instrument and the corresponding months from the Rayleigh-scatter lidar shows the two give very similar results (Figure 30). Along with the average temperature the RMS variation for the mean is given. The curves are close enough together to give the

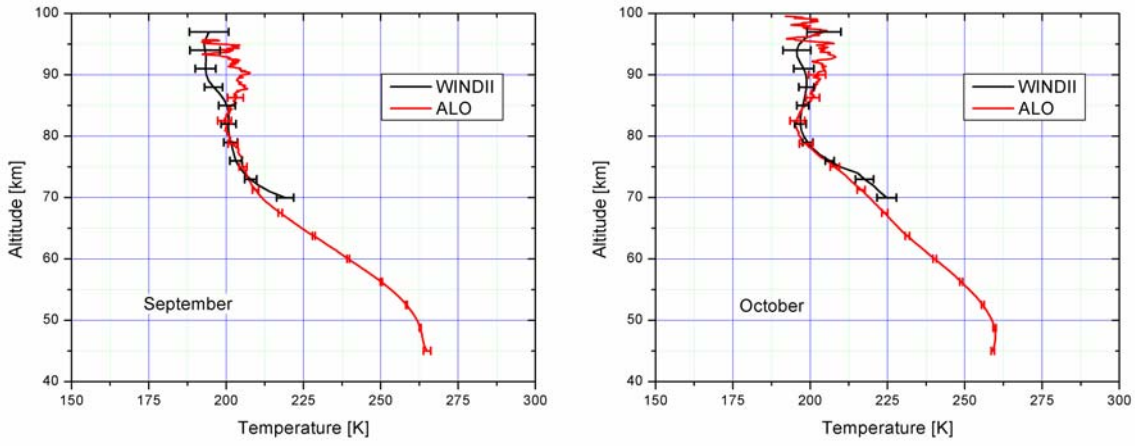

Figure 28. Temperature comparisons between Rayleigh temperatures from WINDII (black) and ALO (red) for September and October. The ALO temperature profiles are derived from the average of the two-minute data. The error bars are the RMS variation of the mean calculated from the nightly temperature profiles.

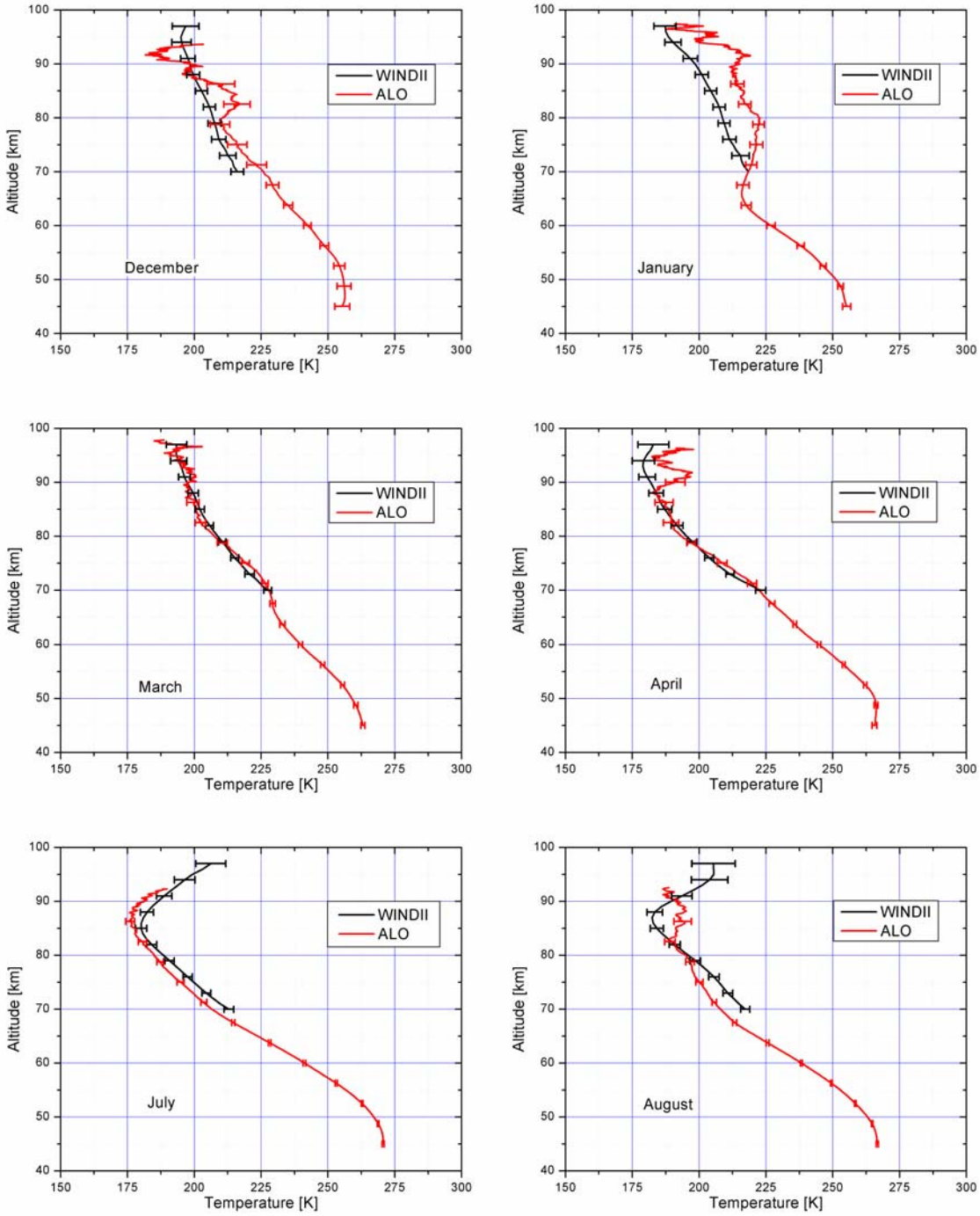

Figure 29. Temperature comparisons between Rayleigh temperatures from WINDII (black) and ALO (red) for December, January, March, April, July, and August. The ALO temperature profiles are derived from the average of the two-minute data. The error bars are the RMS variation of the mean calculated from the nightly temperature profiles.

impression the two systems agree very well. The two systems show some differences at the upper and lower altitudes, but the differences are encompassed within by the RMS variation of the mean and show good overall agreement.

3. **Comparison with SABER**

Sounding of the Atmosphere using Broadband Emission Radiometry (SABER) is one of the four instruments on the Thermosphere Ionosphere Mesosphere Energetics

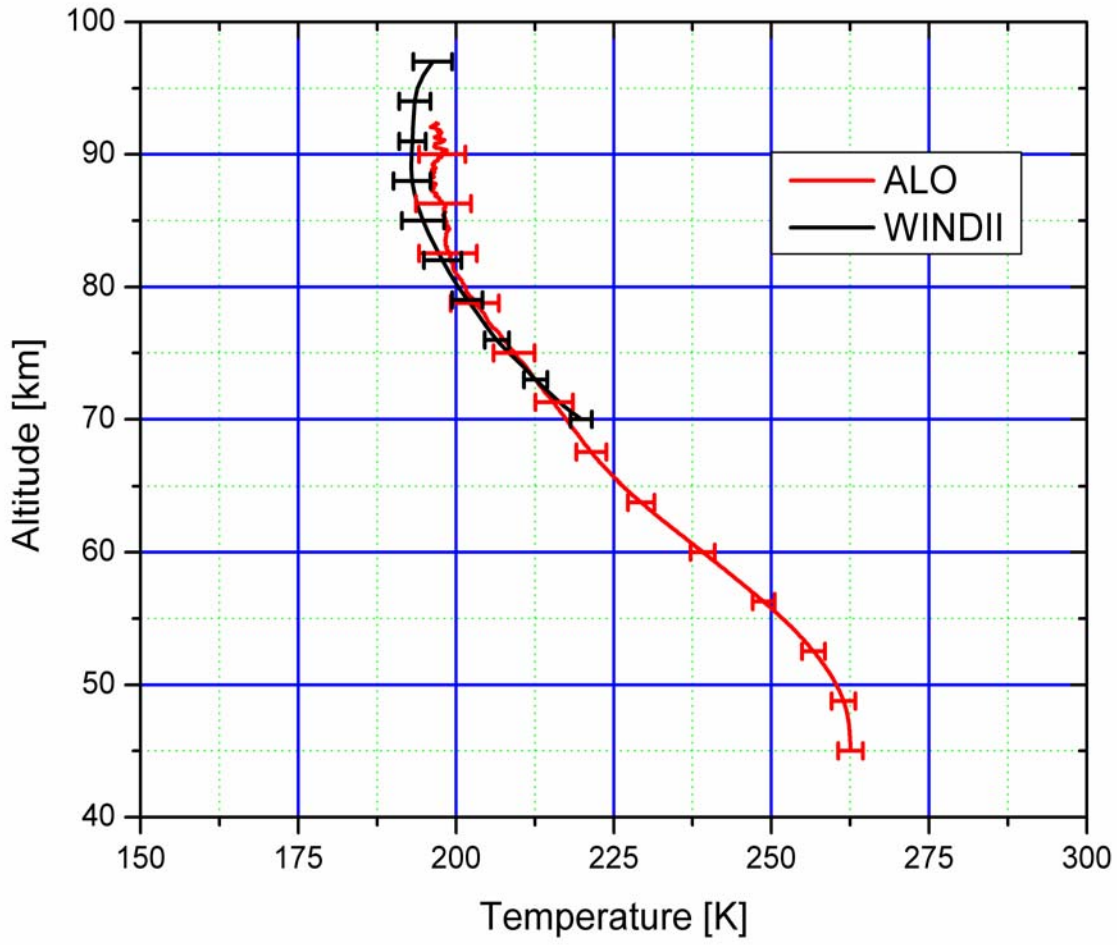

Figure 30. Average of the WINDII data (black) and the ALO data (red). The error bars and are the standard deviation of the mean for the two averages.

Dynamics (TIMED) satellite. The SABER instrument looks at Earth-limb emissions with a 10-channel radiometer. The data from the instrument must be mathematically inverted to provide vertical profiles. The primary data product from the SABER instrument is temperature derived from CO_2 from 10 to 130 km.

Since shortly after the launch of the TIMED satellite, SABER has been obtaining data for determining temperature profiles of the Earth's atmosphere. To compare temperatures derived from the SABER instrument to the ALO Rayleigh lidar, it was necessary to find spatial and temporal coincidences. A list of times was generated for which measurements from the SABER instrument were within 300 km of Logan during the period from 8 PM to 6 AM approximately when the lidar was in operation. Eighteen nights of coincident measurements were found between February 2002 and November 2002. The comparisons are shown in Figures 31 through 33.

While comparing the temperatures, it is also important to note the temporal and spatial differences between the two measurements. They are indicated on each plot. The time separation is between the mean time of the nightly temperature profile for the Rayleigh-scatter profile and the three-minute observation made by SABER. The spatial separations are given in latitude and longitude for the separation between the mid-point of the Saber measurement and the location of the lidar. The associated error bar for the ALO temperature profiles is the temperature uncertainty.

The temperature measurements from SABER show very good agreement with the measurements from the Rayleigh lidar. The agreement in temperature is directly related

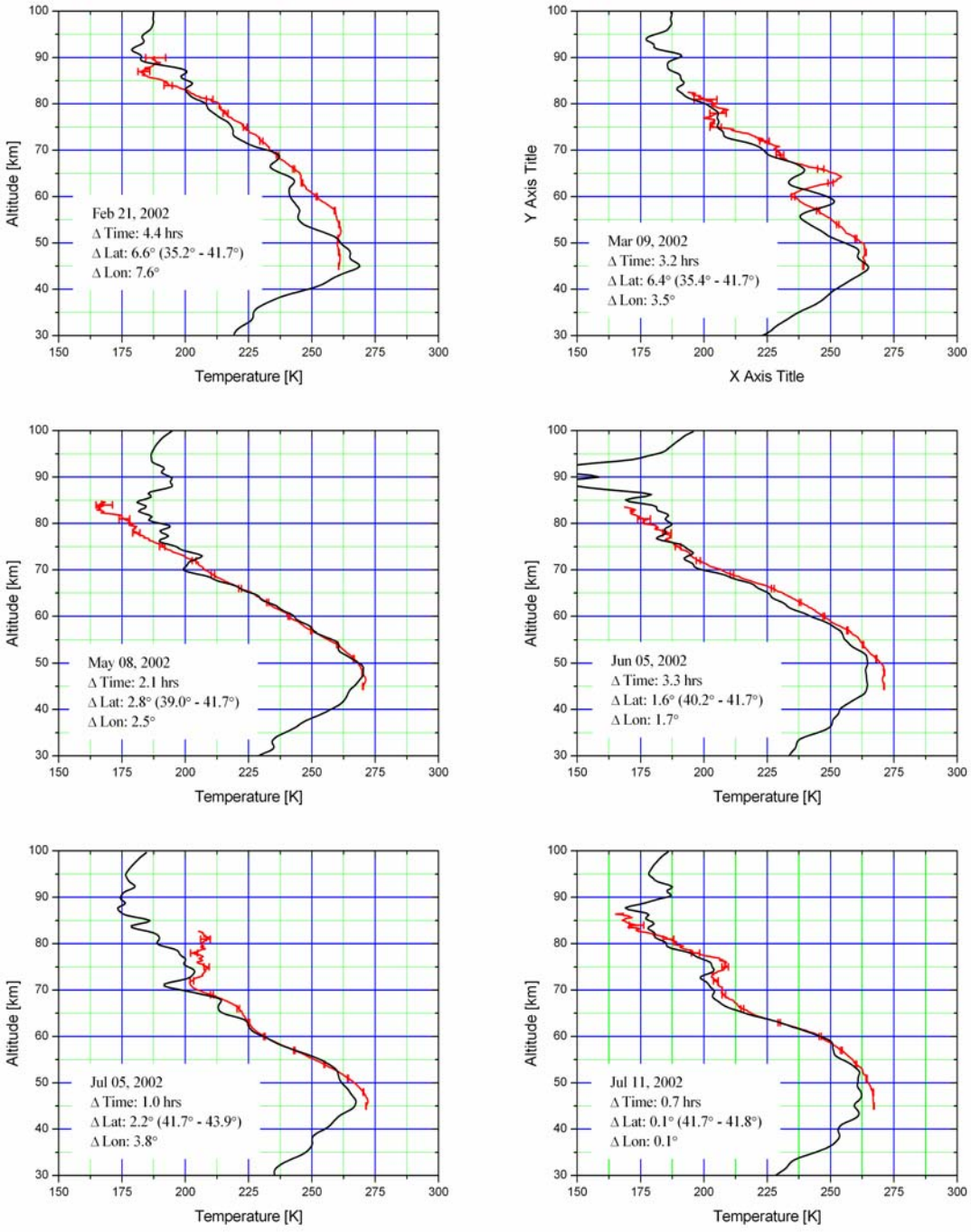

Figure 31. Nightly temperature comparison between SABER (black) and ALO(red). The SABER temperatures assume local thermodynamic equilibrium. The ALO temperatures are from averaging the two-min. photocount profiles for the night. The ALO uncertainties are from the measurement uncertainty, Eq. 3.3.26.

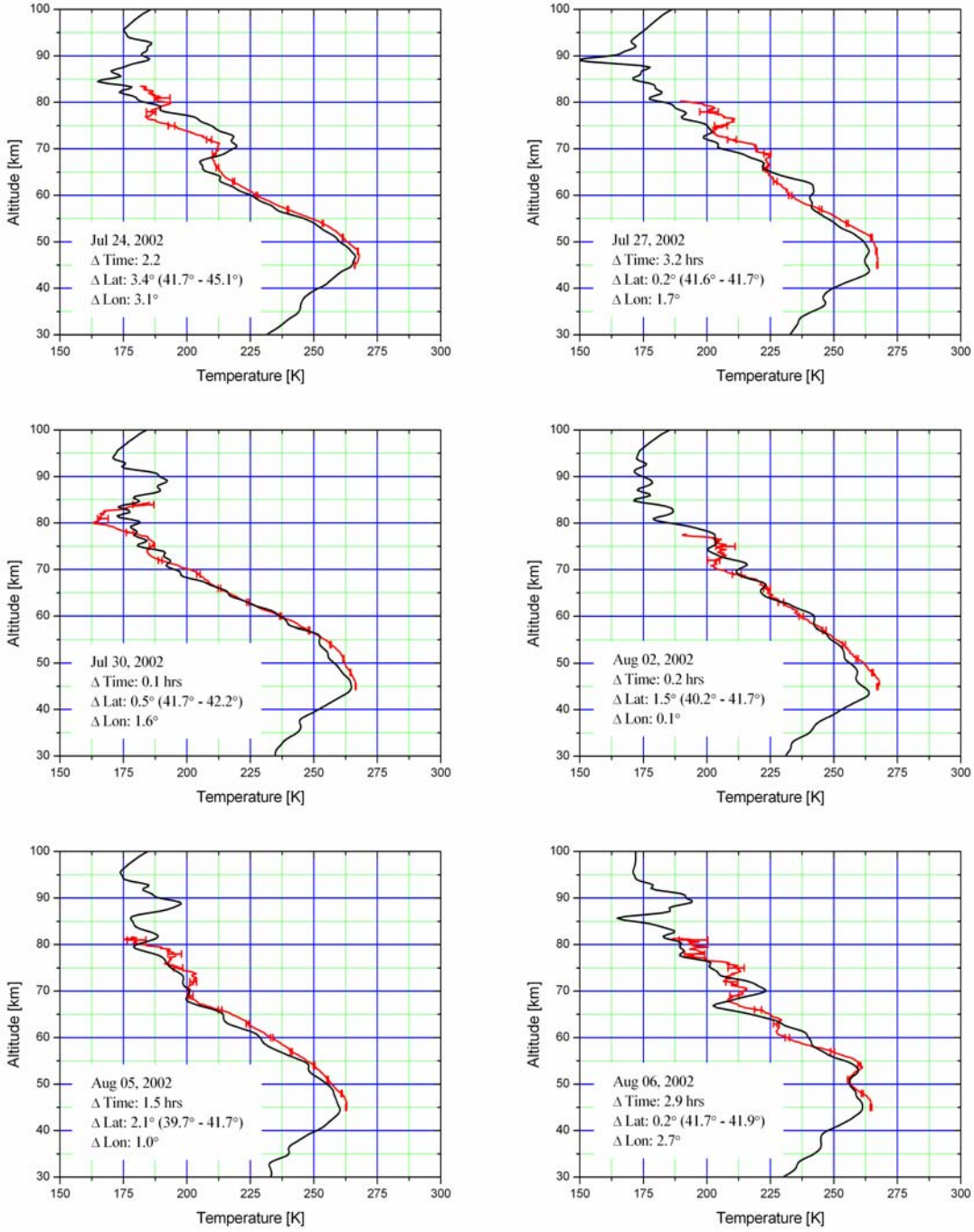

Figure 32. Nightly temperature comparison between SABER (black) and ALO(red). The SABER temperatures assume local thermodynamic equilibrium. The ALO temperatures are from averaging the two-min. photocount profiles for the night. The ALO uncertainties are from the measurement uncertainty, Eq. 3.3.26.

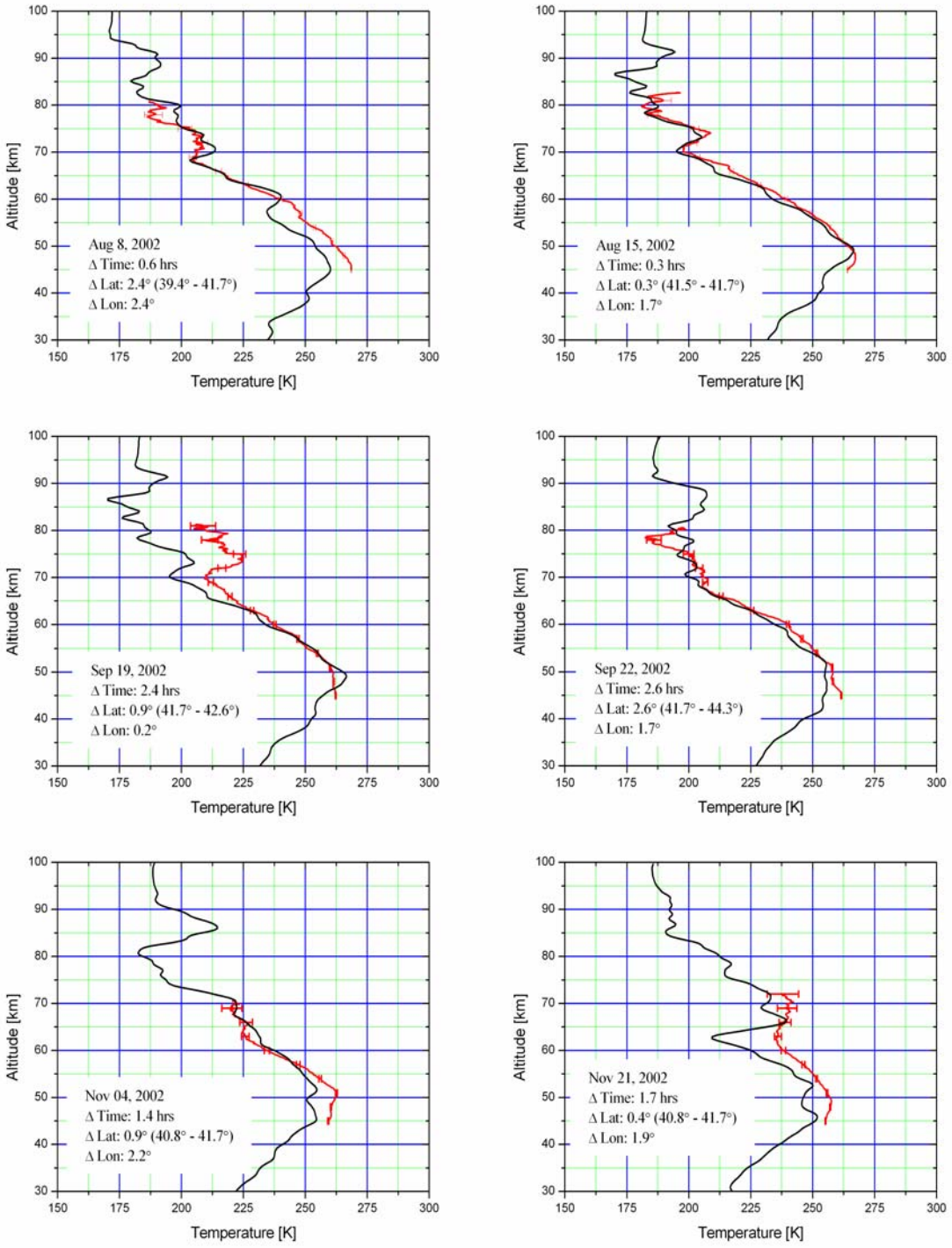

Figure 33. Nightly temperature comparison between SABER (black) and ALO(red). The SABER temperatures assume local thermodynamic equilibrium. The ALO temperatures are from averaging the two-min. photocount profiles for the night. The ALO uncertainties are from the measurement uncertainty, Eq. 3.3.26.

to how close the two profiles are temporally and spatially. As can be seen in Figure 33, on Aug 15, 2002 the temperatures are very close over most altitudes. The two measurements are also very close temporally and spatially 0.3 hrs, 0.3º in latitude, and 1.7º in longitude, respectively. The results from the Rayleigh lidar are a nightly average while those from SABER were taken over a very brief period (three minutes) and show more small-scale features. As a result, much of the short-term variability in the atmosphere is averaged out of the lidar profiles.

While the temperatures from the Rayleigh lidar show very good agreement with SABER at altitudes below 65 km, during some nights the results show a marked temperature difference above 65 km. Looking again at Figure 33, the results from Sept. 19, 2002 show differences between the temperatures at these higher altitudes, but as the results from the lidar are integrated downward, the difference decreases. The temperature differences between 45 km and 65 km are on average 0.16 K. While the mean differences between 65 km and 85 km is much larger at 5 K. As was discussed previously, the algorithm to derive temperatures from the Rayleigh lidar must use an initial temperature to start the temperature-reduction. This initial temperature was taken from the climatology found at CSU. It should be quite good for finding our climatological results. However, for individual nights, it could be off by 10 or 20 K because of geophysical variability. The difference between the two temperatures in the first 5 km is 13.5 K. Figure 34 shows temperature profiles starting with a ± 15 K error in the initial value at 83.9 km. The error at 75 km has dropped from 15 K to 3.4 K after

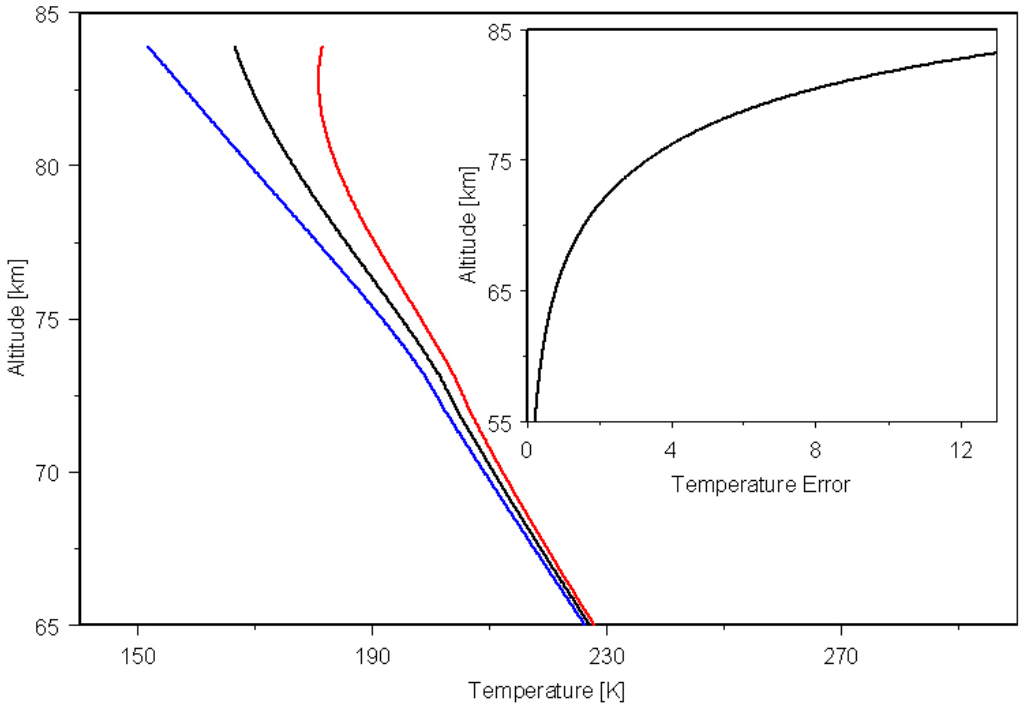

Figure 34. Temperature results assuming both a positive (red) and negative (blue) error in the starting temperature of 15 K. The black curve between the red and blue curves is the correct temperature. The black curve in the inset plot is the absolute value of the error for either case.

integrating for 8.9 km. Comparing the temperature differences between SABER and ALO on September 19, 2002, they drop almost the same amount in almost the same distance. The value of the initial temperature probably accounts for the high-altitude difference.

As the temporal and spatial differences increase, the temperature differences increase. This probably reflects real geophysical differences, providing insight into the dynamics of the atmosphere. Figure 31 shows the results from March 9, 2002. The temperatures from both instruments show a large oscillation between 55 and 65 km, but

with a 5 km difference in the altitude of the peak. This difference appears to be a phase shift in a wave arising from either the temporal or spatial offset of the measurements.

The comparison between the two instruments can be pursued further by averaging the temperatures from all 18 nights. There are enough nights that some of the geophysical variability should be averaged out. Two average temperature profiles were created from the eighteen temperature profiles, one from each instrument. These average temperatures show good agreement over the majority of the range of the lidar system (Figure 35). Along with the mean, the RMS variation of the mean was also found. The temperatures from the lidar system are higher than those generated from the SABER instrument at the lowest altitudes, near the stratopause. There is also a slight difference in the temperatures at the top 5 km, but this again is most likely due to the influence of the starting temperature.

While there are some small differences between the two instruments, the overall agreement is very good. This good agreement is particularly significant because the two sets of temperatures are derived by totally different techniques. As more data from the SABER instrument becomes available, we will continue to make comparisons when the satellite is directly overhead and when it is further away. The overhead comparison will continue the SABER validation in time. The distant comparisons will look for the propagation of structures in the temperature profiles.

4. Comparison with OHP

Another source of temperature measurements with which to compare are the pair

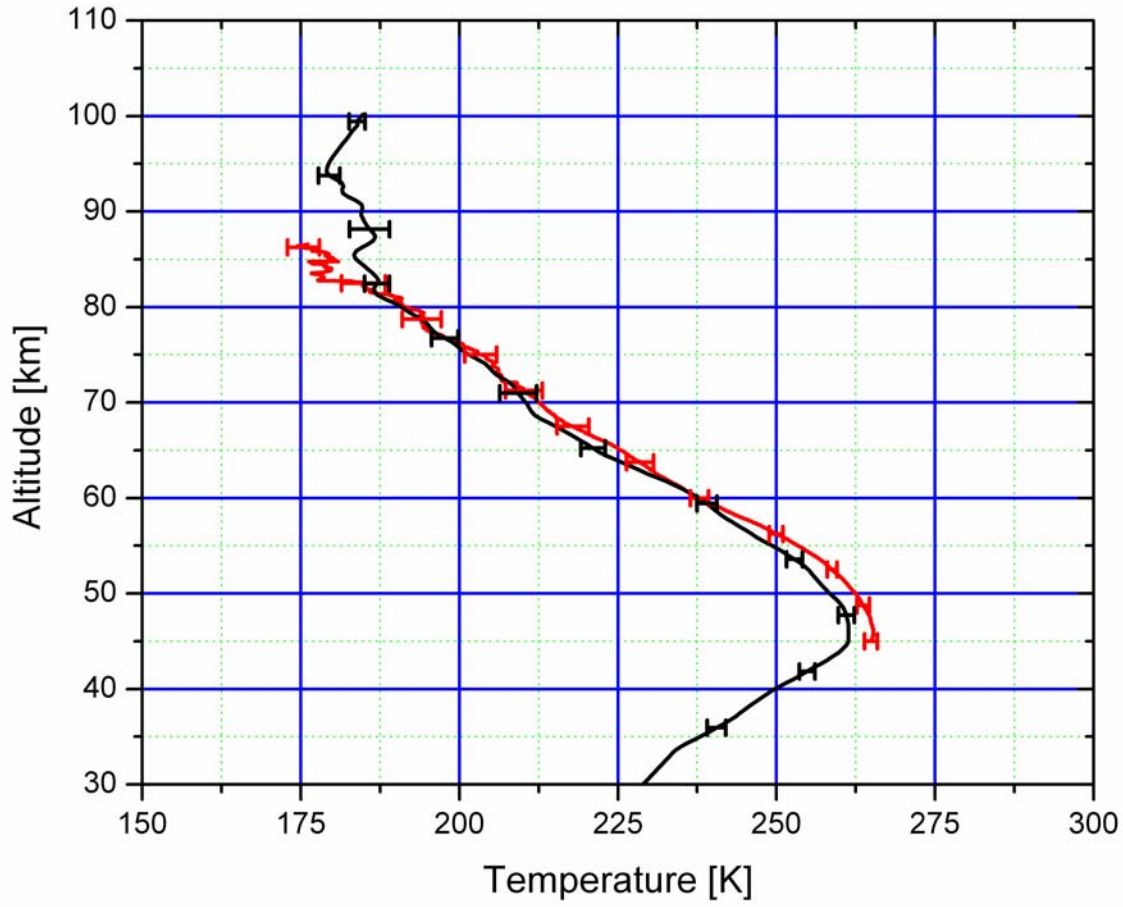

Figure 35. Average of the temperature profiles used in the SABER (black) – ALO (blue) comparison. The error bars are the standard deviation of the means for the 18 nights compared.

of Rayleigh-scatter lidars at Haute Provence (OHP) (44 N, 6 E) and Biscarrosse (BIS) (44 N, 1 W) [*Hauchecorne and Chanin*, 1980; *Chanin*, 1984; *Hauchecorne et al.*, 1991; *Keckhut et al.*, 1995]. These two lidars are at the same latitude but separated by 550 km. The reported temperatures cover an altitude range from 33 to 87 km, and cover a period from October 1978 to December 1989. While both of the French systems used larger telescopes, they used lower-power lasers, with the result the ALO and French systems are very comparable. The data from the French lidars have been averaged together to

produce nightly temperature profiles. When compared to one another, the nightly temperatures from each of the two French lidars were within 2 K of each other [*Hauchecorne et al.*, 1991].

The monthly results are plotted in Figures 36 and 37, with the results from the ALO lidar in red and those from the French systems in blue. The plotted error bars for the French data are the RMS variability of the nightly temperature, with the measurement uncertainty for a single night temperature profile being 10 K at 90 km and dropping to less than 1 K below 70 km. The measurement error bars for the ALO temperatures are the RMS variability calculated from the nightly temperature averages. Because the nightly temperatures start lower than the multi-year monthly averages, the error bars do not extend to the starting altitude.

The ALO temperature results are plotted from their starting altitude, with the first few kilometers of the data having a large dependence upon the starting temperatures as discussed in Chapter 5. However, because they were derived from a climatology, they should be close to the correct values.

There is generally good agreement between the temperature measurements made with the ALO Rayleigh lidar and the two French lidar systems. This is expected as the two systems are located at nearly the same latitude 42° N vs 44° N and the temperature structure of the atmosphere should not change much over 2º of latitude. The summer months, as would be expected because of less geophysical activity, show the greatest similarity between the two systems with July and August showing very good agreement.

During the winter months when there is the greatest amount of geophysical

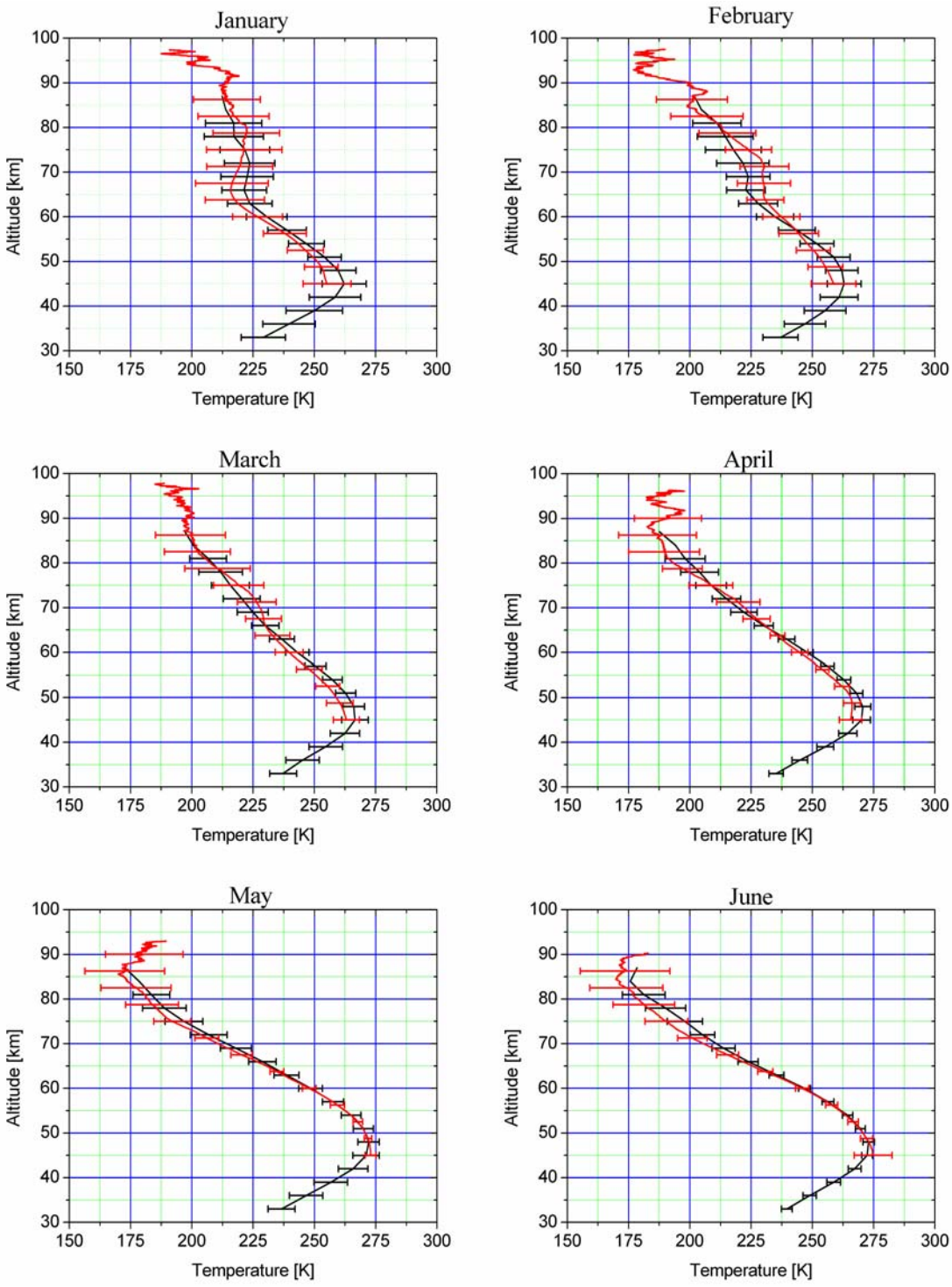

Figure 36. Temperature comparison between the OHP and ALO Rayleigh lidars. The data from the ALO Rayleigh lidar is in red. The data from the French lidar is black. The French and ALO error bars are the geophysical variability.

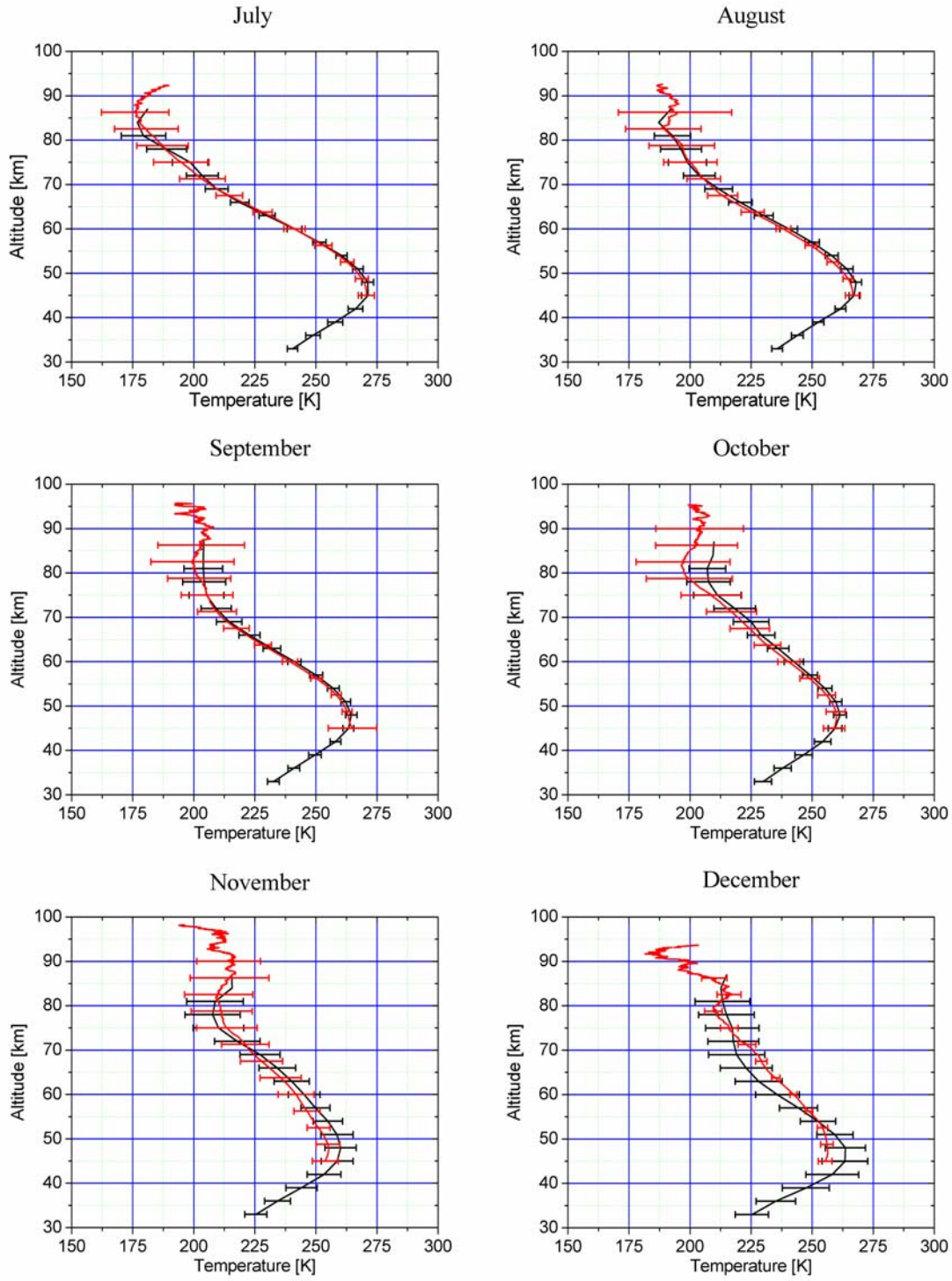

Figure 37. Temperature comparison between the OHP and ALO Rayleigh lidars. The data from the ALO Rayleigh lidar is in red. The data from the French lidar is black. The French error bars are the geophysical variability and the ALO error bars are temperature errors.

variability the temperature comparisons show the greatest differences. However, compared to the WINDII comparison, the results for December and January above 75 km are in good agreement. With the ALO Rayleigh lidar we typically see an inversion layer during the winter months, December through March, around 70 km. The inversion layer is present in the average profiles from the French lidar but over a much shorter period, January and February. It is generally thought inversion layers are formed due to the presence of gravity waves [*Hauchecorne and Maillard*, 1992]. The location of the ALO Rayleigh lidar in the middle of the Rockies, which is a major orographic source of gravity waves, may be the reason this temperature difference.

During the summer and fall periods, there is a noticeable difference between the two sets of temperatures at the higher altitudes. The French systems use an atmospheric model (CIRA86) to derive their initial temperatures. During the months from April to November, which are all of the months without visible inversion layers in the figures, the two temperature profiles approach each other as they are integrated downward. Because the results from the ALO lidar are plotted from their starting points, typically above 90 km, we know by 85 km the influence on the temperatures of the initial value is small. As was mentioned in Chapter 5, the initial temperatures for the ALO lidar were taken from another climatology [*She et al.*, 2000], which we believe gives a better initial value than the CIRA86 model. This decreasing difference could reflect either an incorrect initial value or, possibly, a cooling of the upper mesosphere in the 15 years between data sets.

Figure 38 gives the average of the twelve individual months from the French lidars and the ALO lidar system along with the corresponding RMS variation of the

means. The temperature measurements from the two systems are in the best agreement between 60 to 75 km showing the ALO temperature to be only slightly cooler. The French lidar reported a trend of -4 K/decade between 60 and 70 km [*Hauchecorne et al.*, 1991]. This close agreement would tend to contradict the French cooling trend.

With such a large time interval between the two sets of observations, ALO should see temperatures significantly lower than the French system, but the averaged temperatures from the ALO lidar between 60 and 75 km are down by less than 1 K on average. Below 55 km and above 75 however, the temperatures from the ALO lidar are

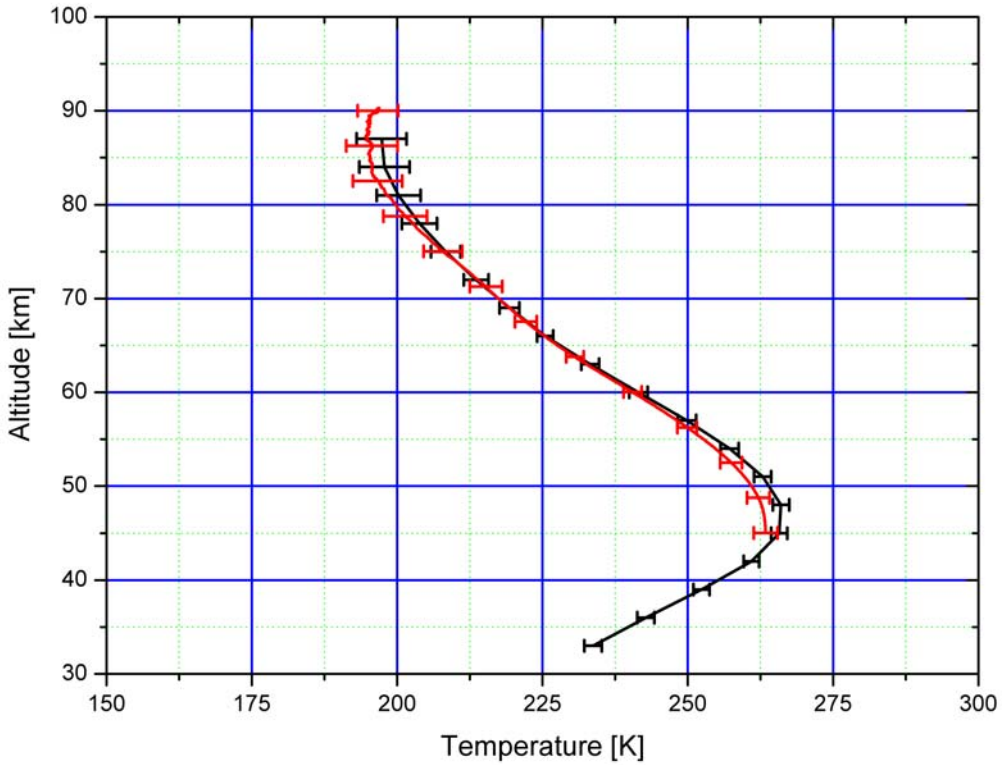

Figure 38. Yearly temperature averages of OHP (black) and ALO (red) lidars. The accompanying error bars for each curve are calculated from the RMS variation of the 12 monthly temperature profiles.

significantly cooler. As the ALO data have not been analyzed for secular trends, this serves as motivation for future trend analysis.

5. Comparison with OH Temperatures at 87 km

There are several airglow emission layers in the middle and upper atmosphere, which can be measured with passive optical instruments to determine the temperature. Three passive optical instruments — a Michelson interferometer, a temperature mapper, and a Fabry-Perot interferometer — have been located at Utah State University or near by at the Bear Lake Observatory (BLO) to measure these temperatures. They provided temperature measurements from the OH emissions. The peak of the OH emission layer is approximately 87 km and the emission layer is about 6 km thick [*Baker and Stair*, 1988].

The first of the three instruments was a Michelson interferometer, which could produce temperature measurements of the OH emission layer by measuring the rotational temperature of the OH(3,1) Meinel band [*Espy and Stegman*, 2002]. The temperature measurements from the BOMEM were taken intermittently during the period between November 1991 and December 1996. Nighttime averages of the rotational temperatures are given in Figure 39 as a function of day number, independent of year. The precision of the measurements were, on average, on the order of three percent [*Espy*, 2001] and a minimum of ten measurements were necessary for the nightly average to be determined [*Espy*, 2003].

The nightly temperature measurements were averaged into monthly means, and the dates were averaged to find where in the month to place the data point. Because of

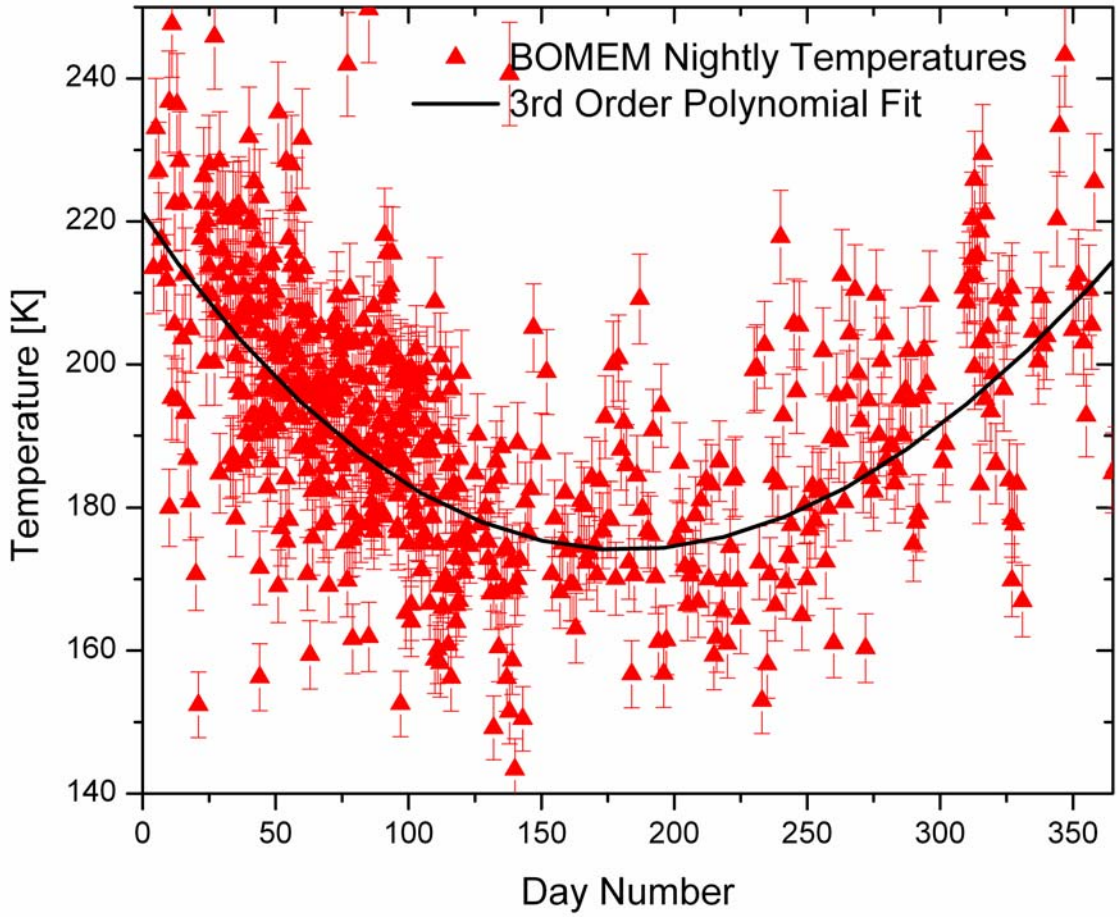

Figure 39. BOMEM nightly OH temperatures [*Espy*, 2003]. The error bars are three percent of the temperature observations. They represent uncertainty in the observation.

the large number of nightly averages, this usually averaged out to be close to the middle of the month. Because each nightly temperature measurement had an uncertainty of three percent of the measured temperature, the average monthly temperature uncertainty was also calculated (Figure 43, shown later).

The second instrument was the Mesospheric Temperature Mapper (MTM) operated by Mike Taylor. The temperature mapper measures the temperature of the OH layer via measurements of two rotational lines whose ratio is temperature sensitive [*Pendleton et al.*, 2000; *Taylor et al.*, 2001]. The temperature mapper ran at the Bear

Lake Observatory for only one year, spanning the second half of 2000 and the first half of 2001 with a few data gaps. The temperatures are shown in Figure 40. The temperatures from the MTM were averaged together into monthly averages in the same way as for the BOMEM data. The RMS variation of the mean for the monthly averages was also calculated.

The third instrument is a Fabry-Perot Interferometer (FPI) [*Rees et al.*, 1989] used to measure winds and temperatures from the OH layer. The temperature measurements from the FPI were taken at BLO from 1993 to 1995 [*Choi et al.*, 1997a; *Choi et al.*, 1997b]. Temperatures and uncertainties were derived from a nonlinear least squares fit

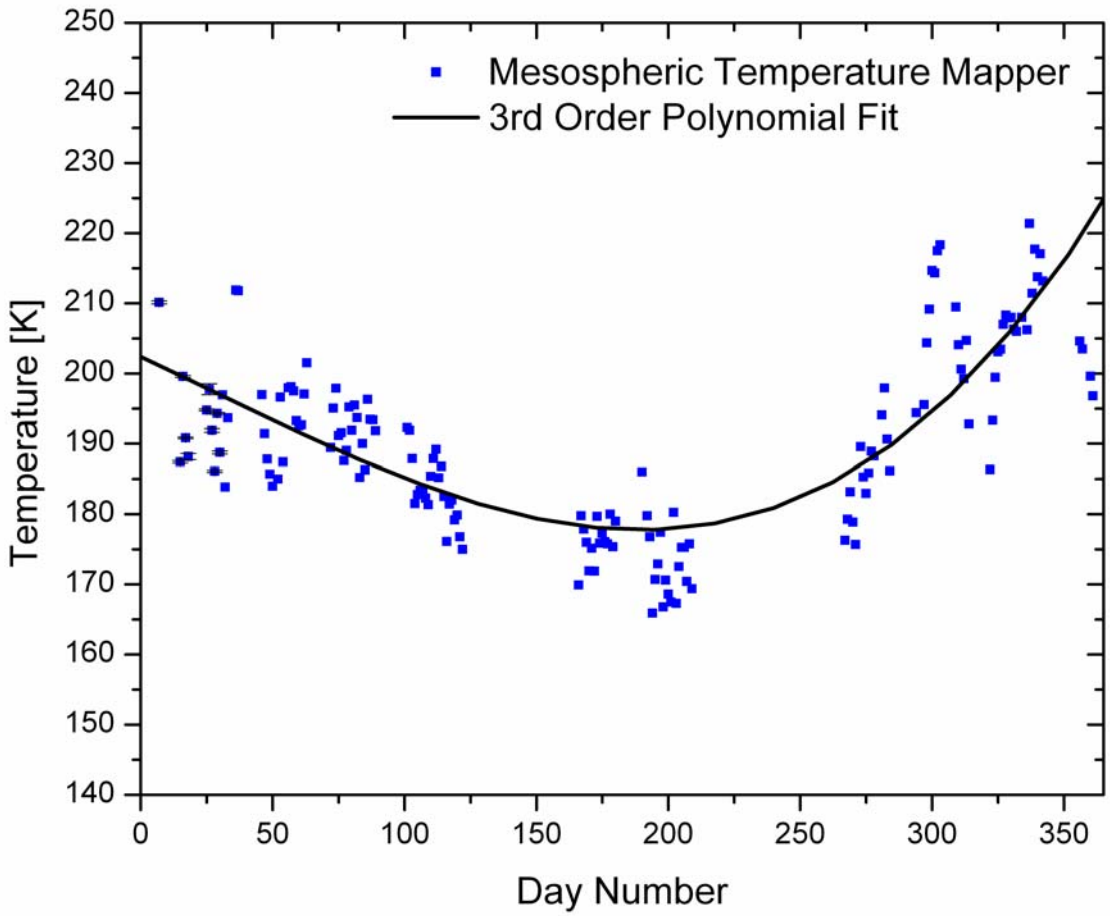

Figure 40. MTM Nightly OH temperatures [*Taori*, 2003].

to the Doppler shape of a rotational line at 843 nm.

Thus these are kinetic temperatures instead of rotational temperatures. They are shown in Figure 41. The available data gives good coverage to calculate monthly temperature averages and the associated measurement uncertainties (Figure 43, shown later).

To make comparisons of the ALO Rayleigh-scatter temperatures to the OH temperatures, it was necessary to use multi-year monthly averages based on the average of the two-minute photon-count profiles. The maximum altitude of the lidar was then

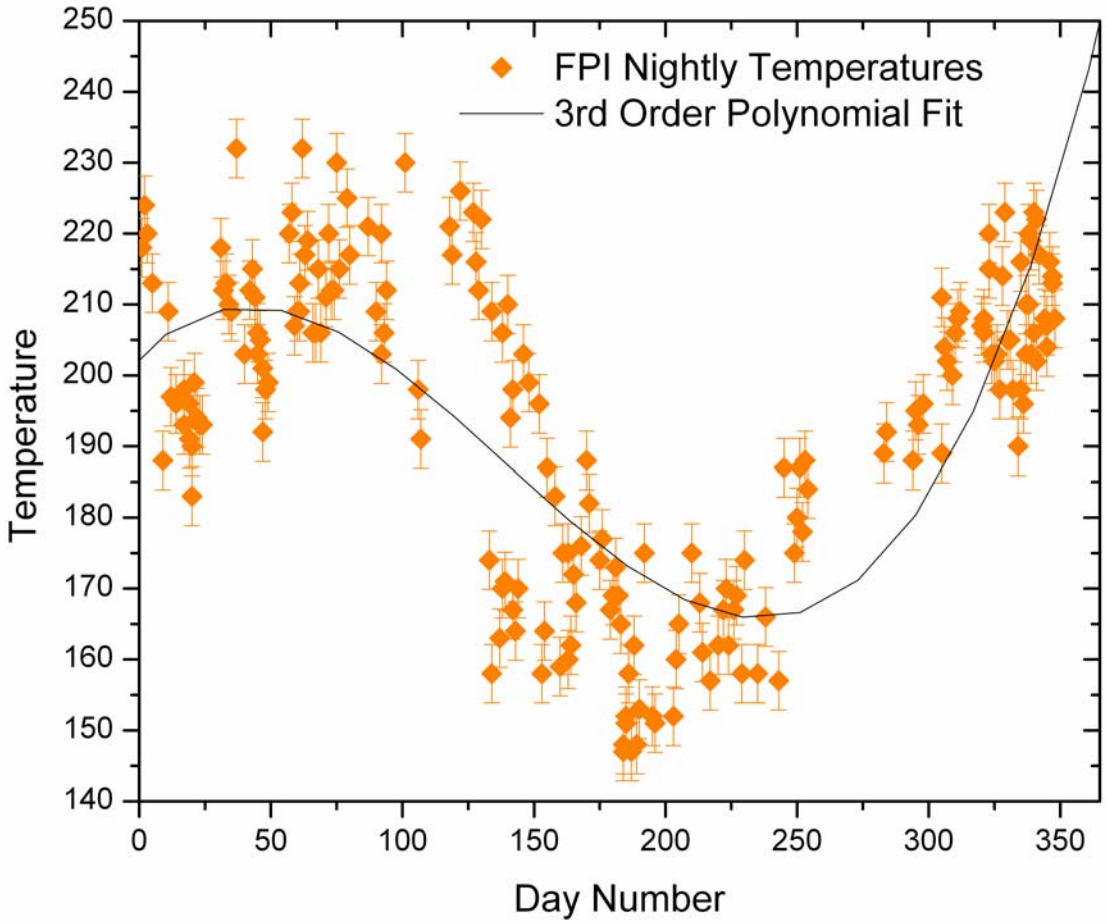

Figure 41. FPI nightly temperatures adapted from Choi et al. [*1997a,1997b*].

well above the midpoint of the layer. Typically the starting altitude for the lidar temperature-reduction is around 95 km. However, for some months there may be a small residual effect from the initial temperatures.

For simplicity, the OH layer has been assumed to have a distribution with a peak at ~87 km [*Taori*, 2003] with a FWHM of ~ 9 km (Table 9). Because the OH layer is not stationary the application of this weighting function to the lidar data is only an approximation, but it is adequate for this first comparison.

We have included results from the CSU sodium lidar, which provides the initial temperatures for the data reduction (Figure 42). The temperatures from the sodium lidar were weighted to compare to those from the Rayleigh lidar and the OH systems in Figure 43. The accuracy of the sodium measurements are ~ 0.6 K at the peak of the sodium layer (92 km) and ~ 5 K at the edges (81 km and 107 km) [*She et al.*, 2000].

The nightly temperature results from all of the instruments were combined into monthly temperature averages. The results from the two lidar systems are from temperature climatologies and have enough observations to give good average

Table 9. OH Weighting Function [*Taori*, 2003]

Altitude	OH wt fn	Altitude	OH wt fn
60	3.82478E-11	82	0.106513247
62	9.88944E-10	84	0.166450494
64	1.98129E-08	86	0.201547374
66	3.07562E-07	88	0.18909489
68	3.69939E-06	90	0.137465283
70	3.44776E-05	92	0.077431356
72	0.000248975	94	0.033794909
74	0.001393104	96	0.011428686
76	0.006039803	98	0.00299469
78	0.020289552	100	0.00060802
80	0.052812016		

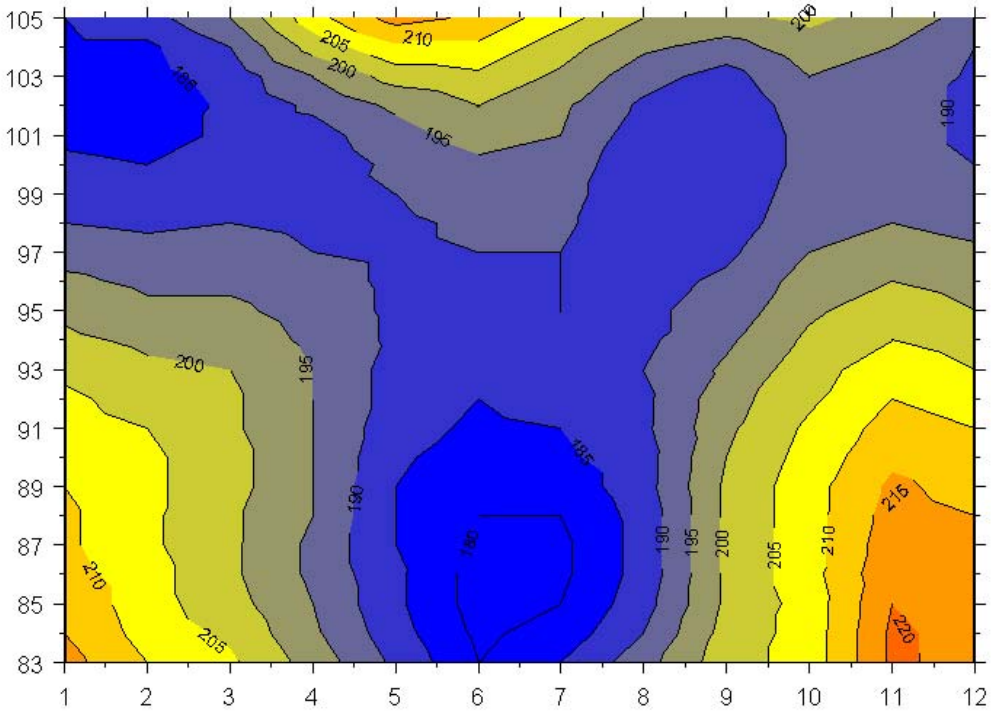

Figure 42. Contour plot of mesopause temperature from the CSU sodium lidar. These temperatures include effects from the Mount Pinatubo volcanic eruption in June 2001 [*She et al., 2000*].

temperature measurements. The other instruments were operated over two to five years, some months do not have adequate coverage for accurate monthly averages, and are dominated by geophysical variability. The number of nights of observations for everything but the lidars is given in Table 10. The results from the five systems described are shown in Figure 43. There is very close agreement, for example, between the BOMEM and the MTM during most of the year. However, the months of January and February show the MTM to be much cooler than any of the other instruments. Looking back to Figure 40 it appears the results from the MTM are subject to large

Table 10. OH Data Coverage Used for the Comparison

Month	MTM	BOMEM	FPI
January	12	47	19
February	16	103	20
March	22	114	20
April	20	101	9
May	2	42	20
June	15	28	20
July	19	27	19
August	0	27	14
September	6	29	7
October	17	25	6
November	18	31	23
December	11	18	21

oscillations and the data sampling has caused the results to be lower than normal [*Taylor*, 2003].

Ignoring the FPI for now, the Rayleigh lidar shows higher temperatures than the other two instruments from July to November, and in March and April. The Na lidar shows higher temperatures than the other two instruments in all months except January. As described in Chapter 2, the initial temperature for the Rayleigh lidar is taken from the climatology of the Sodium lidar at CSU, and is typically found at 95 km for the monthly reductions. However, as indicated elsewhere, the Rayleigh temperatures should be nearly independent of the initial temperatures after 10 km. Even with the weighting function, this is confirmed in May, June, and July when ALO finds temperature at 87 km approximately 10 K cooler than the CSU lidar. The summer difference between the Rayleigh and sodium lidars appears to be systematic. This should be investigated in the future.

The results from the FPI were the first results from a very difficult analysis.

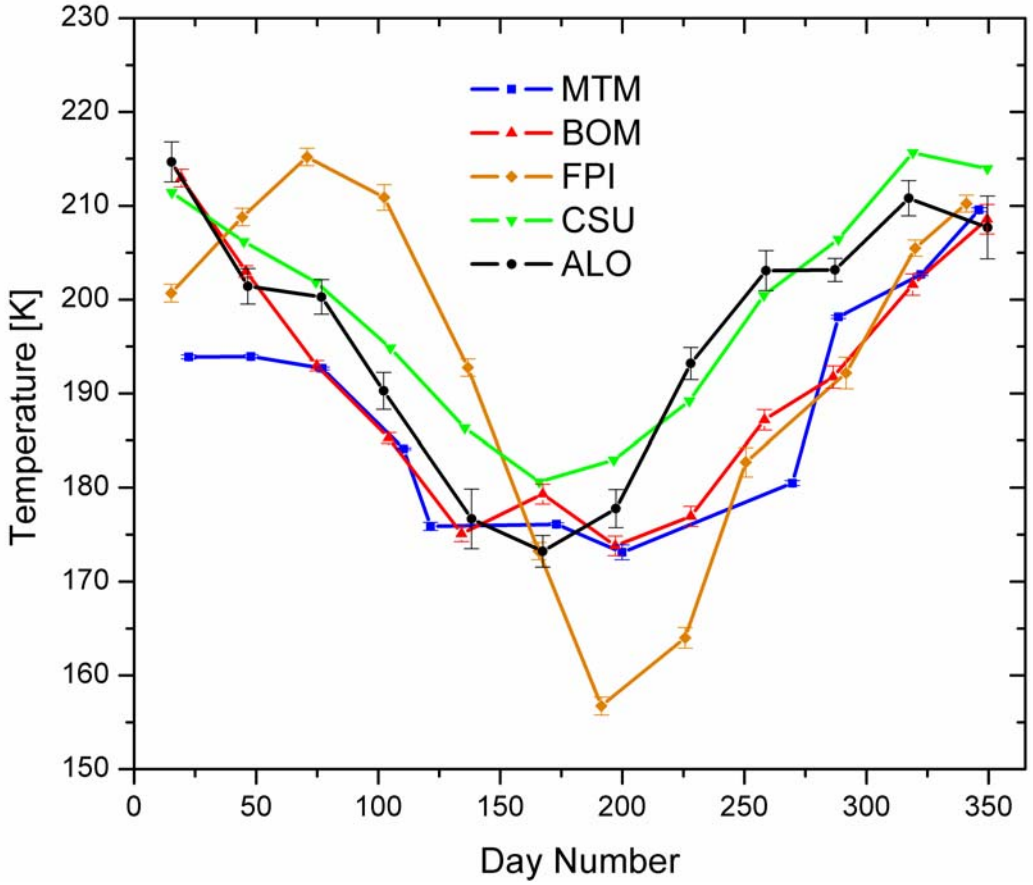

Figure 43. Temperature comparison at 87 km (approximate altitude of the OH layer).

However, the temperature results from the FPI are strongly dependent upon the calibration of the instrument, which was done infrequently because of the length of time it took [*Wickwar*, 2004]. It is highly likely the experimental technique contributed to the high temperatures in March and April and the low temperatures in July and August. The OH rotational temperatures agree very well with each other on all months except January, February, and September, when they differ by as much as 10 – 20 K. These differences could arise from the limited number of observations, geophysical variability, or both.

We can find the mean difference between the mean of the BOMEM and MTM, and the ALO lidar given as

$$\Delta T = T_{ALO} - \frac{T_{BOM} + T_{MTM}}{2}. \qquad 6.1$$

Because the temperature mapper had no results for August, the difference for that month was simply T_{ALO}-T_{BOM}. Table 11 gives the results of the calculation.

As seen from Table 11, there are several months where the temperature differences are less than 5 K. That is the case for the summer months, May, June, and July, and for December. Except for two of the months, the temperature results from the lidar are warmer than the mean of the BOMEM and MTM. The large temperature difference could arise from a variety of sources: geophysical variability, altitude or weighting problems, or a difference between the rotational and kinetic temperatures. Addition investigation will be needed to sort this problem out in the future.

6. Comparison with TIME-GCM

The TIME-GCM is a fully global circulation model developed by Ray Roble at National Center for Atmospheric Research (NCAR) [*Roble* and *Ridley*, 1994; *Roble*

Table 11. Temperature Difference Between ALO and Mean of BOMEM and MTM

Month	ΔT
January	11.3 K
February	2.9 K
March	7.5 K
April	5.6 K
May	1.2 K
June	-4.5 K
July	4.3 K
August	16.2 K
September	19.2 K
October	8.2 K
November	8.7 K
December	-1.4 K

1996]. The model employs a grid with points spaced 5º in latitude and 15º in longitude. The closest to ALO is at 42.5 N latitude and 105 E longitude. The model run was for the year 2002 (Figure 44). It included a full array of meteorological inputs at the lowest altitude, and magnetospheric and solar inputs at the highest altitudes. Among these is a full gravity wave parameterization. To compare with the lidar, which is currently only capable of nighttime operations, the TIME-GCM temperature profiles were selected for local midnight.

The results from the TIME-GCM model show a greater variability in the temperatures than has appeared in any of the lidar climatologies. They vary with periods between 5 and 15 days, which suggest planetary waves influence the model. The greater

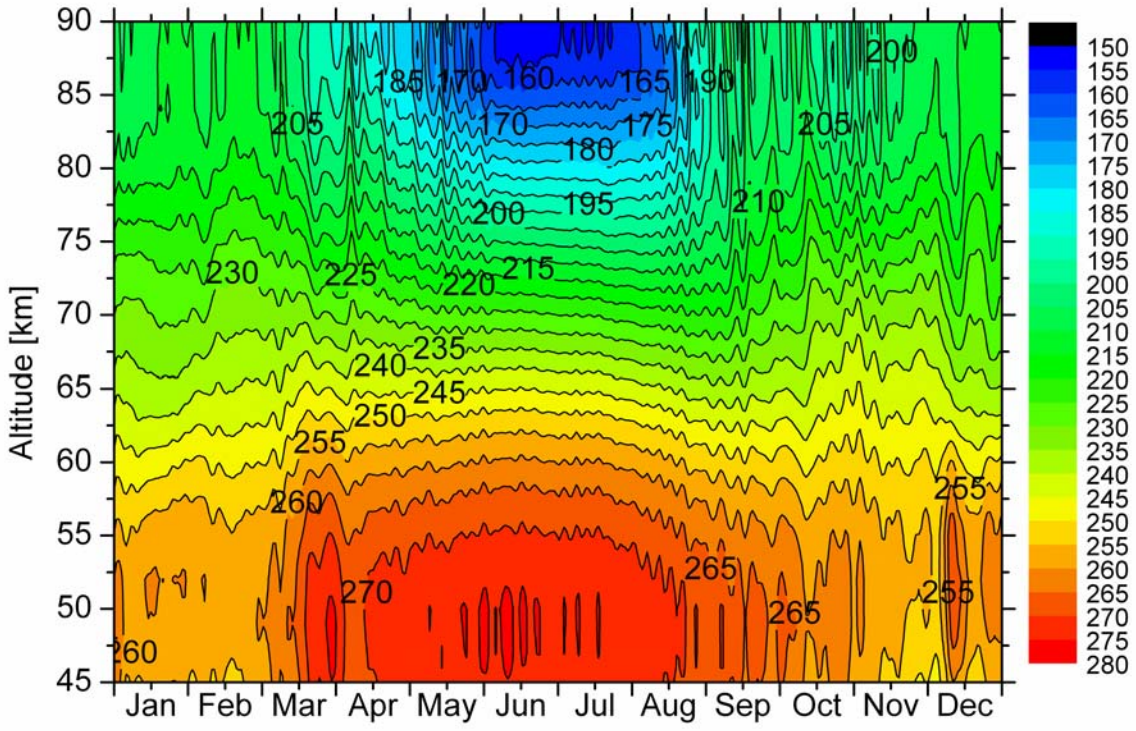

Figure 44. TIME-GCM results for daily midnight temperatures for 2002 at the grid point closest to ALO [*Roble*, 2003].

variability is not surprising as the results from the TIME-GCM are daily profiles, whereas the lidar climatologies are averaged over many days or many days in multiple years. Both the model and the lidar, Figure 25, show the greatest variability at the highest altitudes, between 80 and 90 km. The association of the large variation in the model at these high altitudes to small variations at much lower altitudes suggests much of this high-altitude variability in the observations is due to the growth of waves with altitude.

To compare the results from the TIME-GCM to those from the lidar, a 28-day boxcar average was performed. The results of this time averaging are given in Figure 45. This averaging has removed the short-term variations in the model results. While there is great similarity between the model and the lidar measurements, there are several significant differences. The maximum stratopause temperature given by the model is 275 K, very similar to the 274 K given by the lidar. Both give the maximum in June. However, the TIME-GCM gives the maximum temperature between 47.5 km and 50 km, while the lidar shows it is located below 47.5 km. Because the altitude of the stratopause and its temperature are largely due to the balance between O_3 heating and CO_2 cooling, errors in their distributions or the chemistry giving rise to their distributions might be the reason for the difference. It has also been suggested the difference might arise converting from pressure coordinates in the model to altitude for the observation.

The minimum temperature occurs at the mesopause during mid-summer and is due to atmospheric dynamics. The results from the lidar, Figure 19, show the minimum temperature to be 175 K centered about the first of June and 85 km in altitude. The results from the TIME-GCM give a minimum temperature of 155 K centered about the

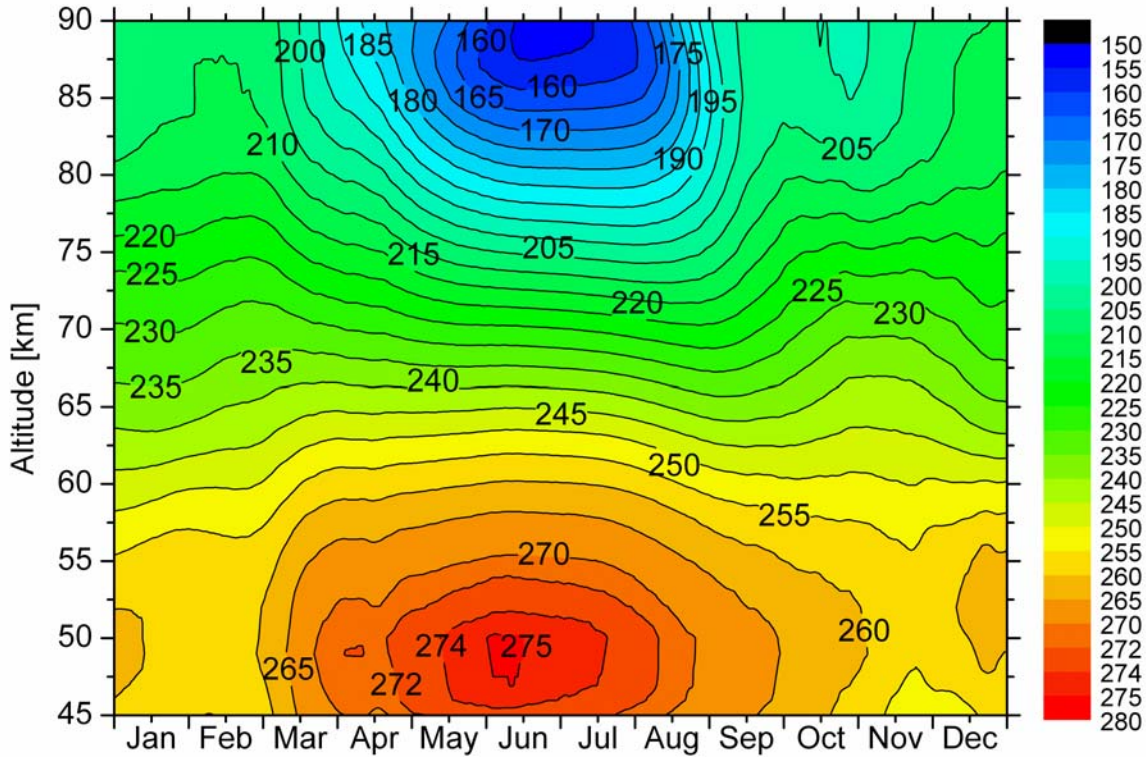

Figure 45. TIME-GCM results for daily midnight temperature for 2002 at the grid point closest to ALO with a 28-day boxcar average applied [*Roble*, 2003].

third week of June at ~ 88 km. Thus, the model gives a summer mesopause temperature minimum that is about 20 K cooler, three weeks later and 3 km higher. This is a big difference.

There are several very interesting similarities between the lidar and the model. During the October-November period, both the lidar and the model see a 200 K feature in the mesopause region. There are also increases in temperatures between 60 km and 80 km in October-November and February-March time periods. The differences and similarities between the lidar results and the TIME-GCM are motivation to determine the physics behind them. The TIME-GCM is a first principles model. Thus more

detailed comparisons in the future and an analysis of important terms in the model could give insights into the physics and chemistry of these significant features.

7. Conclusions

The comparisons between temperatures from the ALO Rayleigh-scatter lidar and other sources in this chapter give further confidence in the resulting temperature climatology. More importantly, they provide information on the geophysics or show the potential for learning about the geophysics.

The comparisons with the two satellites give different insights for each. While the comparison with the SABER instrument on the TIMED satellite contained relatively few days, 18 in total, it showed very good agreement for the simultaneous observations. Indeed, the closer the SABER observations were to ALO, the better was the agreement. Further observations may be able to show how the temperature structure varies with distance from ALO. In addition, temperature differences on occasion at the highest altitudes show the possibility of temperature fluctuation of some 15-20 K at these altitudes.

The WINDII instrument uses the same method to derive temperature, converting a density profile to temperature. While the technique is the same, the results show considerable difference during certain months. The largest disagreements between WINDII and ALO occur during the winter months when the geophysical variability is greatest, and show good agreement during the summer months when the geophysical variability is at a minimum.

The comparison with the OH temperatures is a difficult one to make. The

comparisons showed good agreement between the BOMEM and MTM to the ALO lidar over certain months and poor agreement during others. This comparison certainly merits future investigation. If possible a comparison between the lidar and an OH instrument should be carried out on a nightly basis to answer possible questions of the differences between the rotational and kinetic temperatures, weighting function, and emission altitude.

Comparisons with the TIME-GCM should provide great insight into the physics and chemistry of the middle atmosphere. This is done by noting what modifications are necessary to bring the model into agreement with the measurements, for instance the altitude of the summer stratopause. This is also done by examining the forcing terms in the model. For instance, what is needed to create the elevated temperatures seen in the contours above 70 km in February and November? This should help explain similar features in the observations. Furthermore, it would provide information for scaling inputs to the model to achieve better agreement. The inclusion of meteorological inputs in the model should also help in identifying meteorological effects in the observations.

CHAPTER 8

SUMMARY AND FUTURE

1. Summary

The observation philosophy of the ALO has been to make observations with the Rayleigh lidar whenever possible. This has provided good coverage of all the months of the year. These long-term frequent observations are necessary to produce accurate temperature climatologies. They also provide the possibility of finding unexpected events.

Unlike many passive instruments a Rayleigh-scatter lidar system requires continual maintenance to be operational. Without multiple trained personnel, it becomes increasingly difficult to maintain the instrument, make observations, and perform the necessary data analysis. The creation of the temperature climatology represents an enormous effort.

Part of this effort was to ensure the temperature results derived from the lidar data are accurate. Some of this involved the hardware. The detection system was proven to make accurate measurements at the high count rates encountered at lower altitudes. Some of this effort involved the software. Examining the data and the algorithms was facilitated by simulating the lidar signal and data. As a result, possible sources of systematic errors were characterized, including the importance of the initial temperature, the accuracy of the background measurement, and the variation of gravity with height. The final temperature-reduction algorithm was applied to the MSISe90 model, retrieving correct results, and was compared to the independent data-reduction

algorithm used by the Purple Crow lidar producing the same temperature profile. Part of this effort was to find ways to distinguish between good and bad data. A set of criteria were developed and applied to every day in the data set. They are given in Chapter 5. The temperature climatology is given in Table 5 and the RMS variability is given in Table 6.

To prove the accuracy of the lidar climatology further, the data set was divided into two different data sets. The average temperature profiles from the two data sets were found and showed good agreement. However, the differences often exceeded the RMS variation of the mean, suggesting a distribution function with wings greater than for a Gaussian distribution. The summer months, in general, showed better agreement than the winter months, as expected because the winter months have a greater day-to-day and year-to-year geophysical variability.

The temperatures and temperature climatology were then compared to other temperature observations and to model calculations. This was done in part to insure there were no surprises in the ALO results arising from the data or data reduction. This was done most importantly to look for similarities and differences that can be followed up on later to learn about the physics and chemistry of the mesosphere.

In general the ALO climatology compares well with the majority of the instruments and extremely well with others. Having verified the reduction techniques from both the PCL lidar and the ALO lidar were equivalent, the climatology from the ALO lidar was compared to the climatology from PCL. They show very good agreement and some interesting features, which will bear future study. One example would be the presence of a large inversion during the month of February that was seen in

both lidars. Second the two lidars being at approximately the same latitude should show the same temperature structure. While close the temperature structure shows some differences, for example at both summer stratopause and mesopause, and may be due to longitudinal effects.

The results from the lidar were also compared to those from two satellites. The first comparison was done with the WINDII instrument on the UARS satellite. The averaged temperatures from WINDII and the ALO climatology compared well. The data for WINDII were taken over a three-year period. However, some months contain data from only one year. These differed significantly from the ALO temperatures reinforcing the possibility of large inter-annual variability, especially in winter. In contrast, March for example, contained the most data and had the best agreement with ALO. The second comparison was with the SABER instrument on the TIMED satellite and involved individual nights instead of long-term averages. This comparison only involved 18 days, but gave very good agreement. The nights with the highest level of coincidence in time and space showed the best agreement to the lidar. This was reassuring as the two instruments derive the temperature from very different methods. This also suggests the temperature structure can be examined as a function of distance from ALO.

The next comparison was with the climatology from the French lidar group at OHP. This comparison is very interesting in that the data for their climatology was taken 15 years before the ALO measurements. In their paper [*Hauchecorne et al.*, 1991] a cooling trend of -4 K/decade was reported between 60 and 70 km. While the ALO results were found to be cooler on average between 60 and 70 km they were only

slightly cooler. In contrast, the regions above 70 and below 60 km were significantly cooler. Because the ALO results have not been analyzed for trends, we cannot say this is proof of a smaller cooling trend between 60 and 70 km and a larger trend at higher and lower altitudes, but it does serve as motivation for the analysis to be done.

The next comparison was done with several instruments that produce temperature measurements of the OH emission very close to ALO. A Fabry-Perot Interferometer (FPI), a Michelson Interferometer (BOMEM), and a Temperature Mapper (MTM), were in this group. The rotational temperature from the BOMEM and the MTM showed close agreement to the lidar during three summer months. During the rest of the year, the lidar found temperatures that were systematically warmer than the OH measurements. Additional work will have to be done to determine whether the difference arises from interannual variability, the altitude of the OH emission layer, or differences between rotation and kinetic temperatures.

The final comparison was carried out with the TIME-GCM. The TIME-GCM provided temperature results for every night that were averaged to match the ALO climatology. Highly significant differences were found in the stratopause and mesopause regions. Also, similar temperature structures were found in February and November. Understanding the cause of these differences and these structures will give insight into the physics and chemistry of the mesosphere.

2. Future Work

Several comparisons are necessary with different instruments and models. The comparison with the PCL needs to be extended to examine whether the difference

between the stratopause and mesopause temperatures are due to our orographic source of gravity waves. Perhaps these comparisons could also be extended to current OHP data.

The initial comparison with the SABER instrument used nightly averages showing very good agreement. These need to be extended with additional data and the new SABER data-reduction algorithm. Comparisons can be carried out with the hourly instead of nightly temperature profiles increasing the temporal coincidence. Moreover, a comparison with the SABER instrument can be used to give insight into the horizontal scale sizes and the motions of the temperature structure by comparing profiles when the satellite is at different distances from the lidar.

The TIME-GCM can be used to gain an understanding of the physics and chemistry of the mesosphere. This can be done primarily by modifying inputs to the model to bring the calculation into agreement with the observations. For example, the cause of the temperature structures above 70 km during February and November is still unknown.

The lidar system is currently in the middle of an upgrade. The largest change to the Rayleigh lidar is an increase in the size of the receiving telescope. The current telescope is a 44-cm Newtonian telescope, and the new system will comprise four telescopes the primary of each having a 1.25-m diameter. The total collecting area of the new system will be the equivalent of a 2.5-m telescope. The new telescope can be moved ± 270 degrees in azimuth off of north and 45 degrees in elevation off of zenith. This upgrade will increase the collecting area, and therefore the return signal, of the lidar by some thirty times. This increase in area will enable us to decrease the temperature uncertainty, increase the maximum altitude of the lidar, and use shorter integration

times. Two additional receiver channels will be used to take the measurements down into the stratosphere. The pointing capability will also enable us to make measurements of the spatial structure.

A fluorescence lidar will soon be in operation in conjunction with the Rayleigh-scatter lidar system. The system will measure the return from potassium deposited in the upper atmosphere from meteorites. The fluorescence-backscatter cross section of potassium is much larger than the Rayleigh cross section and a large signal can be measured with a modestly sized laser. Temperature can be derived from the detailed shape of the potassium spectrum. The resulting temperatures can also be used to improve the Rayleigh-lidar temperature-reduction by providing the initial temperature in the region from 80 to 110 km.

With the addition of the new telescope and potassium lidar, it will also be possible to measure the Doppler shift of the potassium spectrum to determine the wind field in the transition region from the mesosphere to the thermosphere. This will be a totally new capability for ALO and for potassium lidars.

After the upgrade to the lidar is finished and we have both the Rayleigh and resonance lidars working, the next goal is the addition of daytime measurements. To make daytime measurements, a narrow filter is necessary to minimize the amount of sunlight that enters the system. For the resonance lidar, a magneto-optical filter can be used. Daytime measurements with the Rayleigh lidar require the use of two or three Fabry-Perot etalons in tandem, which have to be capacitance stabilized. This is a more costly upgrade than the magneto-optical filter. The addition of a daytime capability will dramatically increase the capabilities of the lidar, particularly for measuring tides.

A method for properly determining the effect of gating and high signal on the PMT would be of considerable worth as this has been a problem in the past. In addition to their testing, PMT's with higher quantum efficiencies would increase the accuracy and range of the lidar.

The comparison with the OH emission at 87-km could also be extended in the future. Currently, there is no operational system at the BLO that can measure the OH temperatures or altitudes. The discrepancy found between Rayleigh and Na temperatures can be examined with the addition of the K Lidar.

There is also a considerable amount of work that can be done with the temperature data now available from the ALO lidar. The analysis of the temperature results for secular trends is needed and is currently underway. The temperature profiles can also be analyzed for effects from tides and planetary waves [*Nelson*, 2004]. The energy in the shorter-period gravity waves is being analyzed using the fluctuations in the relative density profiles.

REFERENCES

Argall, S., Personal Communication in regard to comparison between Purple Crow Lidar and the Atmospheric Lidar Observatory, edited by J. Herron, London, Ontario, Canada, 2003.

Baker, D.J., and A.T. Stair, Jr., Rocket measurements of the altitude distributions of the hydroxyl airglow, *Phys. Scripta*, *37*, 611–622, 1988.

Banks, P.M., and G. Kockarts, *Aeronomy*, 785 pp., Academic, New York, 1973.

Beissner, K.C., Studies of mid-latitude mesospheric temperature variability and its relationship to gravity waves, tides, and planetary waves, Ph.D. thesis, Utah State University, Logan, UT, 1997.

Chanin, M.-L., Review of lidar contributions to the description and understanding of the middle atmosphere, *J. Atmos. Terr. Phys.*, *46*, 987–993, 1984.

Chanin, M.-L., and A. Hauchecorne, Lidar studies of temperature and density using Rayleigh scattering, in *Ground-Based Techniques*, edited by R.A. Vincent, pp. 87–98, SCOSTEP Secretariat, University of Illinois, Urbana, IL, 1984.

Choi, G.-H., I.K. Monson, V.B. Wickwar, and D. Rees, Seasonal and diurnal variations of temperature near the mesopause from Fabry-Perot interferometer observations of OH Meinel emissions, *Adv. Space. Res.*, *21*, (6)847–(6)850, 1997a.

Choi, G.-H., I.K. Monson, V.B. Wickwar, and D. Rees, Seasonal variations of temperature near the mesopause from Fabry-Perot interferometer observations of OH Meinel emissions, *Adv. Space Res.*, *21*, (6)843–(6)846, 1997b.

Donovan, D.P., J.A. Whiteway, and A.I. Carswell, Correction for nonlinear photon-counting effects in lidar systems, *Appl. Opt.*, *32*, 6742–6753, 1993.

Espy, P.J., Bomem Temperatures from Utah State University, edited by V.B. Wickwar, Logan, 2001.

Espy, P.J., Reanalysis of BOMEM temperatures from USU, edited by J.P. Herron, Logan, 2003.

Espy, P.J., and J. Stegman, Trends and variability of mesospheric temperature at high latitudes, *Phys. and Chem. of the Earth*, *28*, 531, 2002.

Gardner, C.S., D.C. Senft, T.J. Beatty, R.E. Bills, and C.A. Hostetler, Rayleigh and sodium lidar techniques for measuring middle atmosphere density, temperature and wind perturbations and their spectra, in *World Ionosphere/Thermosphere Study, WITS HANDBOOK*, edited by C.H. Liu, pp. 148–187, SCOSTEP Secretariat, University of Illinois, Urbana, IL, 1989.

Hauchecorne, A., and M.L. Chanin, Density and temperature profiles obtained by lidar between 35 and 70 km, *Geophys. Res. Lett.*, *7*, 565-568, 1980.

Hauchecorne, A., M.-L. Chanin, and P. Keckhut, Climatology and trends of the middle atmospheric temperature (33–87 km) as seen by Rayleigh lidar over the south of France, *J. Geophys. Res.*, *96*, 15297–15309, 1991.

Hauchecorne, A., M.L. Chanin, and R. Wilson, Mesospheric temperature inversion and gravity wave breaking, *Geophys. Res. Lett.*, *14*, 933-936, 1987.

Hauchecorne, A., and A. Maillard, The mechanism of formation of inversion layers in the mesosphere, *Adv. Space Res.*, *12*, (10)219–(10)223, 1992.

Hedin, A.E., Extension of the MSIS thermosphere model into the middle and lower atmosphere, *J. Geophys. Res.*, *96* (A2), 1159-1172, 1991.

Hedin, A.E., M.A. Biondi, R.G. Burnside, G. Hernandez, R.M. Johnson, T.L. Killeen, C. Mazaudier, J.W. Meriwether, J.E.S. Salah, R. J., R.W. Smith, N.W. Spencer, V.B. Wickwar, and T.S. Virdi, Revised global model of thermosphere winds using satellite and ground-based observations, *J. Geophys. Res.*, *96*, 7657–7688, 1991.

Jursa, A.S., ed, *Handbook of Geophysics and the Space Environment*, Air Force Geophysics Laboratory, Air Force Systems Command, United States Air Force, 1985.

Keckhut, P., A. Hauchecorne, and M.L. Chanin, Midlatitude long-term variability of the middle atmosphere: Trends and cyclic and episodic changes, *J. Geophys. Res.*, *100*, 18887–18897, 1995.

Leblanc, T., I.S. McDermid, A. Hauchecorne, and P. Keckhut, Evaluation of optimization of lidar temperature analysis algorithms using simulated data, *J. Geophys. Res.*, *103* (D6), 6177–6187, 1998.

Measures, R.M., *Laser Remote Sensing Fundamentals and Applications*, 510 pp., Krieger Publishing Company, Malabar, FL, 1992.

Meriwether, J.W., X. Gao, V.B. Wickwar, T.D. Wilkerson, K. Beissner, and M.E. Hagan, Observed Coupling of the Mesosphere Inversion Layer to the Thermal Tidal Structure, *J. Geophys. Res.*, *Submitted*, 1997.

Meriwether, J.W., X. Gao, V.B. Wickwar, T.D. Wilkerson, K.C. Beissner, S.C. Collins, and M.E. Hagan, Observed coupling of the mesosphere inversion layer to the thermal tidal structure, *Geophys. Res. Lett.*, *25*, 1479–1482 & 2127, 1998.

Nelson, K.L.M., Lidar Observations of Oscillations in the Middle Atmosphere, Utah State University, Logan, 2004.

NIMA, Department of Defense World Geodetic System 1984 — Its definition and relationships with local geodetic systems, National Imagery and Mapping Agency, Bethesda, MD, 2000.

Pendleton, W., Jr., M.J. Taylor, and L.C. Gardner, Terdiurnal Oscillations in OH Meinel rotational temperatures for fall conditions at northern mid latitude sites, *GRL*, *27* (12), 1799-1802, 2000.

Rees, D., I. McWhirter, A. Aruliah, and S. Batten, Upper Atmospheric Wind and Temperature Measurements Using Imaging Fabry-Perot Interferometers, in *WITS Handbook,*, edited by C.H. Liu, pp. 188–223, SCOSTEP and Univ. of Illinois, Urbana, IL, 1989.

Roble, R.G., The NCAR thermosphere-ionosphere-mesosphere-electrodynamics general circulation model (TIME-GCM), in *STEP: Handbook of ionospheric models*, edited by R.W. Schunk, pp. 281–288, Utah State University / SCOSTEP, Logan, 1996.

Roble, R.G., TIMED-GCM results for 2002 at the Bear Lake Observatory (BLO), edited by V.B. Wickwar, Logan, 2003.

Roble, R.G., and E.C. Ridley, A thermosphere-ionosphere-mesosphere-electrodynamics general circulation model (time-GCM): Equinox solar cycle minimum simulations (30-500 km), *Geophys. Res. Lett.*, *21*, 417-420, 1994.

She, C.Y., S. Chen, Z. Hu, J. Sherman, J.D. Vance, V. Vasoli, M.A. White, J.R. Yu, and D.A. Krueger, Eight-year climatology of nocturnal temperature and sodium density in the mesopause region (80 to 105 km) over Fort Collins, CO (41 N, 105 W), *Geophys Res. Lett.*, *27* (20), 3289-3292, 2000.

She, C.Y., S.W. thiel, and D.A. Krueger, Observed episodic warming at 86 and 100 km between 1990 and 1997: Effects of Mount Pinatubo eruption, *Geophys. Res. Lett.*, *25*, 497–500, 1998.

Shepherd, M.G., B. Prawirosoehardjo, S. Zhang, B.H. Solheim, G.G. Shepherd, V.B. Wickwar, and J.P. Herron, Retrieval and validation of mesospheric temperatures from WINDII observations, *J. Geophys. Res.*, *104* (A11), 24813-24829, 2001.

Sica, R.J., S. Sargoytchev, P.S. Argall, E.F. Borra, L. Girard, C.T. Sparrow, and S. Flatt, Lidar measurements taken with a large-aperture liquid mirror. 1. Rayleigh-scatter system, *Appl. Optics*, *34* (30), 6925–6936, 1995.

Taori, A., Bear Lake Observatory Temperature Mapper Results, edited by J.P. Herron, Logan, 2003.

Taylor, M.J., Aliasing of the MTM measurements., edited by J.P. Herron, Logan, 2003.

Taylor, M.J., L.C. Gardner, and W. Pendleton, Jr., Long period wave signatures in mesospheric OH Meinel (6,2) band intensity and rotational temperature of mid latitudes, *Ad. Space Res.*, *27* (6-7), 1171-1179, 2001.

Wickwar, V.B., Conversation concerning the FPI results from the BLO observatory, edited by J.P. Herron, Logan, 2004.

Wickwar, V.B., T.D. Wilkerson, M. Hammond, and J.P. Herron, Mesospheric temperature observations at the USU / CASS Atmospheric Lidar Observatory (ALO), in *Remote Sensing of the Atmosphere, Environment, and Space*, pp. 272–284, SPIE, Sendai, Japan, 2000.

APPENDICES

Appendix A

Variation of Gravity with Height

The original gravity calculation used in the ALO temperature algorithm was based upon the simple $1/r^2$ fall off with the affects of centrifugal acceleration added. In comparison the gravity calculation employed by the PCL lidar is found in "The Handbook of Geophysics and the Space Environment" produced by the Air-Force [*Jursa*, 1985]. This algorithm is a Taylor series expansion of gravity above and ellipse and is discussed below. The value of gravity on an ellipse can be calculated by the following approximation:

$$\gamma = \gamma_0 \cdot \frac{1 + k \cdot \sin(\phi)^2}{\sqrt{1 - e^2 \cdot \sin(\phi)^2}}.$$

When the geodectic height is small, the normal gravity above the ellipsoid can be estimated by using an upward truncated Taylor series.

$$\gamma(h) = \gamma_0 + \left(\frac{d}{dh}\gamma_0\right) \cdot h + \frac{1}{2} \cdot \left(\frac{d^2}{dh^2}\gamma_0\right) \cdot h.$$

A frequently used expansion for the normal gravity above the ellipsoid with a positive direction along the geodetic normal to the ellipsoid can be expressed as the following:

$$\gamma(h) = \gamma_0 \cdot \left[1 - \frac{1}{2} \cdot \left(1 + f + m - 2 \cdot f \cdot \sin(\phi)^2\right) \cdot h + \frac{3}{a^2} \cdot h^2\right].$$

This expansion is employed by the PCL lidar system, but as the source for the equation is older, most of the coefficients have been updated.

As the algorithm used by ALO was in need of updating, it was decided since the full formula for propagation of g was available it would be used instead of the Taylor series expansion. The following calculation for gravity above an ellipsoid is given in the Department of Defense World Geodetic System [*NIMA*, 2000] and also gives the

updated parameters for the Taylor's series expansion. The calculation of g is dependent upon the following variables:

ϕ	geodetic latitude
λ	geodetic longitude
h	height
GM	gravitational constant of the Earth including the atmosphere
ω	angular rotation of the Earth
a	semi-major axis of the Earth
b	semi-minor axis of the Earth
e	linear eccentricity
γ_p	theoretical gravity at the pole
γ_e	theoretical gravity at the equator
f	ellipsoidal flattening
N	radius of curvature in the prime vertical
x	rectangular coordinate x
y	rectangular coordinate y
z	rectangular coordinate z

$$k = \frac{b \cdot \gamma_p}{a \cdot \gamma_e} - 1 .$$

$$E = \sqrt{a^2 + b^2} .$$

$$m = \frac{\omega^2 \cdot a^2 \cdot b^2}{GM} .$$

$$N = \frac{a}{\sqrt{1 - e^2 \cdot \sin^2(\phi)}}.$$

$$x = (N + h) \cdot \cos(\phi) \cdot \cos(\lambda).$$

$$y = (N + h) \cdot \cos(\phi) \cdot \sin(\lambda).$$

$$z = \left(\frac{b^2}{a^2} \cdot N + h\right) \cdot \sin(\phi).$$

$$u = \sqrt{\frac{1}{2} \cdot \left(x^2 + y^2 + z^2 - E^2\right) \cdot \left[1 + \sqrt{1 + \frac{4 \cdot E^2 \cdot z^2}{\left(x^2 + y^2 + z^2 - E^2\right)}}\right]}.$$

$$\beta = \tan^{-1}\left(\frac{z \cdot \sqrt{u^2 + E^2}}{u \cdot \sqrt{x^2 + y^2}}\right).$$

It is easiest to start the calculation of gravity about an ellipse in the elliptical coordinate system. The first coordinate u is the semi-major axis, the second coordinate β is the reduced latitude, and the third is the geocentric longitude. Since there is symmetry about the longitudinal axis, the normal component of gravity in this direction is zero.

$$w = \sqrt{\frac{u^2 + E^2 \cdot \sin(\beta)^2}{u^2 + E^2}}.$$

$$q = \frac{1}{2} \cdot \left[\left(1 + 3 \cdot \frac{u^2}{E^2}\right) \cdot \tan^{-1}\left(\frac{E}{u}\right) - 3 \cdot \frac{u}{E}\right].$$

$$q_1 = \frac{1}{2} \cdot \left[\left(1 + 3 \cdot \frac{b^2}{E^2}\right) \cdot \tan^{-1}\left(\frac{E}{b}\right) - 3 \cdot \frac{b}{E}\right].$$

$$q_2 = 3 \cdot \left(1 + \frac{u^2}{E^2}\right) \cdot \left(1 - \frac{u}{E} \cdot \tan^{-1}\left(\frac{E}{u}\right)\right) - 1.$$

$$\gamma_u = \frac{-1}{w}\cdot\left[\frac{GM}{u^2+E^2}+\frac{\omega^2\cdot a^2\cdot E}{u^2+E^2}\cdot\frac{q_2}{q_1}\cdot\left(\frac{1}{2}\cdot\sin(\beta)^2-\frac{1}{6}\right)\right]$$
$$+\frac{1}{w}\cdot\omega^2\cdot\sqrt{u^2+E^2}\cdot\sin(\beta)\cdot\cos(\beta).$$

$$\gamma_\beta = \frac{1}{w}\cdot\frac{\omega^2\cdot a^2}{\sqrt{u^2+E^2}}\cdot\frac{q}{q_1}\cdot\sin(\beta)\cdot\cos(\beta)-\frac{1}{w}\cdot\omega^2\cdot\sqrt{u^2+E^2}\cdot\sin(\beta)\cdot\cos(\beta).$$

$$\gamma_\lambda = 0.$$

$$\gamma_{Normal} = \sqrt{\gamma_u{}^2+\gamma_\beta{}^2+\gamma_\lambda^2}.$$

Here we have expressed the normal gravitational vector of $\gamma(u,\beta,\lambda)$. Here we have the magnitude of the total normal gravity vector γ_E as γ_{Normal}.

$$\gamma_E = \begin{bmatrix}\gamma_u\\ \gamma_\beta\\ 0\end{bmatrix}.$$

While this complete calculation of g above an ellipse is more accurate than the Taylor series, it is not the exact calculation of the normal component. To calculate the normal component, it is necessary to make the distinction between geodetic and geocentric coordinates. The difference in the direction of γ_{total} and γ_h is the angle ε. It is also necessary to perform several coordinate transforms.

$$R_1 = \begin{bmatrix}\frac{u}{w\cdot\sqrt{u^2+E^2}}\cdot\cos(\beta)\cdot\cos(\lambda) & \frac{-1}{w}\cdot\sin(\beta)\cdot\cos(\lambda) & -\sin(\lambda)\\ \frac{u}{w\cdot\sqrt{u^2+E^2}}\cdot\cos(\beta)\cdot\sin(\lambda) & \frac{-1}{w}\cdot\sin(\beta)\cdot\sin(\lambda) & \cos(\lambda)\\ \frac{1}{w}\cdot\sin(\beta) & \frac{u}{w\cdot\sqrt{u^2+E^2}}\cdot\cos(\beta) & 0\end{bmatrix}.$$

$$R_2 = \begin{bmatrix} \cos(\psi)\cdot\cos(\lambda) & \cos(\psi)\cdot\sin(\lambda) & \sin(\psi) \\ -\sin(\psi)\cdot\cos(\lambda) & -\sin(\psi)\cdot\sin(\lambda) & \cos(\psi) \\ -\sin(\psi) & \cos(\lambda) & 0 \end{bmatrix}.$$

The first is the coordinate transform to change the ellipsoidal system into the rectangular coordinate system. The second is the coordinate transform to change the rectangular coordinate system into spherical coordinates of which a normal can be defined.

$$\gamma_{Spherical} = R_2 \cdot \left(R_1 \cdot \gamma_{Elliptical}\right).$$

$$\gamma_{Spherical} = \begin{bmatrix} \gamma_r \\ \gamma_\psi \\ \gamma_\lambda \end{bmatrix}.$$

After the components of gravity are transformed into spherical coordinates we must project them onto the geodetic normal line through the point P(x,y,z). This is done by using the difference between geocentric (ψ) and geodetic (φ) latitudes.

$$\alpha = \phi - \psi\ .$$

The equation to calculate the exact value of the normal gravity component at point P(x,y,z) is therefore:

$$\gamma_{Normal} = -\gamma_r \cdot \cos(\alpha) - \gamma_\psi \cdot \sin(\alpha).$$

Appendix B

Temperature-Reduction Programs

```
PRO   NIGHTLY_REDUCTION
      Time          =     30.0    ;Number of two minute profiles to use
      Threshold     =     1/16.0  ;Maximum percent error allowed
      Geolat        =     41.742  ;Latitude
      Geolong       =     241.19  ;Longitude
      AvgBins       =     81      ;Number of bins for a 3 km boxcar average
      MMM           =     28.9415;Mean Molecular Mass
      RRR           =     8.31432;Ideal gas constant
      Altres        =     0.0375  ;Altitude resolution of lidar
      Hour          =     7       ;Hour in UTC to run MSIS
      Bins          =     14005   ;Number of range bins
      DateInput, Timestring ;Returns the date to be opened
      Readbinary, Timestring, Date,Data,Headers, Bkhi , Bklo
                                  ;Reads in the nightly data from hard disk
      CalculateTime, Headers,Time,TimeProfiles,RayleighTimes
                                  ;Bins the data hourly
      Altprof=      FINDGEN(BINS)*Altres+1.47+Altres/2
                                  ;calculates altitudes of lidar returns
      Dayofyear, Timestring,Doy
                                  ;returns an approximate DOY
      RUNMSISe90, Geolat,Geolong,Doy,Hour,Altres,Atmosphere
                                  ;runs MSISe90 and returns results
      RayleighError,Data,RayleighTimes,Avgbins,CntError,PctError,Signal,$
                  AvgSignal,Bklo,Bkhi       ;Calculates measurement error
      CalculateDensity,AvgSignal,Altprof,Density
                                  ;Calculates the hourly density profiles
      Gravity, Geolat,Geolong,Bins,Altres,Gnew
                                  ;Calculates the gravity profile above the lidar
      TopCalculation,CntEror,PctError,AvgSignal,Threshold,Doy,Altprof,$
                  Atmosphere,Topbin,TopTemp
                                  ;Calculates starting altitude and temperature
      TempCalculation,Altprof,Density,Gnew,MMM,RRR,Altres,Topbin,$
                  TopTemp,Temperature
                                  ;Calculates hourly and nightly temperatures
      TempError,Temperature,Altprof,PctError,Topbin,Temperr
                                  ;Propagates measurements errors into ;temperature
                                  errors
      Timestamp     =     SYSTIME()       ;reads in system time
      File          =     'c:\lidar data\'+Timestring+'.dat'
                                  ;file to store analyzed data into
      SAVE, Temperature,Density,TempErr,Altprof,Topbin,TopTemp,Headers,$
            Date,Data,Rayleightimes,Bkhi,Bklo,Timestamp,Filename=FILE
                                  ;IDL save command
END
```

```
PRO DateInput       ,Temp
        Directory   =       'c:\lidar data\'
        PRINT,      'Enter the data for temperature-reduction.'
        PRINT,      'Example: Enter 011228 for Dec 28, 2001'
        READ        ,       'TEMP
        RETURN
END

PRO ReadBinary      ,TimeString,Date,Data,Headers,Bklo,Bkhi
        Year        =       STRMID(Timestring,0,2)      ;gets year
        Month       =       STRMID(Timestring,2,2)      ;gets month
        Day         =       STRMID(Timestring,4,2)      ;gets day
        Data        =       ''                          ;defining a string
        Filedir     =       'c:\lidar data\'+Year+Month+'\Rayleigh\'
                                                        ;data directory
        Filename    =       Year+Month+Day              ;main filename
        File        =       STRUPCASE(Filedir+'*'+Filename+'*.*')
                            ;string with the correct data and wildcards
        Filenames   =       FINDFILES(File)
                            ;finding all files in subdirectory with correct date
        Length=     (SIZE(Filenames))(1) ;number of files found
        Headers     =       STRARR(Length,12) ;defining space for headers
        Header=     ''                          ;string to read in headers
        Time        =       STRARR(Length,2)            ;defining space for times
        Data        =       FLTARR(Length,14005)        ;defining space for data
        Line        =       INTARR(7)                   ;integers to read in data
        FOR i=0, Length-1 DO BEGIN
                SPAWN, 'readmcs'+Filenames(i)+' >'+'I:'+Filename+'asc'+,$
                        '.'+STRTRIM(String(i),1),/hide
                            ;call to external routing to convert binary data to text
                GET_LUN,LUN         ;defining a logical unit number to reference a file
                OPENR,LUN,'I:\'+Filename+'asc'+'.'+STRTRIM(string(i),1)
                                    ;opening text file to be read
                FOR j=0, 11 DO BEGIN
                        READF,LUN,Header            ;read in line of txt
                        Headers(i,j)    =       Header;save text in headers
                ENDFOR
                k=0
                WHILE (k lt 13990) DO BEGIN
                        READF,LUN,LINE                      ;reads in 6 range bins
                        Data(I,k:k+5)=Line(1:6)             ;stores them in data
                        K=k+6
                ENDWHILE
                CLOSE, LUN
```

```
            FREE_LUN,LUN
            FILE_DELETE,'I:\'+Filename+'asc'+'.'+STRTRIM(string(i),1)
            Plot, Data(i,*),yrange=[1.0,10000],/ylog      ;plots 2 min profile
        ENDFOR
        Temp        =       FLTARR(13990)
        FOR i=0,13990-1 DO BEGIN
            Temp(i)     =       MEAN(Data(0:length-1,i))
        ENDFOR
        PLOT, temp(*),ylog=1,yrange=[.1,10000]          ;Averages nightly data
        PRINT,'Please enter the background starting point'
        READ, BKLO                                      ;start of background region
        PRINT,'Please enter the background ending point'
        READ, BKHI                                      ;end of background region
        RETURN
END

PRO CalculateTime   ,Headers,Time,Timeprofiles,RayleighTimes
        Length =    (SIZE(Headers))(1)   number of 2 minute profiles
        TimeProfiles    =       FLTARR(Length,4)        ;defining space for times
        FOR i=0, Length-1 DO BEGIN
            Temp    =       STRMID(Headers(i,4),18,8)  ;pulling out part of string
            Timeprofiles(i,0)       =       STRMID(TEMP,0,2)
                IF (Timeprofiles(I,0) GT 20) THEN Timeprofiles(i,0) =,$
                Timeprofiles(I,0),-24
            Timeprofiles(I,1)       =       STRMID(Temp,3,2)
            Timeprofiles(I,2)       =       STRMID(TEMP,3,2)
            Timeprofiles(I,3)       =       Timeprofile(I,0)*3600+,$
                Timeprofiles(I,1)*60+Timeprofiles(I,2)      ;time in seconds
        ENDFOR
        StartTime           =       TimeProfiles(0,3)   ;Initial time
        StartHour           =       Timeprofiles(0,0)   ;Initial hour
        IntTime             =       Time*2.0*60.0       ;seconds to start integration
        IF ((StarTime) GT (StartHour*3600+1800)) THEN BEGIN
            FirstHour       =       (StartHour+1.0)*3600+1800
        ENDIF ELSE BEGIN
            FirstHour       =       StartHour*3600+1800
        ENDELSE
        RayleighTimes       =       IntArr(35,3)
        RayleighTimes(0,0)  =       0
        I=0
        WHILE (Timeprofiles(I,3) LE FirstHours) DO i=i+1
        RayleighTimes(1,0)  =i
        HourRecord          =i
        K                   =i
```

```
        FOR i=HourRecord+1,Length-1 DO BEGIN
                IF ((Timeprofiles(HourRecord,3)+IntTime*k) LE,$
                        (Timeprofile(I,3))) THEN BEGIN
                        RayleighTimes(k+1,0)        =       i
                        K                           =       k=1
                ENDIF
        ENDFOR
        RayleighTimes       =       RayleighTimes(0:k+1,*)
        K                   =       (SIZE(RayleithTimes))(1)-2
        FOR j=0, k-1 DO BEGIN
                Temp                =       RayleighTimes(j+1,0)
                RayleighTimes(j,1)  =       Temp-1
                RayleighTimes(j,2)  =       Temp-RayleighTimes(j,0)
        ENDFOR
        RayleighTimes(k,1)          =       Length-1
        RayleighTimes(k,2)          =       Length-RayleighTimes(k,0)
        RayleighTimes(k+1,0)        =       0
        RayleighTimes(k+1,1)        =       Length-1
        RayleighTimes(k+1,2)        =       Length-1
        RETURN
END

PRO DayOfYear       ,Date,Doy
        MD    =     [0,31,28,31,30,31,30,31,31,30,31,30]
                ;I have ignored the effects of leap years
        Month =     Fix(STRMID(Date,2,2))
        Year  =     Fix(STRMID(Date,0,2))
        Day   =     Fix(STRMID(Date,4,2))
        Doy   =     Total(MD(0:Month-1))+Day
        RETURN
END

PRO RUNMSISE90   ,GEOLAT,GEOLONG,DAY,HOUR,ALTRES,ATMOSPHERE
        DATA                =       FLTARR(4,1)
        ATMOSPHERE          =       FLTARR(4,15000)
        FIRSTPOINT          =       5
        DayOfYears          =       FIX(DAY)
        Flux                =       150.0
        Seconds             =       FIX(Hour*3600)
        OMEGA               =       7.292e-5
        GET_LUN             ,       LUN
        OPENW               ,       LUN,'c:\idl stuff\mcs\model\msisi.in'
        PRINTF              ,       LUN,DayOfYears
```

```
        PRINTF          ,       LUN,0,0,Seconds
        PRINTF          ,       LUN,0,0,0
        PRINTF          ,       LUN,0,0,0
        PRINTF          ,       LUN,'kman'
        PRINTF          ,       LUN,'1.46 300',AltRes
        PRINTF          ,       LUN,GeoLat,GeoLong
        PRINTF          ,       LUN,Flux,Flux
        PRINTF          ,       LUN,' 4 0 0 0 0 0 0'
        PRINTF          ,       LUN,'000 000'
        PRINTF          ,       LUN,'msisi.out'
        PRINTF          ,       LUN,'000'
        CLOSE           ,       LUN
        FREE_LUN        ,       LUN
        CD              ,       'c:\idl stuff\mcs\model\'
        SPAWN           ,       'Msisi.exe',/hide
        ON_ERROR        ,       1
        GET_LUN         ,       LUN
        OPENR           ,       LUN,'c:\idl stuff\mcs\model\msisi.out'
        POINT_LUN       ,       LUN,FirstPoint
        PRINT           ,       'Accessing the Model Information'
        j               =       0
        WHILE NOT EOF(LUN) DO BEGIN
                READF   ,       LUN,DATA
                ATMOSPHERE(*,j) =DATA
                j=j+1
        ENDWHILE
        CLOSE           ,       LUN
        FREE_LUN        ,       LUN
        Atmosphere      =       Atmosphere(*,0:j-1)
END

Pro RayleighError2      ,Data,RayleighTimes,add,AvgBins,CntError,$
                        PctError,Signal,AvgSignal,BKLO,BKHI
        Length                  =       (Size(Data))(2)
        Width                   =       (Size(Data))(1)
        Twidth                  =       (Size(RayleighTimes))(1)
        Background              =       FLTARR(Width)
        SignalError             =       FLTARR(Width,Length)
        CntError                =       FLTARR(TWidth,Length)
        Signal                  =       FLTARR(Width,Length)
        PctError                =       FLTARR(TWidth,Length)
        AvgSignal               =       FLTARR(TWidth,Length)
        AvgRayleigh             =       FLTARR(TWidth,Length)
        AvgBackground           =       FLTARR(Twidth)
```

```
        Temp                    =       FLTARR(Length)
        Temp2                   =       0.0

        FOR i=0,Width-1 DO BEGIN
                Background(i)           =       TOTAL(DATA(i,BKLO:BKHI)),$
                /(BKHI-BKLO+1.0)
                Signal(i,*)             =       Data(i,*)-Background(i)
        ENDFOR
        FOR i=0,Twidth-1 DO BEGIN
                a               =               rayleightimes(i,0)
                b               =               rayleightimes(i,1)
                c               =               rayleightimes(i,2)
                temp(*)         =       0.0
                temp2  =        0.0
                k               =       0
                FOR l=a,b do begin
                        IF ((signal(l,1100) GE 60.0) AND (background(l) LT 20)) ,$
                        THEN BEGIN
                                temp(*)         =       temp(*)+data(l,*)
                                temp2           =       temp2+background(l)
                                k               =       k+1.0
                        ENDIF
                ENDFOR
                Rayleightimes(i,2)              =       c
                AvgSignal(i,*)                  =       Temp(*)/k
                AvgBackground(i)                =       temp2/k
                IF (i EQ (twidth-1)) Then begin
                        AvgSignal(i,*)          =       AvgSignal(i,*)+add
                        AvgBackground(i)        =       AvgBackground(i)+add
                ENDIF
                AvgSignal(i,*)                  =       Smooth(AvgSignal(i,*),Avgbins)
                Cnterror(i,*)                   =       AvgSignal(i,*)/(Avgbins*k)+,$
                AvgBackground(i)/(k*(BKHI-BKLO+1.0))
                AvgSignal(i,*)                  =       AvgSignal(i,*)-AvgBackground(i)
                Pcterror(i,*)                   =       SQRT(Cnterror(i,*))/AvgSignal(i,*)
        ENDFOR
        RETURN
END

PRO Calculate Density       ,TavgRayleigh,Altres,Bins,Density
        Width           =       (Size(TavgRayleigh))(1)
        Length          =       (Size(TavgRayelgih))(2)
        Density         =       FLTARR(Width,Length)
        FitBin          =       1027
        Range           =       FINDGEN(BINS)*Altres+Altres/2
```

```
        FOR j=0,Width-1 DO BEGIN
                Density (j,*)   =       TavgRayleigh(j,*)*(Range*Range)
                Density(j,*)    =       Density(j,*)/Density(j,Fitbin)
        ENDFOR
        RETURN
END

PRO GRAVITY     ,GEOLAT,GEOLONG,LENGTH,ALTRES,GNEW
        gm              =       3986004.418e8           ;gravitational constant of Earth
        omega           =       7292115.0e-11           ;angular rotation of Earth
        a               =       6378137.0               ;semi-major axis
        b               =       6356752.3142            ;semi-minor axis
        e               =       8.1819190842622e-2      ;linear eccentricity
        gge             =       9.7803253359            ;theoretical gravity at the equator
        ggp             =       9.8321849378            ;theoretical gravity at the pole
        EE              =       SQRT(a^2.0+b^2.0)       ;
        k               =       (b*ggp)/(a*gge)-1
        m               =       (omega^2.0*a^2.0*b^2.0)/gm
        f               =       1/298.257223563         ;ellipsoidal flattening
        phi             =       GeoLat*!DTOR
        si              =       atan(((1-f)^2)*tan(phi))
        lambda          =       GeoLong*!DTOR
        alpha           =       phi-si
        ho              =       1460                    ;starting altitude in meters
        N               =       a/sqrt(1-e*e*sin(phi)*sin(phi))         ;raius of curvature
        gnew            =       fltarr(length)
        FOR i=0, length-1 DO BEGIN
                h       =       1460+altres*1000.0*i
                x       =       (N+h)*cos(phi)*cos(lambda)          ;x coordinate
                y       =       (N+h)*cos(phi)*sin(lambda)          ;y coordinate
                z       =       ((b*b)/(a*a)*N+h)*sin(phi)          ;z coordinate
                u               =       sqrt((1.0/2.0)*(x*x+y*y+z*z-EE*EE),$
                *(1.0+sqrt(1.0+4.0*EE*EE*z*z/(x*x+y*y+z*z-EE*EE)^2)))
                beta    =       atan(z*sqrt(u*u+EE*EE)/(u*sqrt(x*x+y*y)))
                w       =       sqrt((u*u+EE*EE*sin(beta)*sin(beta))/(u*u+EE*EE))
                q       =       (1.0/2.0)*((1.0+3.0*u*u/(ee*ee))*atan(EE/u)-3.0*u/EE)
                qo      =       (1.0/2.0)*((1.0+3.0*b*b/(ee*ee))*atan(EE/b)-3.0*b/EE)
                qp      =       3.0*(1.0+u*u/(ee*ee))*(1.0-u/ee*atan(ee/u))-1.0
                gu      =       (-1.0/w)*(gm/(u*u+ee*ee),$
                +(omega*omega*a*a*ee*qp)/((u*u+ee*ee)*qo)*(1.0/2.0*sin(beta),$
                *sin(beta)-1.0/6.0))+omega*omega*u*cos(beta)*cos(beta)/w
                gb      =       (1/w)*(omega*omega*a*a*q)/(sqrt(u*u+ee*ee)*qo),$
                *sin(beta)*cos(beta)-omega*omega*sqrt(u*u+ee*ee)*sin(beta),$
                *cos(beta)/w
```

```
            gae     =       [gu,gb,0]
            R2      =       [[cos(phi)*cos(lambda),cos(phi)*sin(lambda),sin(phi)],$
                             [-sin(phi)*cos(lambda),-sin(phi)*sin(lambda),cos(phi)],$
                             [-sin(lambda),cos(lambda),0]]
            R1      =       [[u*cos(beta)*cos(lambda)/(w*sqrt(u^2+EE^2)),-
                    1/w*sin(beta)*cos(lambda),-sin(lambda)],$
                             [u*cos(beta)*sin(lambda)/(w*sqrt(u^2+EE^2)),-
                    1/w*sin(beta)*sin(lambda),cos(lambda)],$
                             [sin(beta)/w,u*cos(beta)/(w*sqrt(u^2+EE^2)),0]]
            gs      =       R2#(R1#gae)   ;coordinate transforms
            gphi    =       -gs(0)*sin(alpha)+gs(1)*cos(alpha)
            gh      =       -gs(0)*cos(alpha)+gs(1)*sin(alpha)
            gnew(i)         =       sqrt(gh^2+gphi^2)      ;normal component
        ENDFOR
        RETURN
END

PRO     TopCalculation          ,TavgCntError,PCTERR,TavgRayleigh,Threshold,Doy,$
                                ,AltProf,Atmosphere,Topbin,TopTemp
        Length          =       (Size(TavgCntError))(2)
        Width           =       (Size(TavgCntError))(1)
        TopBin          =       FLTARR(Width)
        TopTemp         =       FLTARR(Width)
        Restore         ,       'c:\idl stuff\mcs\programs\lidar project\sodium.sav'
        XX              =       [-16,15,46,74,105,135,166,196,227,258,288,319,349,380]
        FOR i=0, Width-1 DO BEGIN
                FOR Start=1500,2500 DO BEGIN
                        Error           =       Total(PctErr(i,Start-5:Start+5))/11.0
                        Topbin(i)       =       Start
                        IF      (Error GE Threshold) THEN BEGIN
                                Start   =       2500
                                ;Start  =       2300
                        ENDIF
                ENDFOR
                High    =       AltProf(Topbin(i))
                IF      (High LT 83) THEN BEGIN
                        Below           =       105-FIX(High)
                        IF (Below GT 22) THEN Below=22
                        Above           =       Below-1
                        Ydown           =[SheTemp(12,Below),SheTemp(1:12,Below),$
                        ,SheTemp(1,Below)]
                        NaTemp          =       SPLINE(XX,YDOWN,DOY,0.1)
                        Temp1           =       Atmosphere(2,2175)
                        Temp2           =       Atmosphere(2,TopBin(i))
```

```
                TopTemp(i)  =   NaTemp-(Temp1-Temp2)
            ENDIF ELSE BEGIN
                Below       =   105-FIX(High)
                IF (BELOW GT 22) THEN BELOW=22
                Above       =   Below-1
                YUP         =,$
                [SheTemp(12,Above),SheTemp(1:12,Above),SheTemp(1,Above)]
                YDown       =,$
                [SheTemp(12,Below),SheTemp(1:12,Below),SheTemp(1,Below)]
                TempLow     =   SPLINE(XX,YDown,DOY,0.1)
                TempHigh    =   SPLINE(XX,YUp,DOY,0.1)
                P           =   [TempLow,TempHigh]
                LL          =   [SheTemp(0,Below),SheTemp(0,Above)]
                NaTemp      =   Interpol(P,LL,High)
                TopTemp(i)  =   NaTemp
            ENDELSE
        ENDFOR
        RETURN
END

PRO TempCalculation, Altprof,Density,Gnew,MMM,RRR,Altres,TopBin,TopTemp,$
                ,Temperature
        Length      =   (SIZE(Density))(2)
        Width       =   (SIZE(Density))(1)
        Temperature =   FLTARR(Width,Length)
        FOR i=0,Width-1 DO BEGIN
            C1      =   Density(I,Topbin(i))/Density(I,*)
            C2      =   TopTemp(i)
            C3      =   Altres/(2.0*RRR*Density(I,Topbin(i)))
            Upper   =   MMM*Gnew(Topbin(i))*Density(I,Topbin(i))*C3
            Integral=0.0
            FOR j=Topbin(i)-1,1026,-1 DO BEGIN
                Lower           =   MMM*Gnew(j)*Density(i,j)*C3
                Integral        =   Integral+Upper+Lower
                Temperature(I,j)=   C1(j)*(C2+Integral)
                Upper           =   Lower
            ENDFOR
        ENDFOR
        REUTRN
END

PRO TempErrors      ,Temperature, Altprof,TavgPctError,Topbin,TempErr
        Length      =   (Size(Temperature))(2)
        Width       =   (Size(Temperature))(1)
```

```
        TempErr         =       FLTARR(Width,Length)
        FOR i=0, Width-1 DO BEGIN
                FOR j=Topbin(i),1000,-1 DO BEGIN
                        TempErr(I,j)   =       Temperature(I,j)^2.0*TavgPctErr(I,j)^2.0,$
                        +Temperature(I,Topbin(i))^2.0*TavgPctErr(I,Topbin(i))^2.0,$
                        *EXP(-2.0*(Altprof(Topbin(i))-Altprof(j))/7.0)
                        TempErr(I,j)   =SQRT(TempErr(I,j))
                ENDFOR
        ENDFOR
        RETURN
END
```

Appendix C

Lidar Observations

The lidar has been in operation for ~ 10 years. The following tables list the nights the lidar was in operation. The green boxes denote the nights that were included in the temperature climatology and the black boxed denote nights that were left out. There are a total of 817 nights comprised of 590 good nights and 227 bad nights.

Table 1. Nights of Observations for 1993 the Green Nights are Included in Climatology

93	1	2	3	4	5	6	7	8	9	10	11	12	13	14	15	16	17	18	19	20	21	22	23	24	25	26	27	28	29	30	31
J																															
F																															
M																															
A																															
M																															
J																															
J																															
A																															
S																															
O																															
N																															
D																															

Table 2. Nights of Observations for 1994 the Green Nights are Included in Climatology

94	1	2	3	4	5	6	7	8	9	10	11	12	13	14	15	16	17	18	19	20	21	22	23	24	25	26	27	28	29	30	31
J																															
F																															
M																															
A																															
M																															
J																															
J																															
A																															
S																															
O																															
N																															
D																															

Table 3. Nights of Observations for 1995 the Green Nights are Included in Climatology

95	1	2	3	4	5	6	7	8	9	10	11	12	13	14	15	16	17	18	19	20	21	22	23	24	25	26	27	28	29	30	31
J																															
F																															
M																															
A																															
M																															
J																															
J																															
A																															
S																															
O																															
N																															
D																															

Table 4. Nights of Observations for 1996 the Green Nights are Included in Climatology

96	1	2	3	4	5	6	7	8	9	10	11	12	13	14	15	16	17	18	19	20	21	22	23	24	25	26	27	28	29	30	31
J																															
F																															
M																															
A																															
M																															
J																															
J																															
A																															
S																															
O																															
N																															
D																															

Table 5. Nights of Observations for 1997 the Green Nights are Included in Climatology

97	1	2	3	4	5	6	7	8	9	10	11	12	13	14	15	16	17	18	19	20	21	22	23	24	25	26	27	28	29	30	31
J																															
F																															
M																															
A																															
M																															
J																															
J																															
A																															
S																															
O																															
N																															
D																															

Table 6. Nights of Observations for 1998 the Green Nights are Included in Climatology

98	1	2	3	4	5	6	7	8	9	10	11	12	13	14	15	16	17	18	19	20	21	22	23	24	25	26	27	28	29	30	31
J																															
F																															
M																															
A																															
M																															
J																															
J																															
A																															
S																															
O																															
N																															
D																															

Table 7. Nights of Observations for 1999 the Green Nights are Included in Climatology

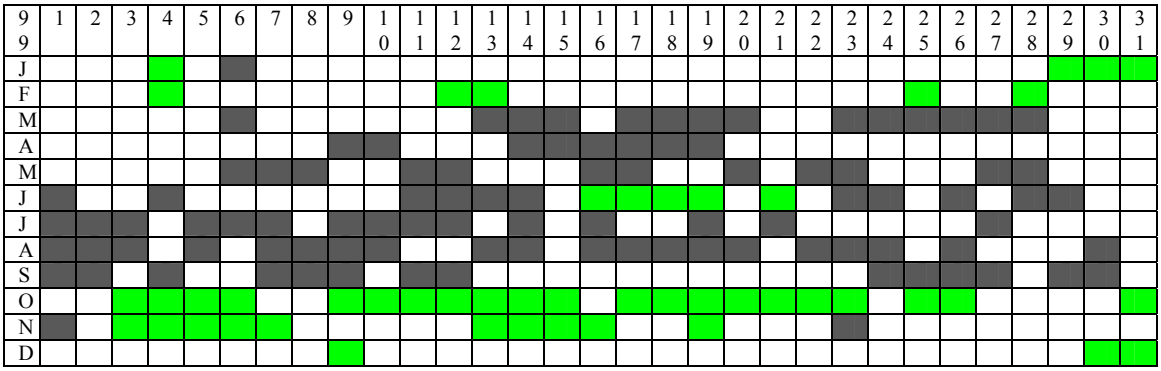

Table 8. Nights of Observations for 2000 the Green Nights are Included in Climatology

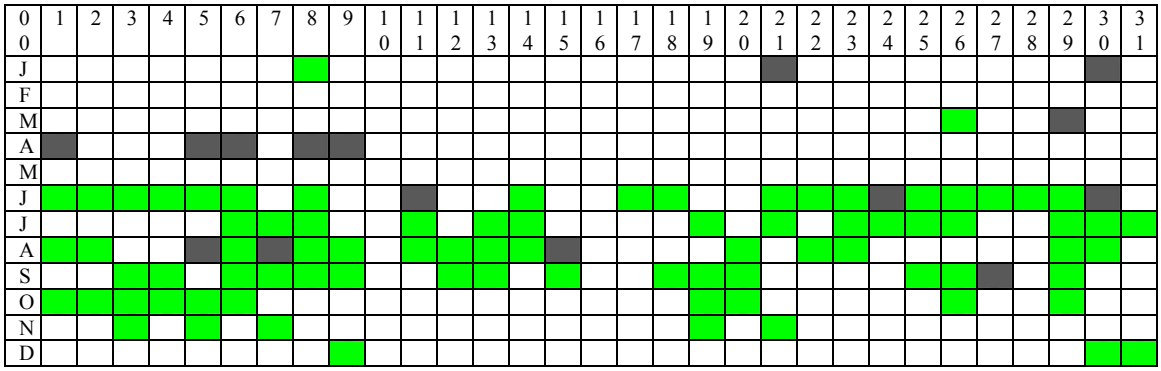

Table 9. Nights of Observations for 2001 the Green Nights are Included in Climatology

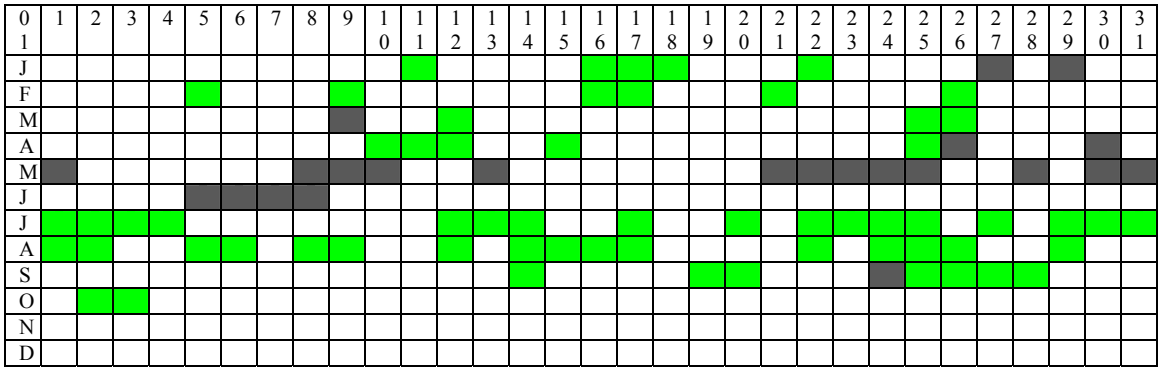

Table 10. Nights of Observations for 2002 the Green Nights are Included in Climatology

02	1	2	3	4	5	6	7	8	9	10	11	12	13	14	15	16	17	18	19	20	21	22	23	24	25	26	27	28	29	30	31
J																															
F																															
M																															
A																															
M																															
J																															
J																															
A																															
S																															
O																															
N																															
D																															

Table 11. Nights of Observations for 2003 the Green Nights are Included in Climatology

03	1	2	3	4	5	6	7	8	9	10	11	12	13	14	15	16	17	18	19	20	21	22	23	24	25	26	27	28	29	30	31
J																															
F																															
M																															
A																															
M																															
J																															
J																															
A																															
S																															
O																															
N																															
D																															